A Wearable Heart Monitor at the Ear using Ballistocardiogram (BCG) and Electrocardiogram (ECG) with a Nanowatt ECG Heartbeat Detection Circuit

by

David Da He

B.A.Sc., University of Toronto (2005)
S.M., Massachusetts Institute of Technology (2008)

Submitted to the Department of
Electrical Engineering and Computer Science
in partial fulfillment of the requirements for the degree of

Doctor of Philosophy

at the

MASSACHUSETTS INSTITUTE OF TECHNOLOGY

February 2013

Author ....
Department of
Electrical Engineering and Computer Science
January 31, 2013

Certified by ....
Charles G. Sodini
LeBel Professor of Electrical Engineering
Thesis Supervisor

Accepted by ....
Leslie A. Kolodziejski
Chair, Department Committee on Graduate Theses

A Wearable Heart Monitor at the Ear using Ballistocardiogram (BCG) and Electrocardiogram (ECG) with a Nanowatt ECG Heartbeat Detection Circuit

by

David Da He

Submitted to the Department of
Electrical Engineering and Computer Science
on January 31, 2013, in partial fulfillment of the
requirements for the degree of
Doctor of Philosophy

Abstract

This work presents a wearable heart monitor at the ear that uses the ballistocardiogram (BCG) and the electrocardiogram (ECG) to extract heart rate, stroke volume, and pre-ejection period (PEP) for the application of continuous heart monitoring.

Being a natural anchoring point, the ear is demonstrated as a viable location for the integrated sensing of physiological signals. The source of periodic head movements is identified as a type of BCG, which is measured using an accelerometer. The head BCG's principal peaks (J-waves) are synchronized to heartbeats. Ensemble averaging is used to obtain consistent J-wave amplitudes, which are related to stroke volume. The ECG is sensed locally near the ear using a single-lead configuration. When the BCG and the ECG are used together, an electromechanical duration called the RJ interval can be obtained. Because both head BCG and ECG have low signal-to-noise ratios, cross-correlation is used to statistically extract the RJ interval.

The ear-worn device is wirelessly connected to a computer for real time data recording. A clinical test involving hemodynamic maneuvers is performed on 13 subjects. The results demonstrate a linear relationship between the J-wave amplitude and stroke volume, and a linear relationship between the RJ interval and PEP.

While the clinical device uses commercial components, a custom integrated circuit for ECG heartbeat detection is designed with the goal of reducing power consumption and device size. With $58nW$ of power consumption, the ECG circuit replaces the traditional instrumentation amplifier, analog-to-digital converter, and signal processor with a single chip solution. The circuit demonstrates a topology that takes advantage of the ECG's characteristics to extract R-wave timings at the chest and the ear in the presence of baseline drift, muscle artifact, and signal clipping.

Thesis Supervisor: Charles G. Sodini
Title: LeBel Professor of Electrical Engineering

To my parents and Amanda.

Acknowledgments

Finishing Ph.D. is sometimes compared to reaching the light at the end of the tunnel, but for me there has been plenty of enlightenment but no tunnel in sight. For this, I have the following people to thank.

First, I would like to express my gratitude to the other name on the thesis cover: Professor Charlie Sodini. His rigor has made me a more disciplined engineer and his sharp insight has taught me how to think critically. But beyond that, Charlie sincerely cares for the well-being of his students. This comes through in many ways, one of which is how Charlie makes sure that we live beyond the confines of the lab. From dining in Sai Kung, to fending off feral monkey attacks, to learning to body surf, to going to Sox games, Charlie has made my Ph.D. experience unforgettably more than just academic.

I would like to thank Amanda Balderrama. I am the luckiest person to be blessed with her companionship and friendship on my journey. Through thick and thin, I can always count on her to brighten my day. Sharing my successes with her gives meaning to my work.

I would like to thank everyone in the Sodini/Lee lab for making it such a fun place to work and to collaborate. Specifically, I would like to thank Eric Winokur for working with me on this project. Also, I would like to thank Kailiang Chen, SungWon Chung, and Marcus Yip for helping me tremendously with my tape out. I would like to thank all my friends for making my experience at MIT so fulfilling, whether it is jamming on Friday nights at Edgerton, playing tennis in the bubble, or petting stingrays in Grand Cayman. These friendships last a lifetime and I hope our paths will cross many times in the future.

I would like to thank Dr. Thomas Heldt for answering my physiology questions since the very beginning of the project and for helping me setup the clinical test protocol and equipment. Tom O'Dwyer and Dr. Michael Coln offered generous help from Analog Devices with chip packaging and technical advice. Their assistance is much appreciated.

The clinical test would not have been possible without the help of Catherine Ricciardi of MIT's Clinical Research Center, who helped us from abrading skin to zeroing timers. Although no humans were harmed in the production of this thesis, many hairs were lost and many skin cells were irritated. For that, my gratitude goes out to the clinical test subjects, who generously volunteered their time and cardiovascular responses to produce the data that you see in this thesis.

I would like to thank Guha Balakrishnan for helping me with the video analysis experiment with his algorithms and enthusiasm. I would also like to thank Professor Harry Lee and Professor Roger Mark for serving on my thesis committee. Their guidance and assistance have been crucial to the project's direction.

Finally and most importantly, I would like to thank my parents Yingmei Du and Ming He. I would not be where I am today without their support, sacrifice, and unconditional love. I cannot overstate my gratitude to them.

This project's funding is made possible by the MIT Medical Electronic Device Realization Center (MEDRC), the MIT Center for Integrated Circuits and Systems (CICS), and the Canadian NSERC Postgraduate Fellowship.

List of Abbreviations

ADC	Analog-to-digital converter
ASIC	Application-specific integrated circuit
BCG	Ballistocardiogram
BMI	Body Mass Index
CMFB	Common-mode feedback
CMRR	Common-mode rejection ratio
CVD	Cardiovascular disease
DBP	Diastolic blood pressure
DRL	Driven-right-leg
DSP	Digital signal processor
ECG	Electrocardiogram
EMD	Electromechanical delay
EOV	Electrode offset voltage
HR	Heart rate
HRV	Heart rate variability
IA	Instrumentation amplifier
IC	Integrated circuit
ICG	Impedance cardiogram
ICT	Isovolumic contraction time
LED	Light-emitting diode
LVET	Left ventricular ejection time
MAP	Mean arterial pressure
NEF	Noise efficiency factor

NSDE	Normalized standard deviation from the ensemble
PAT	Pulse arrival time
PEP	Pre-ejection period
PGA	Programmable gain amplifier
PPG	Photoplethysmogram
PSRR	Power supply rejection ratio
PTT	Pulse transit time
PWV	Pulse wave velocity
QRS	ECG's Q-wave to S-wave interval
RJI	RJ interval
SAR	Successive approximation register
SBP	Systolic blood pressure
SNR	Signal-to-noise ratio
SPI	Serial Peripheral Interface
SpO_2	Saturation of peripheral oxygen (%)
SV	Stroke volume
UART	Universal Asynchronous Receiver/Transmitter
USB	Universal Serial Bus

Contents

List of Figures

List of Tables

Chapter 1

Introduction

1.1 Cardiovascular Disease Monitoring

Cardiovascular disease (CVD) affects 37% of the United States population and is the leading cause of death in the U.S. [1]. This work focuses on the continuous and wearable measurements of key cardiovascular parameters including heart rate, stroke volume (SV), and pre-ejection period (PEP). Each parameter has specific applications in the field of cardiovascular disease monitoring.

Heart rate is obtained by measuring R-wave (the principal peak of the ECG) timings, which can be used to monitor arrhythmias that contain irregular beat intervals. An example is atrial fibrillation (AF), which is the most common form of cardiac arrhythmia [2]. AF is often undiagnosed, but increases the risk of stroke and heart failure [2]. One of the markers of AF is irregular RR intervals (the time period between adjacent R-waves), which can be identified with continuous R-wave monitoring. Another example is premature ventricular contraction (PVC). A PVC occurs when a premature ventricular beat occurs before a regular beat, resulting in a large and wide R-wave and a short RR interval. PVC's can occur in a healthy person, but they can also be the symptom of an underlying CVD such as cardiomyopathy. PVC's irregular RR intervals can be identified with continuous R-wave monitoring.

SV and PEP are important parameters for congestive heart failure (CHF) patients. In CHF, the heart is unable to pump sufficient blood to meet the body's metabolic demands. CHF accounted for 35% of all U.S. CVD deaths and was mentioned in one in nine death certificates in 2008 [3]. SV is the volume of blood pumped per heartbeat and is a measure of the heart's pumping ability. When SV is multiplied with heart rate, cardiac output (CO) can be obtained, which is defined as the total volume of blood pumped per minute. Because of the heart's reduced pumping ability, CHF patients exhibit decreased CO [4]. PEP can also be used to evaluate ventricular performance in CHF patients [5] [6]. PEP is the delay between the ventricular depolarization and the ejection of blood into the aorta. CHF patients have been found to have the inability to decrease PEP upon cardiovascular demand, and are characterized with prolonged PEP [4]. A continuous monitoring device for SV, CO, and PEP can assist closed-loop managements of CHF in an outpatient setting, where the device can detect trends and alarm caregivers or physicians to intervene before the condition deteriorates to require hospitalization [7].

With the additional measurement of the photoplethysmogram (PPG), this work also enables the continuous measurement of pulse transit time (PTT). PTT can be used to cufflessly measure blood pressure. Hypertension is a chronic condition where blood pressure is consistently above $140mmHg/90mmHg$ [8]. Hypertension increases the risk for stroke, coronary heart disease, CHF, and renal disease [9]. Hypertension affects one in three U.S. adults and the lifetime risk above the age of 40 is 90% [8]. Blood pressure can vary up to 20% in 24 hours due to circadian rhythms [10]. This variation introduces fluctuations into spot measurements provided by traditional at-home cuffed oscillometric monitors. In the clinic, "white-coat" and "masked" hypertension can lead to misdiagnosis of hypertension [11]. A continuous and wearable blood pressure monitor can detect changes in blood pressure throughout the day and provide long term trends for lifestyle or medication adjustments.

1.2 The Ear as a Location of Heart Monitoring

While most wearable heart monitors are located on the chest, this work proposes the site behind the ear as a measurement location (Figure 1-1). Inspired by hearing aids and headsets, the ear location is advantageous for both physiological and mechanical reasons.

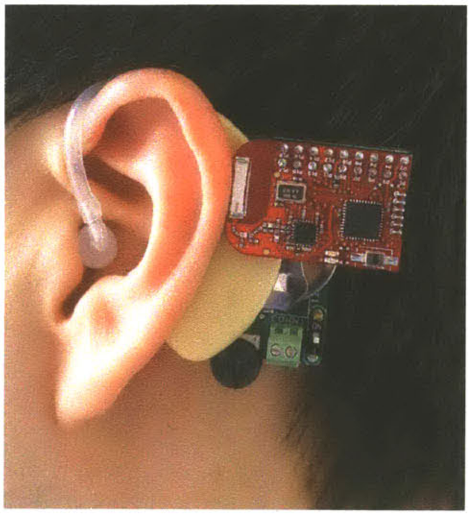

Figure 1-1: The site behind the ear is proposed as a location for the wearable heart monitor.

Physiologically, several signals can be measured at the ear location. These signals include a mechanical signal (the ballistocardiogram, BCG), an electrical signal (the electrocardiogram, ECG), and an optical signal (the photoplethysmogram, PPG). These signals allow the measurements of heart rate, stroke volume, PEP, and PTT.

Mechanically, the mastoid area behind the ear is rigid, which reduces motion artifacts compared to peripheral locations such as the earlobe, finger, and wrist. The ear location is discreet because a small device can be concealed by the ear or hair. Furthermore, as shown by hearing aids and Bluetooth headsets, the ear acts as a natural anchor. This allows device attachment using an earbud instead of adhesives, which cause skin irritation and require re-applications. For cuffless blood pressure calculations, the ear remains in the same vertical orientation relative to the heart when upright or sitting. This reduces the need for continuous hydrostatic pressure calibrations [12].

1.3 Aims of Thesis Work

The research presented in this thesis has the following seven aims:

- To achieve BCG measurements at the head with an ear-worn device in a clinical setting.
- To characterize the head BCG across different subjects to compare its morphological similarities to the traditional BCG.
- To measure heart rate and respiratory rate from the head BCG and to compare them with reference measurements.
- To investigate the relationship between the head BCG amplitudes and stroke volume across different subjects.
- To achieve ECG measurements at the head with an ear-worn device in a clinical setting.
- To use the head BCG and the head ECG to extract the RJ interval and to investigate its correlation with pre-ejection period (PEP) across different subjects.
- To create an ECG application-specific integrated circuit (ASIC) that can extract R-wave timings from both chest and head ECG while being tolerant of signal interferers, with the goal of minimizing power consumption to reduce battery size and hence device size.

1.4 Thesis Organization

This thesis is organized into the following chapters:

- Chapter 2 introduces the physiological origins of the BCG. Measurement modalities ranging from historical apparatus to modern methods are examined. Periodic head motions are identified as a type of BCG. Two methods are presented for sensing the BCG at the head using capacitive electrodes and an accelerometer. Each of the two methods has different hardware designs and challenges. The head BCG's morphology and frequency content are examined along with BCG measurements in different axes and postures. Methods to extract stroke volume and respiratory rate are proposed.

- Chapter 3 begins with a background on traditional and modern chest ECG measurements. Then, this chapter demonstrates that the ECG can be measured at the head near the ear. The head ECG's morphology and frequency content are compared with the chest ECG. The importance of the head ECG lies in the R-wave timing, which is used in Chapter 4 to obtain heart intervals.
- Chapter 4 defines several important heart intervals, the first being PEP. After discussing current PEP measurement methods, it is proposed that the RJ interval can be used to estimate PEP. The RJ interval is a timing interval between the ECG's R-wave and the BCG's J-wave and can be extracted statistically in the presence of noise. Then, the PPG is introduced to define another heart interval called pulse arrival time (PAT). The timing difference between PAT and PEP defines a third time interval, PTT. PTT's importance lies in its relationship with blood pressure. This relationship is derived using fluid dynamics.
- Chapter 5 describes the clinical prototype of the wearable heart monitor that measures the BCG and the ECG. The device's hardware, firmware, and software are discussed. A clinical test is conducted at MIT using the wearable heart monitor and reference measurement equipment. The data allows the characterization of the head BCG morphology across different subjects. Using the data, the device's measurements of heart rate, stroke volume, and PEP are evaluated.
- Chapter 6 presents a nanowatt ECG ASIC that extracts heartbeats and R-wave timings. The goal of the ECG ASIC is to directly replace the discrete ECG circuit components in the wearable heart monitor while consuming significantly less power and area. This goal is realized with a new circuit topology that re-

moves the need for an analog-to-digital converter and a signal processor while being tolerant to signal interferers. The low power circuit design of each circuit block, the electrical characterization, and ECG measurements results are discussed.

- Finally, Chapter 7 concludes the work with a summary of contributions and items for future work.

Chapter 2

The Ballistocardiogram (BCG)

This chapter introduces the physiological origins of the ballistocardiogram (BCG) and provides a background on the traditional and modern BCG measurement methods. A new BCG measurement method is proposed that senses the BCG signal at the head. The head BCG is measured using two methods, one of which uses accelerometry and is chosen as the method to study. Using acceleration measurements, the head BCG is characterized in terms of morphology, frequency content, and physical orientation. Then, methods to extract respiratory rate and stroke volume are proposed.

2.1 The Traditional and Modern BCG

The BCG is a non-invasive measurement of the body's mechanical reaction to the blood ejected by the heart during the cardiac cycle. Signals representing the BCG were first published by Gordon in 1877, when he found that for a person "maintaining, as far as possible, perfect stillness, ...a rhythmic movement ...synchronous with the pulse" can be detected [13]. The first practical measurement method was invented by Starr in 1939, who also coined the name "ballistocardiogram" [14]. Starr's setup has the subject fixed to a mechanical table (Figure 2-3(a)) that is laterally spring loaded. The force exerted by the body is recorded as the BCG.

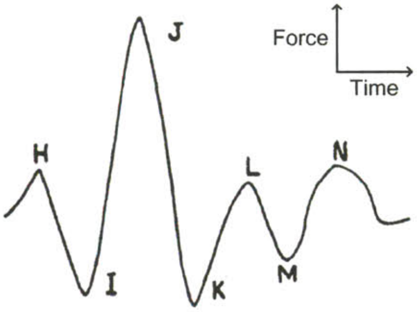

Figure 2-1: A standard BCG with its waves labeled (figure from [14]).

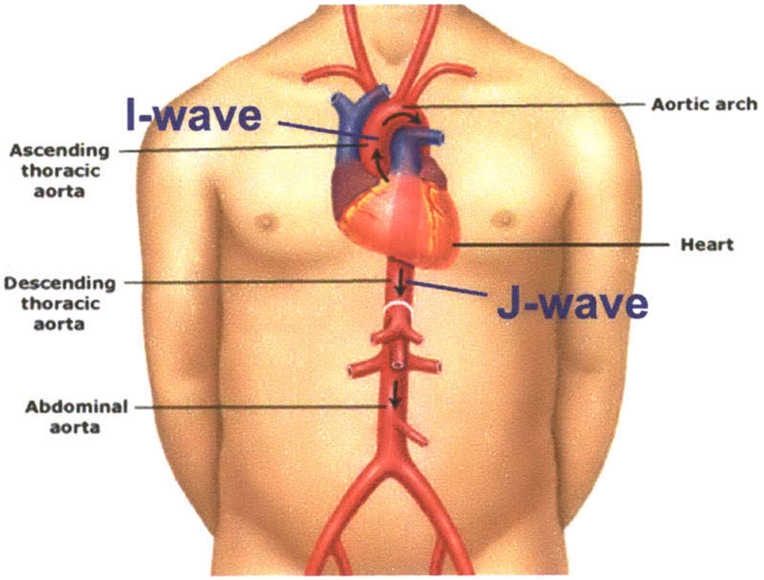

Figure 2-2: Blood flow through the aorta with I-wave and J-wave occurrences labeled (figure adapted from [15]).

A healthy subject's BCG is shown in Figure 2-1. A corresponding blood flow diagram of the aorta is shown in Figure 2-2. I-wave and J-wave are of primary interest. Wave I is due to the "headward" ejection of blood from the left ventricle into the aorta. Due to Newton's Third Law of Motion, this causes the body to recoil "footward" [16]. Wave J is due to the movement of blood from the aorta towards the abdomen through the descending aorta. This causes the body to recoil "headward" [16]. The residual oscillations after the J-wave are due to damped mechanical vibrations in the body resulting from the IJ interval [14].

The early work demonstrates that the BCG morphology can offer insights into stroke volume, the risk of heart attack, heart recovery after myocardial infarction, and mortality [14] [17] [18]. However, due to the lack of standardization and the advent of the echocardiogram, the BCG did not gain traction in the medical community [19].

Recently, there is a renewal of interest in the BCG in the scientific community [20]. This is mostly driven by modern technologies that have made the detection of the BCG signal more accessible. Figure 2-3 shows the traditional method and the modern methods. One method uses a strain-sensing foot scale to measure the BCG in an upright posture (Figure 2-3(b)) [21] [22]. A second method uses chairs (Figure 2-3(c)) that sense the BCG from electromechanical film sensors or pressure sensors for non-ambulatory situations [23] [24] [25]. Beds (Figure 2-3(d)) with load cells, strain gauges, and air mattress pressure sensors are also used to sense the BCG for bedridden patients or subjects during sleep [26] [27].

All of the above methods involve a stationary measurement device that does not allow continuous and portable measurements. The use of 3D accelerometry to measure the BCG in microgravity and dry immersion is explored by Migeotte et al. using a chest strap equipped with accelerometers (Figure 2-3(e)) [28]. However, accelerometers have yet to be studied for sensing the BCG in a normal gravity environment. It should be noted that the traditional BCG records the force exerted by the body instead of body acceleration. Therefore, accelerometer BCG readings can be converted to traditional BCG readings by multiplying the acceleration by body mass ($F_{body} = m_{body}a_{body}$).

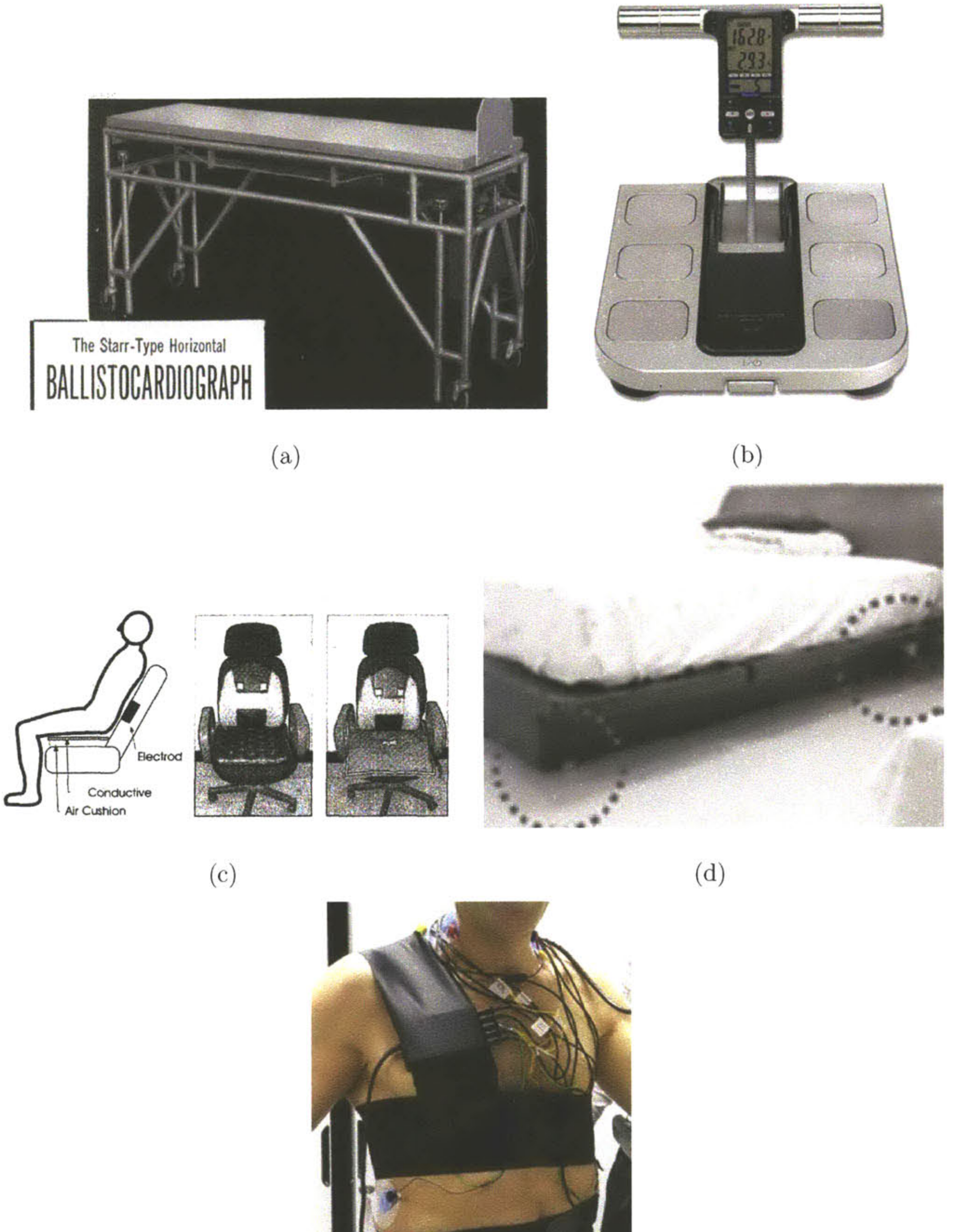

(a) (b)

(c) (d)

(e)

Figure 2-3: Traditional and modern BCG measurement methods: a) the traditional Starr BCG table [14], b) the BCG foot scale [29], c) the BCG chair [23], d) the BCG bed [26], and e) the 3D BCG chest strap [28].

2.2 The Head BCG

The MRI society has been documenting ballistocardiographic head movements as a source of movement artifacts in EEG measured during MRI [30] [31] [32]. Therefore, a proxy measurement of the BCG at the head is a possibility. Because of fundamentally different measurement techniques, the flexibility of the neck, and the lack of a low friction movement axis, the morphology of the head BCG is expected to differ from that of the traditional BCG.

It should be reinforced that the head BCG is due to the overall head acceleration instead of the local skin pulsations near the ear. To verify this, an accelerometer is mounted outside a rigid helmet that is worn on the head, where skin pulsations cannot be detected. Figure 2-4 shows that the head BCG accelerations remain detectable external to the helmet.

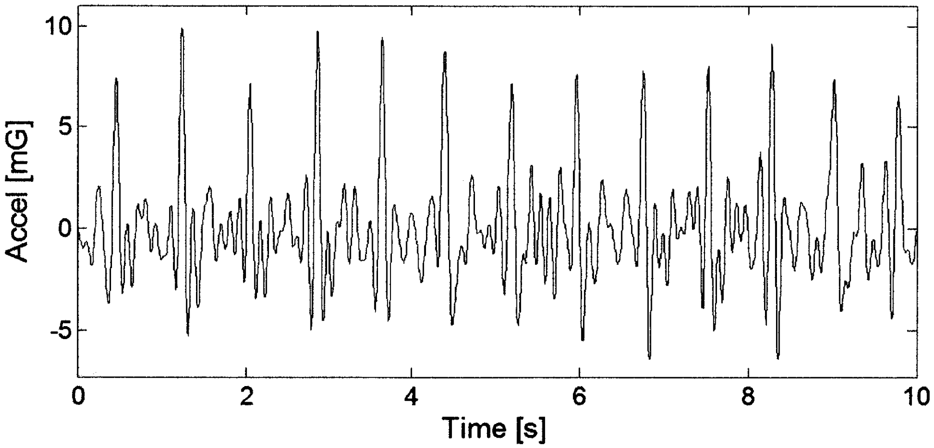

Figure 2-4: Measured head BCG signals (headward-footward direction) from an accelerometer mounted outside a rigid helmet worn on the head.

To further investigate the nature of the head BCG movement, a whole-body video motion analysis is done in collaboration with Guha Balakrishnan (MIT). The videos are recorded with 1920 × 1080 resolution at 29.97 frames per second and a bitrate of $91mbps$. The motions of the head and the chest are tracked by an algorithm, bandpass filtered from $1Hz$ to $5Hz$, and then plotted versus time. The subject is standing upright with the coordinate system labeled in Figure 2-5. Both frontal and sideways views are recorded.

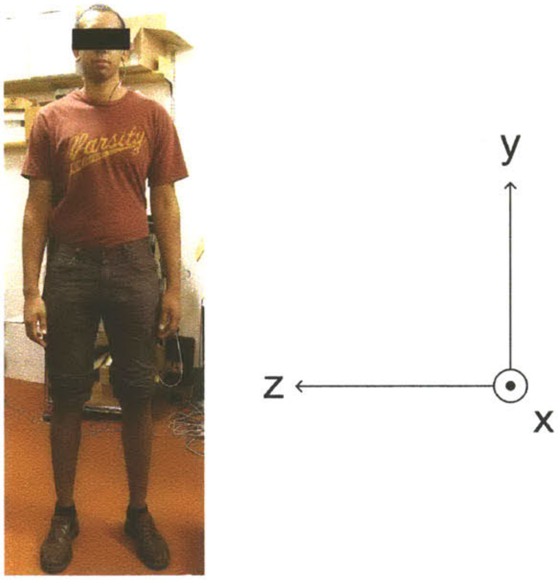
[redacted]

Figure 2-5: The subject as seen by the video camera. The coordinate system is labeled.

Figure 2-6 shows the y-axis motion versus time. It can be seen that both the chest and the head contain pulsatile BCG motions. Furthermore, as shown by the dotted lines aligned to the head motion's peaks, the head motion is synchronized to the chest motion. This suggests that the head is moving coherently with the chest in the y-axis.

Figure 2-7 shows the x-axis motion versus time, and Figure 2-8 shows the z-axis motion versus time. The existence of the BCG signal in these two axes suggests that the BCG motion is three dimensional even though the principal blood flow is vertical. However, the misalignment of the chest motion's peaks to the head motion's peaks in the x-axis suggests that the forward-backward motions are not as coherent as the other two axes.

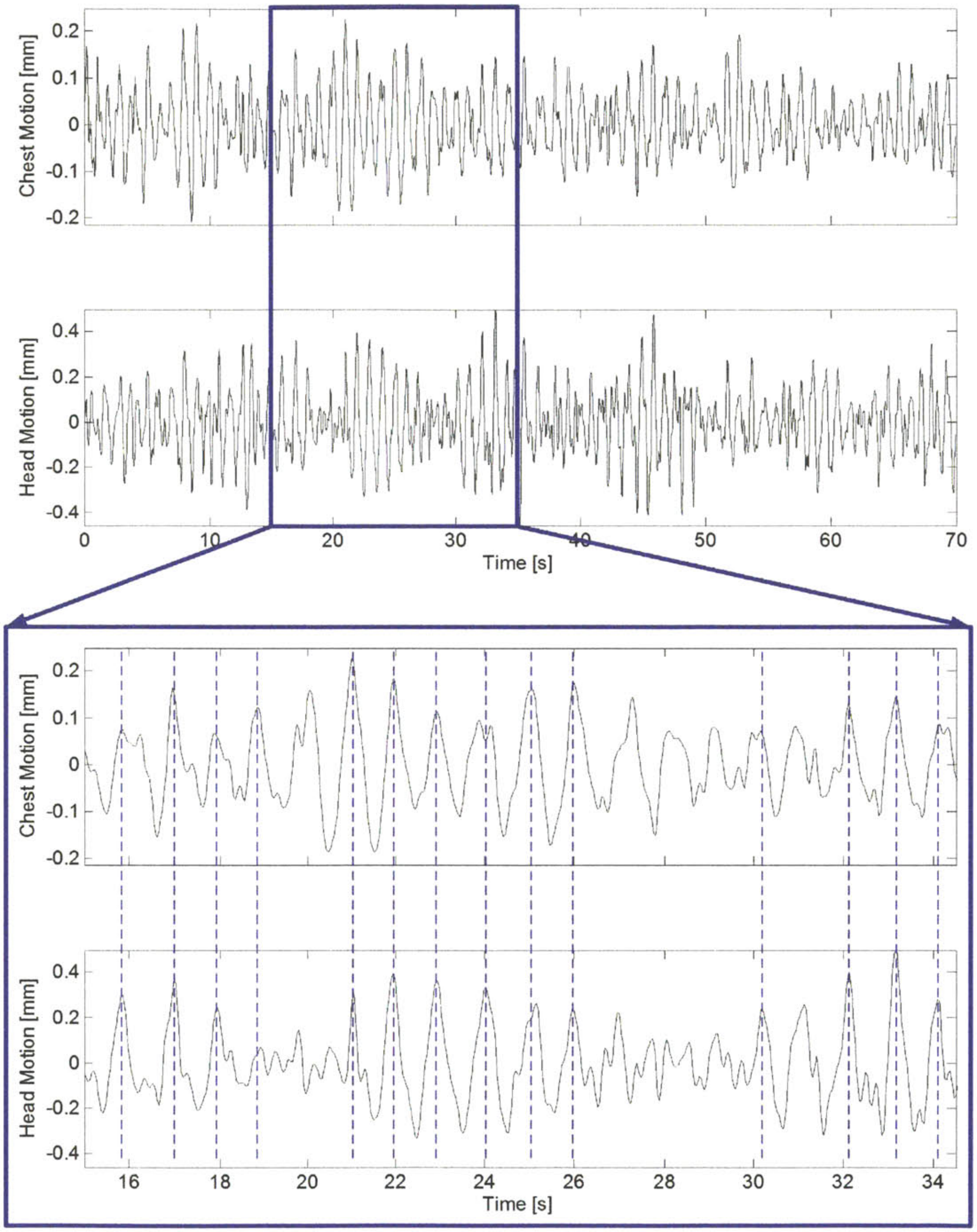

Figure 2-6: The y-axis chest and head motion extracted from video. The head motion's peaks (dotted lines) coincide with the chest motion's peaks.

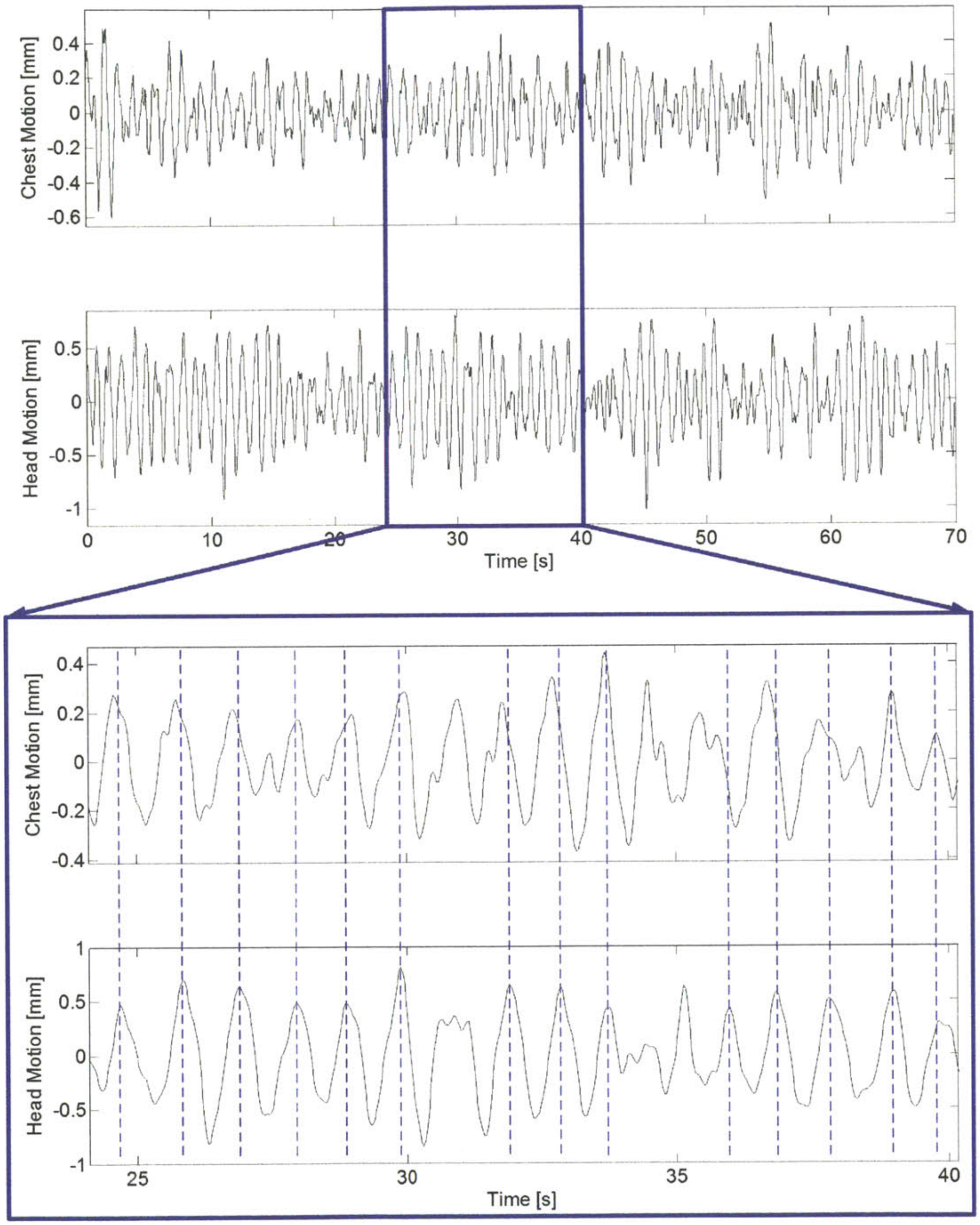

Figure 2-7: The x-axis chest and head motion extracted from video. The head motion's peaks (dotted lines) are misaligned with the chest motion's peaks.

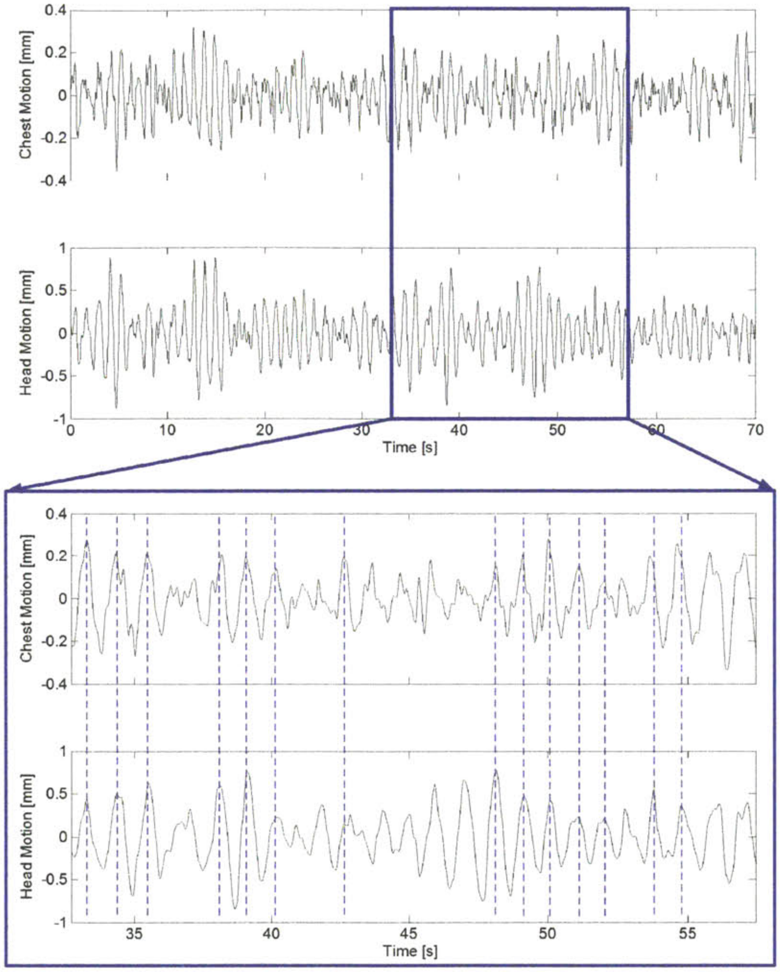

Figure 2-8: The z-axis chest and head motion extracted from video. The head motion's peaks (dotted lines) coincide with the chest motion's peaks.

The above analysis suggests that the head BCG motion is potentially contributed by the upper body's BCG movement. However, a component of the head BCG motion can also be due to the carotid blood flow into the head, which causes the head to bob vertically while pivoted at the neck. Both explanations are based on the same fundamental BCG theory of mechanical recoil caused by the internal movement of blood, whether it is in the aorta or in the carotid artery.

Two wearable head BCG measurement methods employing capacitive transduction and accelerometry are presented in the following sections.

2.3 Head BCG Measurements using Hybrid Electrodes

The first method for sensing the head BCG involves a hybrid electrode setup. This setup consists of two capacitive electrodes for differential sensing, and one dry electrode for common-mode feedback (CMFB). Because the capacitive electrodes' contact to the skin is sensitive to motion, their capacitances change with the mechanical movements associated with the head BCG, thus converting the mechanical activity into electrical signals. To reduce electrical interference, the capacitive electrodes are actively shielded. A dry electrode is used for CMFB to reduce powerline interference. The dry electrode avoids skin irritation caused by gel electrodes and still maintains a low resistance feedback path to the body.

The electrodes are constructed using nylon fabric as the insulator and conductive nickel fabric as the conductor. Both fabric materials are suitable for comfortable long term wear. Photos of the electrodes and their construction materials are shown in Figure 2-9.

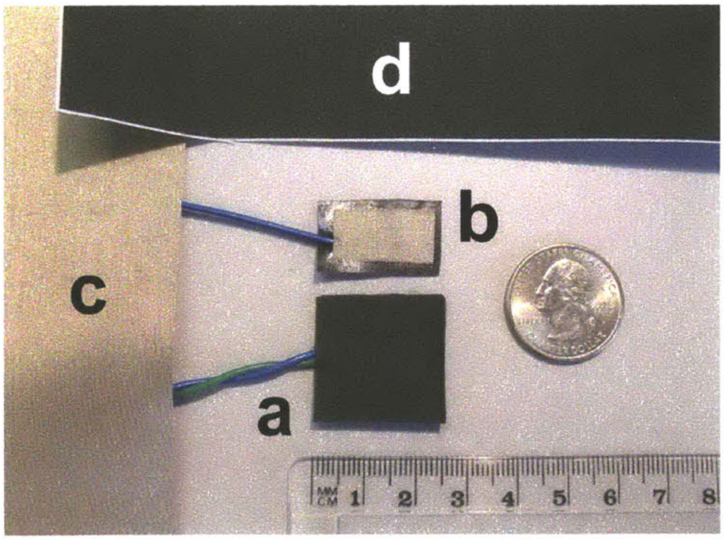

Figure 2-9: A photo of a) the capacitive sensing electrode, b) the dry CMFB electrode, c) the conductive fabric, and d) the nylon fabric.

Figure 2-10 shows the cross-section of the electrodes placed on skin. The capacitive sensing electrodes 1 and 2 have five layers consisting of a sensing layer, an active shield layer, and three insulating layers. The dry CMFB electrode is located between electrodes 1 and 2 and contains one layer driving the CMFB signal into the body and one insulating layer.

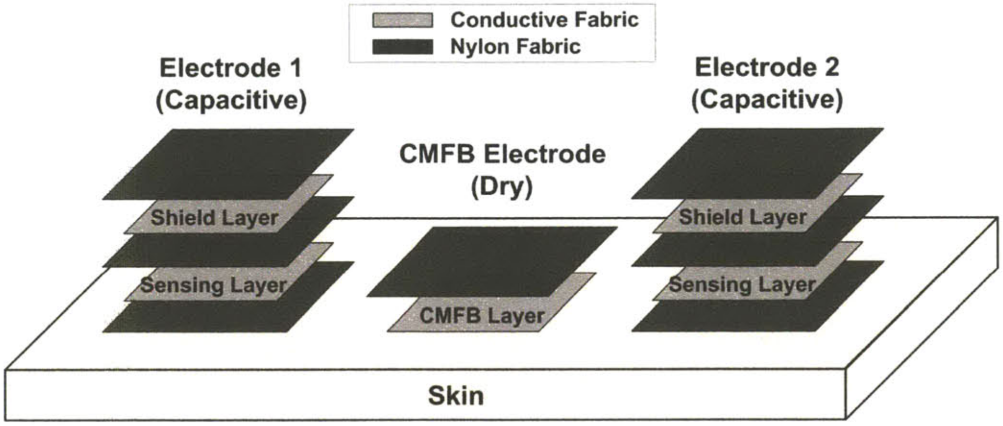

Figure 2-10: A 3D cross-section of the hybrid electrode setup placed on skin, with conductive and insulating layers shown.

The diagram of the discrete head BCG front-end circuit is shown in Figure 2-11. The capacitive electrodes have a capacitance to skin of approximately 4pF, or 4GΩ of impedance at 10Hz. Therefore, to minimize signal loss due to voltage division, the capacitive electrodes are connected to high impedance buffers with $I_{BIAS} = 10fA$ and with $5G\Omega$ bias resistors. The buffers provide active shields for the electrodes, which prevent capacitive coupling away from the skin. The differential signal goes through two twin-T $60Hz$ notch filters and into an instrumentation amplifier with a gain of $40dB$. The common-mode signal is negatively amplified by $46dB$ and then fed back into the body to reduce powerline interference. After the output, the signal is converted into the digital domain and then low pass filtered with a cutoff frequency of $40Hz$.

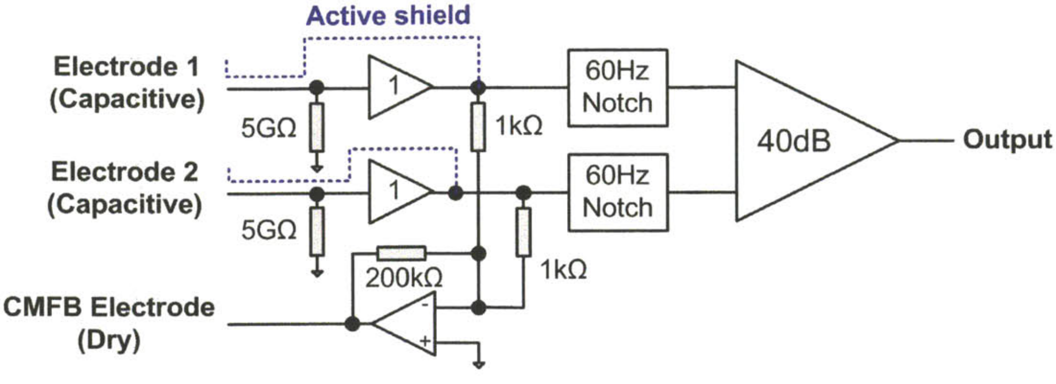

Figure 2-11: The head BCG front-end circuit.

Using the hybrid electrodes and the front-end circuit, the head BCG is measured behind the right ear and is plotted in Figure 2-12.

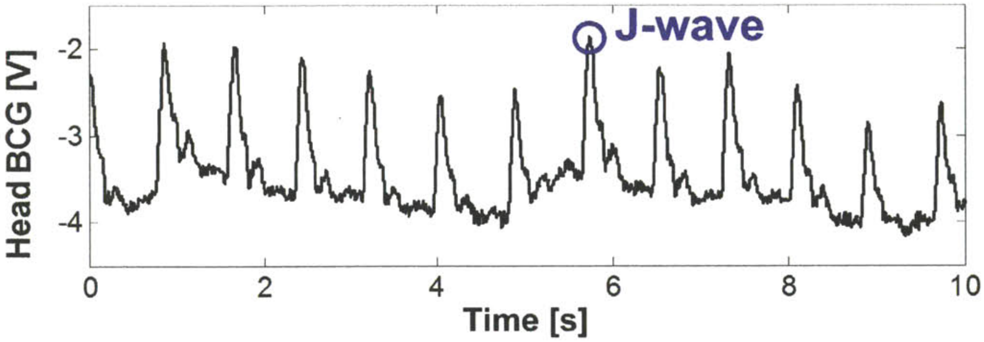

Figure 2-12: The head BCG measured using hybrid electrodes.

The head BCG in Figure 2-12 has a different morphology compared to the traditional BCG (Figure 2-1). Unlike the low friction axis offered by a BCG table, the headward-footward motion is now constrained by the ground. Also, the method of measurement is capacitive instead of directly mechanical. However, the primary wave, or J-wave, remains present.

2.4 Head BCG Measurements using an Accelerometer

Although the hybrid electrode setup can transduce the head BCG into electrical signals, it has the inherent disadvantage of requiring three electrodes. This becomes impractical when considering that the electrocardiogram (ECG) requires two additional electrodes (Chapter 3) and the skin area near the ear is limited. The electrode setup is also susceptible to powerline interference. Furthermore, the electrodes need to maintain planar adhesion to the skin, leading to mechanical design issues and possible skin irritation.

As an alternative, MEMS accelerometers are explored for sensing the head BCG. The accelerometer's advantage is that it does not need electrodes, wires, or skin contact, thus resulting in a more robust mechanical design. Also, the accelerometer is immune to electrical interference. Additionally, the accelerometer provides wearer orientation and activity information for contextual data analysis.

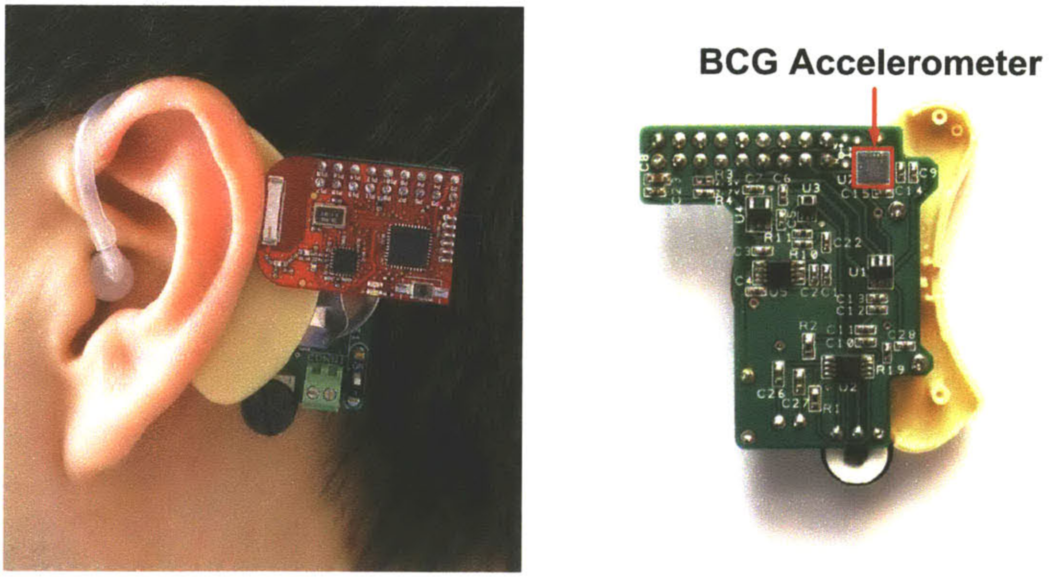

(a) (b)

Figure 2-13: a) The accelerometer-based BCG device worn at the ear, and b) the device backside exposed to show the accelerometer.

For testing, we use a 14-bit low noise ($0.69mG_{rms}$ at $\pm 2G$ range) MEMS tri-axial accelerometer (Bosch BMA180) that is mounted at the ear as shown in Figure 2-13. The accelerometer is enclosed in the housing and occupies $3mm \times 3mm \times 1mm$ of space. The acceleration data is wirelessly transmitted to a computer using a $2.4GHz$ radio (Texas Instruments CC2500).

2.4.1 The Head BCG Morphology

The measured y-axis (headward-footward) head BCG in the upright standing posture is shown in Figure 2-14.

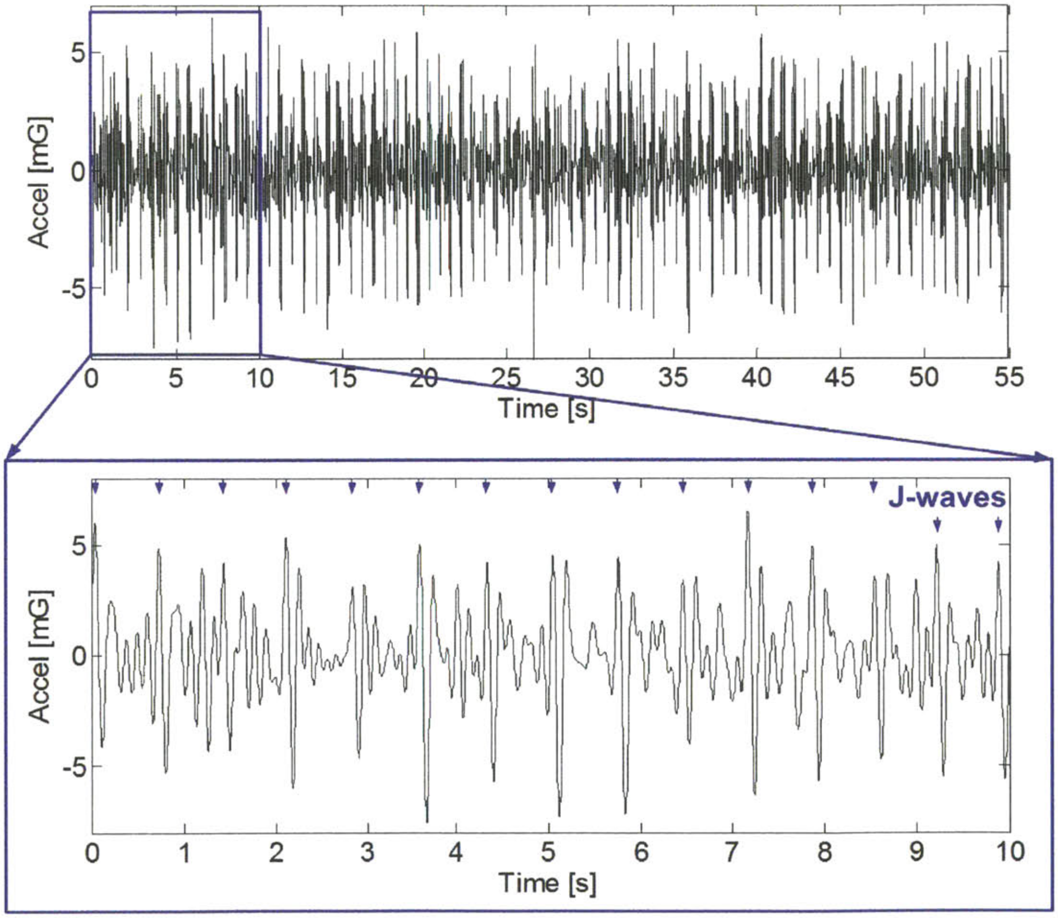

Figure 2-14: The head BCG measured by a y-axis (headward-footward) accelerometer in the standing posture. The J-waves are annotated.

The J-waves in the head BCG are immediately visible as the principal peaks. To examine the secondary BCG waves, the ensemble averages of the head BCG are created by aligning each beat's J-wave and then averaging the beats. As shown in Figure 2-15, with an increasing number of ensemble averages, H, I, K, and L-waves from the traditional BCG become visible. The fact that the majority of the traditional BCG waves exist in the head BCG suggests that the underlying accelerations are preserved. The wave amplitudes are expected to differ between subjects and this variation is characterized through the clinical test in Chapter 5.

The signal quality of the head BCG can be evaluated by its beat-to-beat morphology's repeatability. A clean BCG with no artifacts typically has highly consistent beat morphology, whereas motion artifacts will have uncorrelated beat-to-beat morphology. To quantify the repeatability of the BCG signal, we introduce a metric that is based on the standard deviation between individual beats to the ensemble average. This standard deviation is normalized to the ensemble's J-wave amplitude to produce a metric called Normalized Standard Deviation from the Ensemble (NSDE). NSDE is defined in Equation (2.2), where M is the number of samples per beat, N is the number of beats, *Ensemble* is the ensemble average of N beats, and J is the ensemble average's J-wave amplitude. For the measurement in Figure 2-14, NSDE is 21% for $N = 20$. While a greater N reduces fluctuations in the ensemble waveform, it also masks any short term changes due to averaging. $N = 20$ is chosen for the ensemble averages in this work as it produces sufficiently stable ensemble waveforms with an averaging window of approximately 20 seconds.

$$\begin{aligned} NSDE &\overset{\text{def}}{=} \frac{1}{J}\left(\frac{1}{N}\sum_{i=1}^{N}\left(Stdev\left(Beat_i - Ensemble\right)\right)\right) && (2.1)\\ &= \frac{1}{J}\left(\frac{1}{N}\sum_{i=1}^{N}\left(\sqrt{\frac{1}{M}\sum_{j=1}^{M}(Beat_i[j] - Ensemble[j])^2}\right)\right) && (2.2)\end{aligned}$$

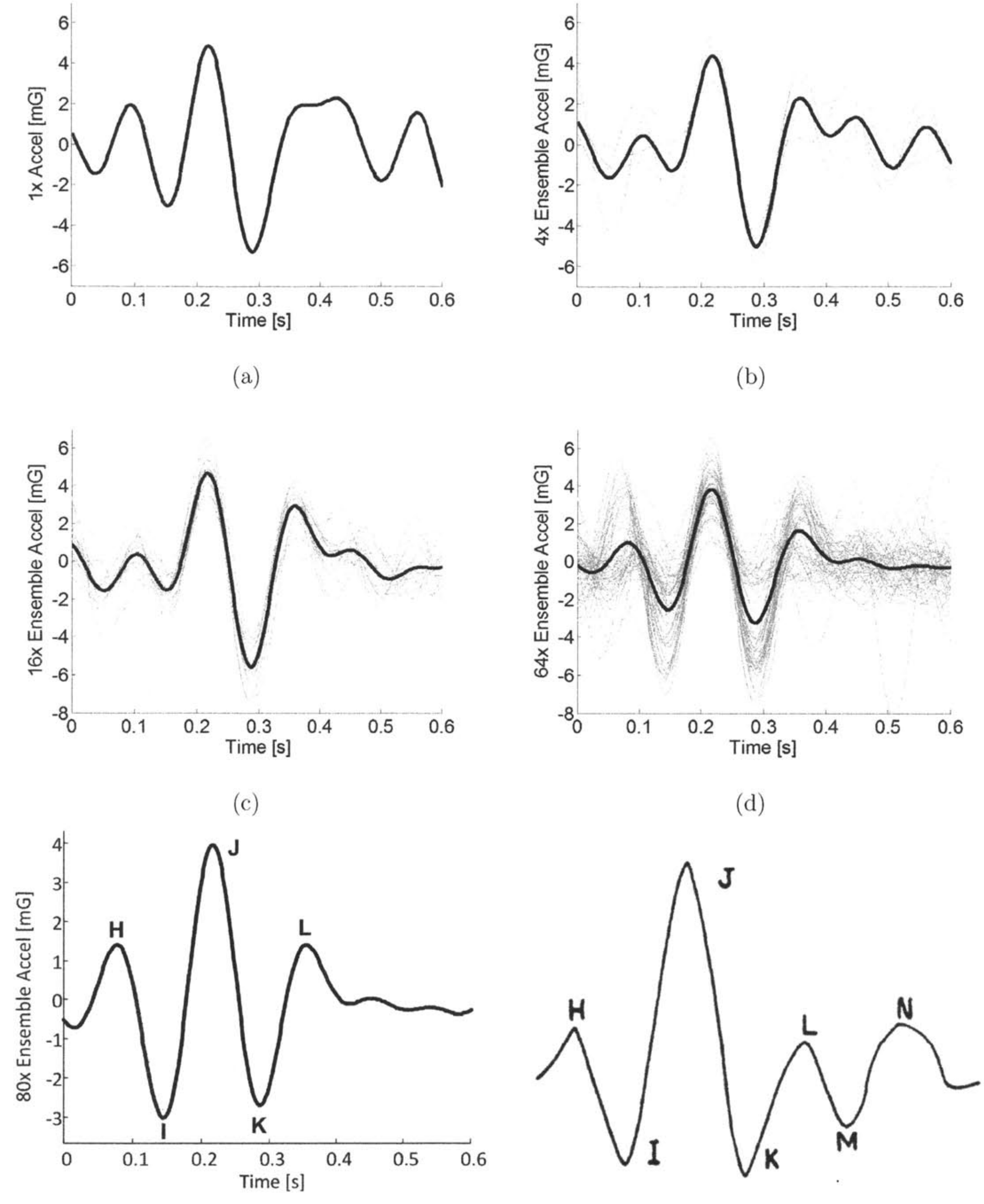

(a) (b)

(c) (d)

(e) (f)

Figure 2-15: a) The head BCG from the first beat, and the ensemble head BCG's from b) the first 4 beats, c) the first 16 beats, d) the first 64 beats, e) the first 80 beats, and f) the traditional BCG [14]. The underlying individual BCG waveforms are shown in grey. The subject's average beat-to-beat interval is $0.73s$.

2.4.2 The Head BCG Frequency Range

Figure 2-16 shows the head BCG's power spectral density of a sample head BCG measured over 60 seconds (Welch's method with $190Hz$ sampling frequency, $48s$ hamming window, $24s$ overlap, and 6064-point FFT). 89% of the total signal power resides in the range of $1Hz - 10Hz$. This is consistent with the previous BCG work, which states that the majority of the BCG's frequency content is less than $10Hz$ [33] [34]. For subsequent head BCG measurements, the signal is bandpass filtered in the range of $1Hz - 10Hz$ to remove DC gravity, sub-Hz baseline drift caused by respiration, and movement artifacts above $10Hz$.

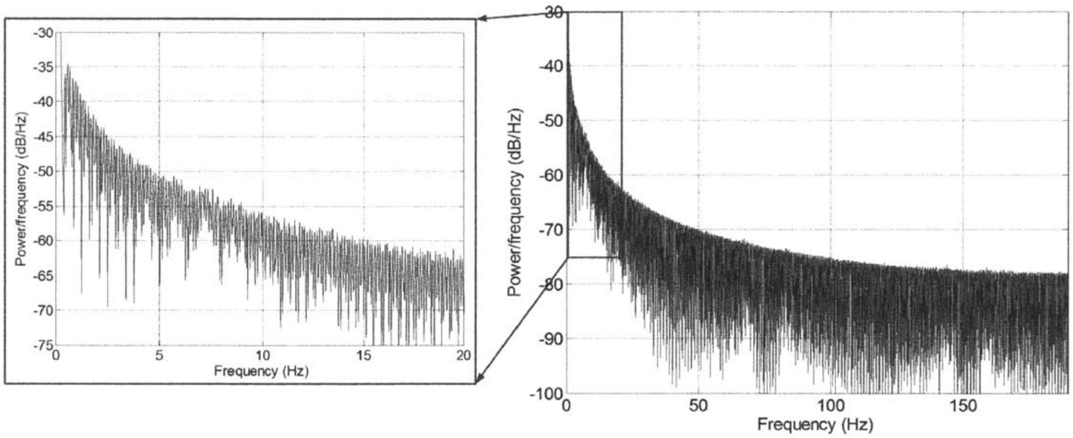

Figure 2-16: The power spectral density of a sample head BCG.

2.4.3 The Head BCG in Different Axes and Postures

Figure 2-17 shows that the head BCG in the upright standing posture exists in all three axes. However, the y-axis is the dominant BCG axis because blood volume movement is mainly in the y-axis.

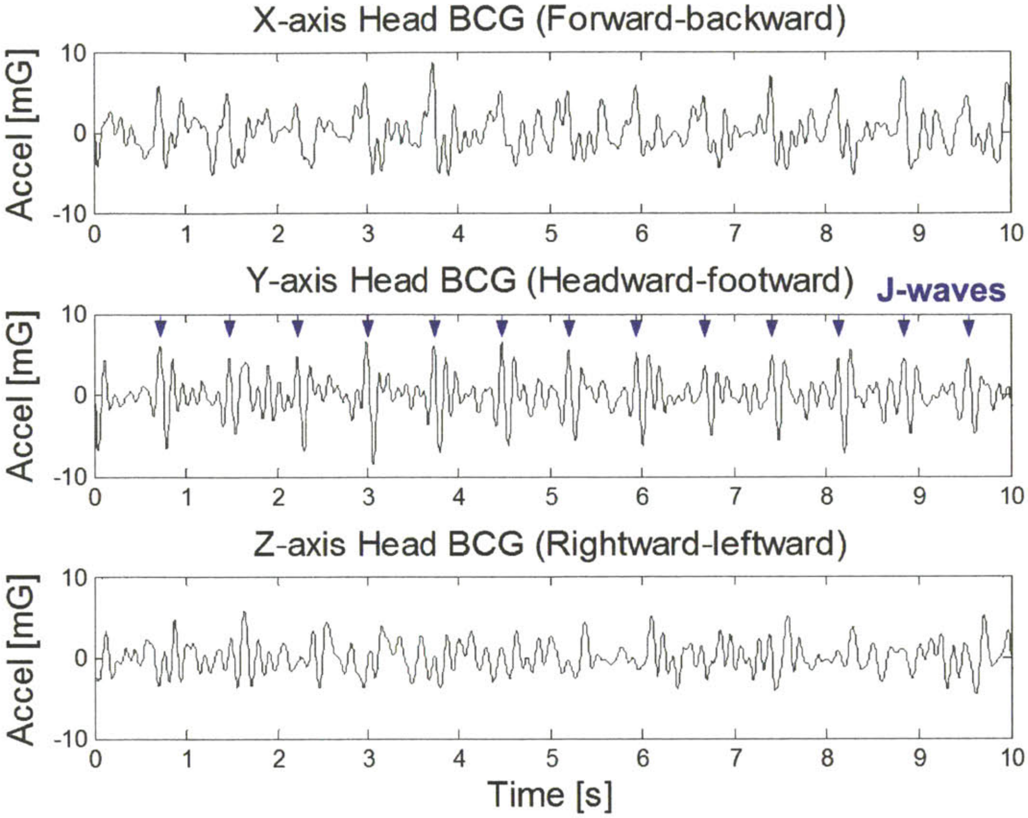

Figure 2-17: Measured tri-axial head BCG in the standing posture with J-waves annotated in the y-axis data.

To demonstrate that the head BCG can be measured in different postures, Figure 2-18 shows the y-axis (headward-footward) measurements in standing, sitting, and supine postures. The y-axis is the dominant axis of the head BCG in all three positions. However, in the supine position, the higher frequency accelerations are dampened by static friction with the stationary table.

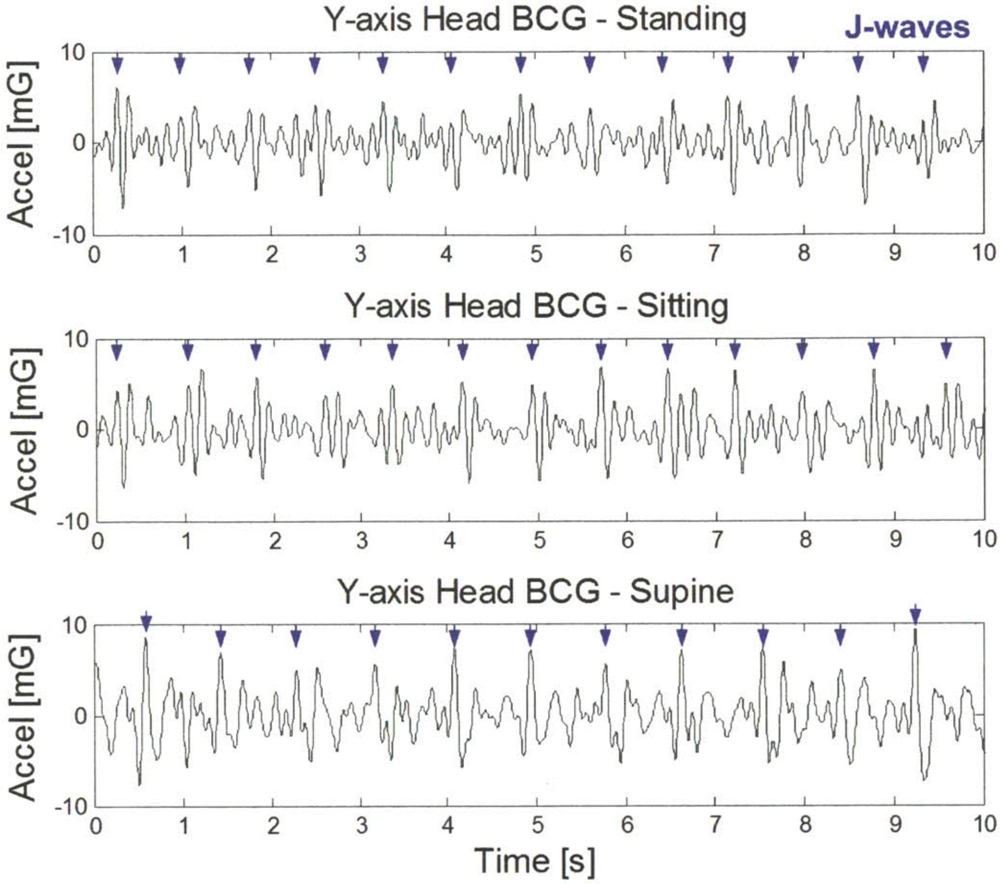

Figure 2-18: Measured y-axis head BCG in various postures with J-waves annotated.

2.4.4 The Head BCG and Stroke Volume

In Starr's pioneering work, it is mentioned that the BCG amplitude is directly related to stroke volume [14]. Physically, the movement of a larger blood mass leads to a more pronounced recoil and a higher BCG amplitude. This direct relationship is investigated using the clinical results in Chapter 5.

It should be noted that if both heart rate and SV are obtained, then cardiac output (CO) can be calculated. CO is the total volume of blood pumped by the heart per minute and is defined as the product of heart rate and SV ($CO[L/min] = HR \times SV$). CO is an important parameter of cardiac condition especially in diseases such as congestive heart failure [4].

2.4.5 Head BCG Derived Respiration

Lastly, since breathing induces physical movement, the accelerometer's baseline is modulated by respiration. In Figure 2-19, the low frequency ($0.05Hz - 0.7Hz$) baseline of the accelerometer y-axis signal is plotted with a simultaneous respiration measurement from a chest band with a strain sensor. The BCG baseline's peaks do not coincide with the chest band's peaks because the BCG signal measures y-axis acceleration while the chest band measures radial strain. However, the BCG baseline can produce the same respiratory rate ($breaths/min$) as the chest band.

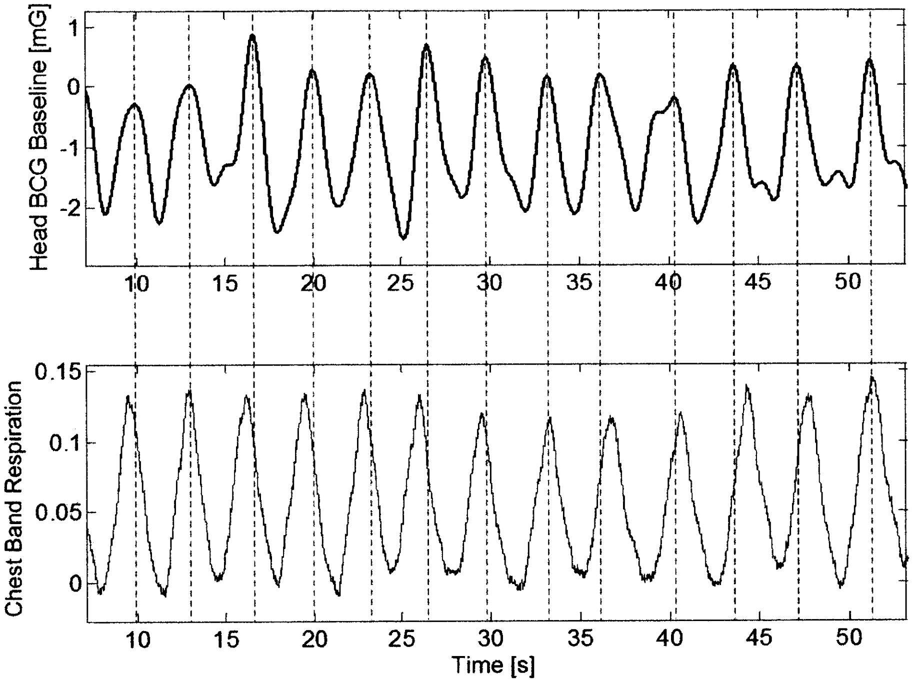

Figure 2-19: The head BCG baseline (bandpass filtered $0.05Hz - 0.7Hz$) and respiration signal simultaneously measured by a chest band.

2.4.6 Concluding Remarks

Because the head BCG is in the range of $10mG_{pp}$, it can only be measured in states of relative rest. For example, walking generates excessive acceleration of hundreds of mG's that are in the same frequency range as the head BCG, thus effectively masking the BCG signal. However, for the target application of long term wearable monitoring, it is possible to form trends from measurements throughout the day when the wearer is relatively still. Di Rienzo et al. have studied the frequency of at-rest (less than $4mG$) time segments from wearable accelerometers [35]. For example, in Figure 2-20, one can expect the subject to be still for an average of 40 20s time segments per hour during the day.

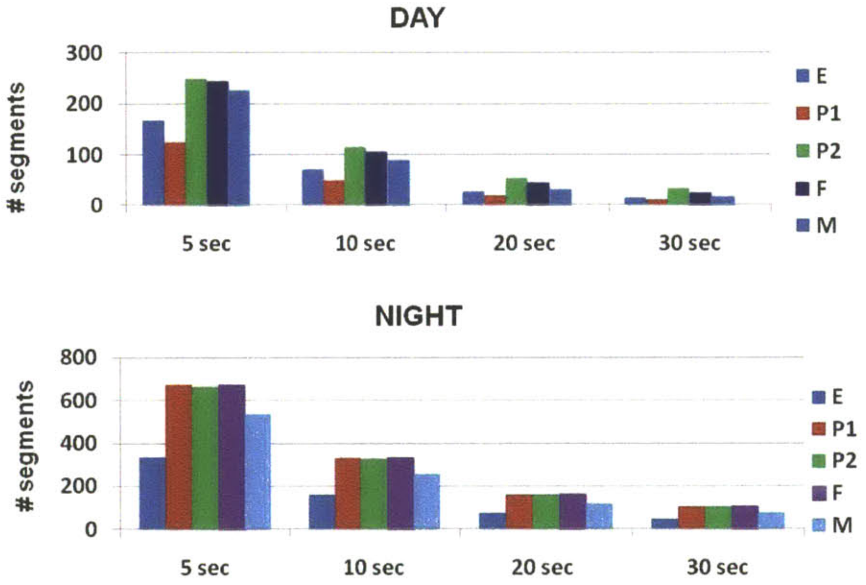

Figure 2-20: Number of at-rest segments during day and night versus segment length for five subjects. Each subject is color-coded. (figure from [35]).

By itself, the head BCG can be used for heart rate, stroke volume, and respiratory rate measurements in states of rest without the use of electrodes or adhesives. It will be shown in Chapter 4 that when BCG and ECG timings are combined, electromechanical timings can be obtained that relate to the heart's muscle function.

Chapter 3

The Electrocardiogram (ECG)

This chapter provides a background on the traditional chest electrocardiogram (ECG) and its origins. Then, the measurement of the ECG at the head is demonstrated. The head ECG's morphology is compared to that of the chest ECG using ensemble averaging as a tool. Lastly, the head ECG's frequency spectrum is compared with the chest ECG's spectrum in terms of fundamental and harmonic frequencies.

3.1 The Chest ECG

The ECG is a non-invasive surface measurement of the electrical potentials of the heart. Augustus Waller published the first human ECG using a capillary electrometer in 1887 [36]. In 1902, Willem Einthoven demonstrated the galvanometric measurement of the ECG from limbs dipped in saline solutions and began the use of the ECG as a clinical tool [37]. Using the morphologies and rhythms of different ECG vectors, the ECG is used to diagnose diseases in specific regions of the heart and has become a primary tool for the non-invasive assessment of cardiac health.

Modern measurements of the ECG use gel electrodes usually made of AgCl for its low half-cell potential. The ECG signals are usually on the order of $1mV$ and are amplified using low noise instrumentation amplifiers. Figure 3-1 shows the anatomy of the heart while Figure 3-2 shows a modern lead II chest ECG with different waves labeled.

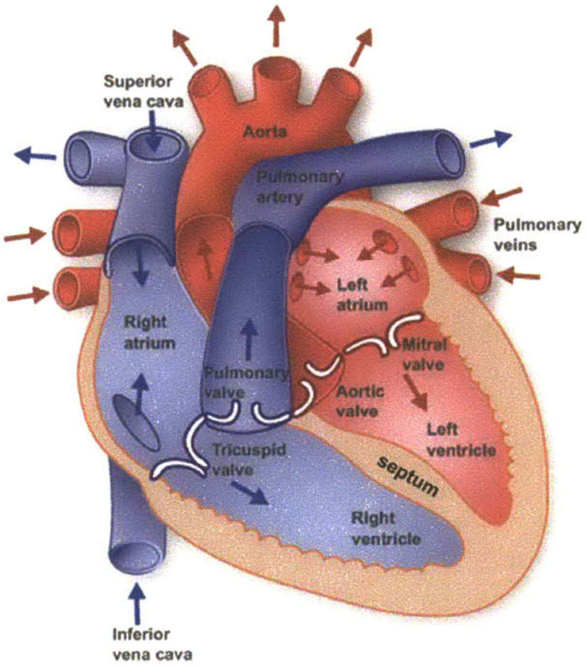

Figure 3-1: The anatomy of the heart (figure from [38]).

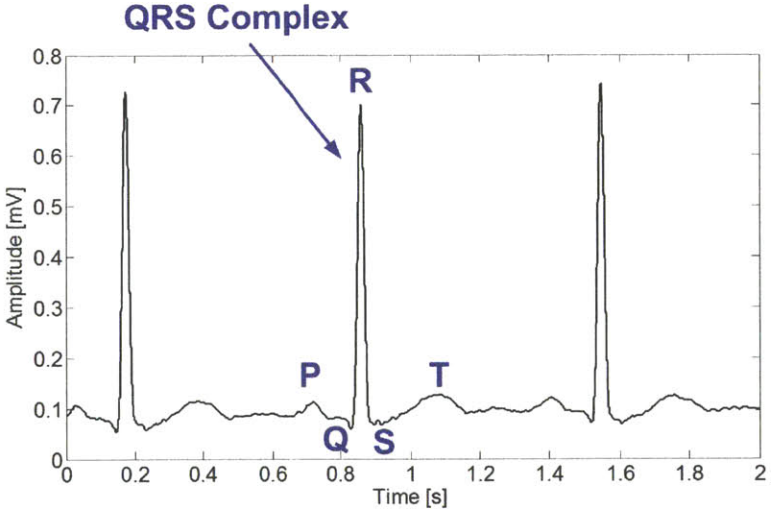

Figure 3-2: A standard lead II chest ECG with its waves labeled (measured by the ECG ASIC from Chapter 6).

In Figure 3-2, the P-wave signifies the depolarization of the atria, the QRS complex signifies the depolarization of the ventricles, and the T-wave signifies the repolarization of the ventricles.

Each differential vector measurement of the ECG is known as a "lead." The standard clinical ECG measurement uses 12 leads which are shown in Figure 3-3. Six of the leads in the plane of the body are called frontal leads. The remaining six leads (V1-V6) are pre-cordial leads perpendicular to the body.

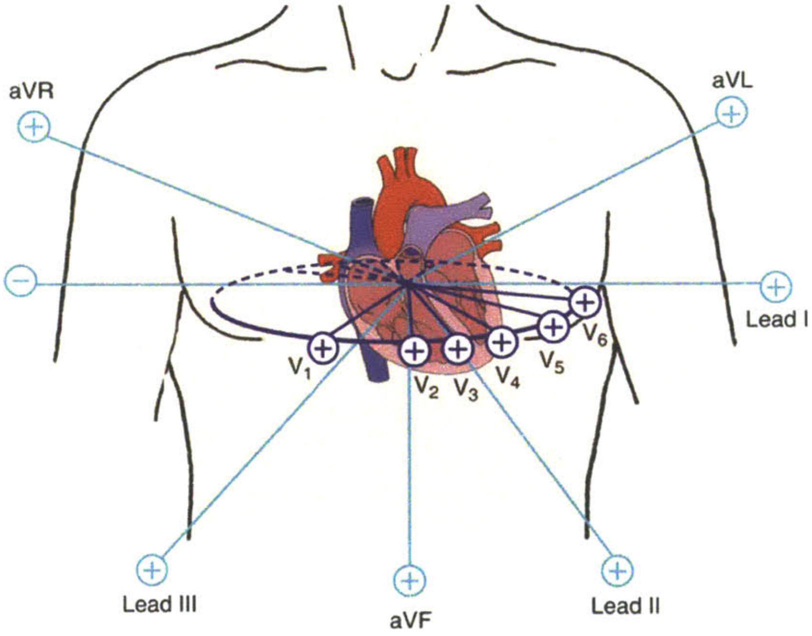

Figure 3-3: The standard 12-lead ECG (figure from [39]).

For diagnosis or monitoring purposes, it is valuable to record long term ECG during the patient's daily activities. Such a device is known as a Holter monitor, which measures one or more leads of the ECG on the chest and stores the data for analysis. Holter monitors have progressed from tape recorders to small solid state devices as shown in Figure 3-4. However, because the highest signal quality is desired, all such ECG monitors are located on the chest.

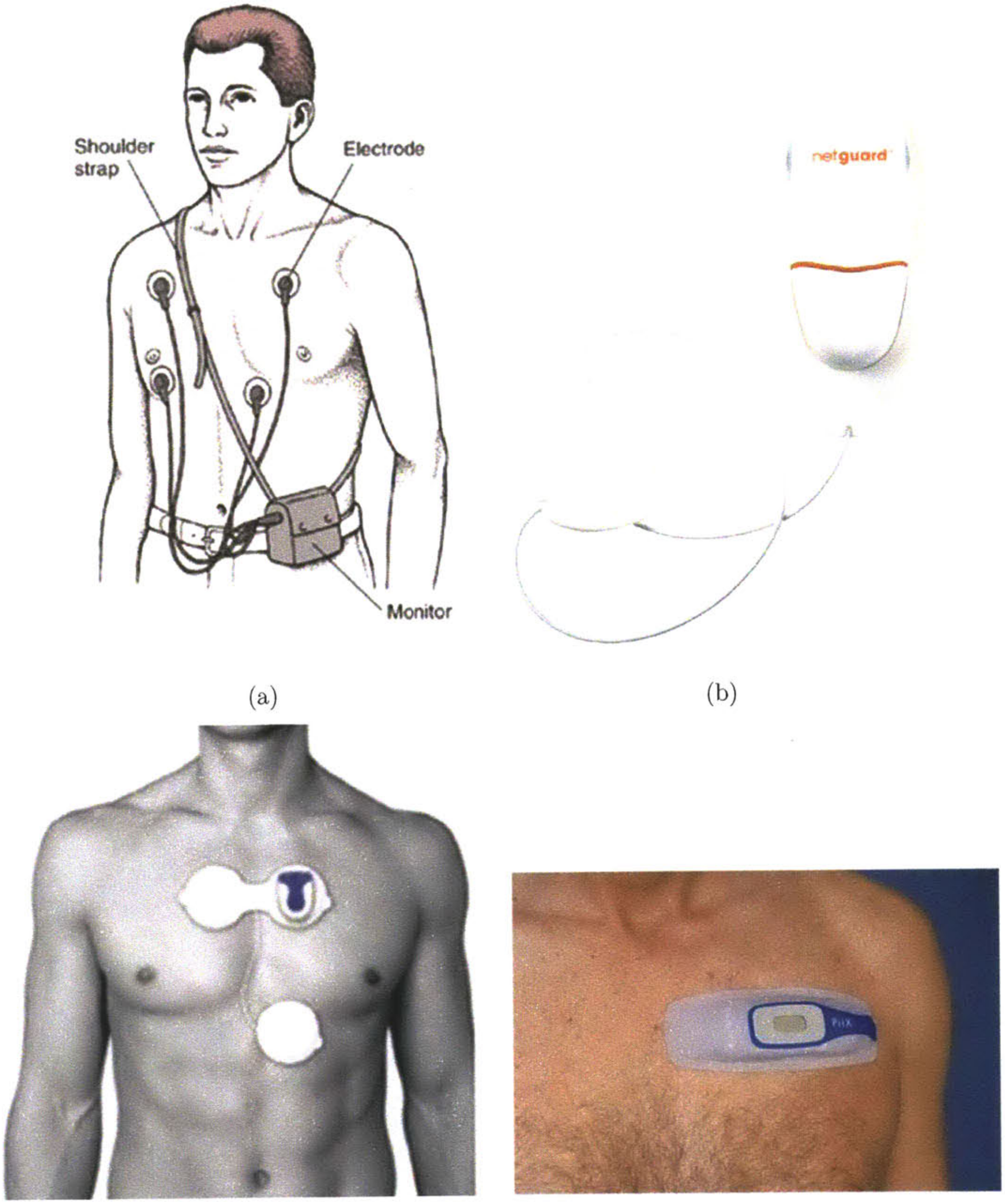

(a) (b)

(c) (d)

Figure 3-4: Traditional and modern Holter monitors: a) the traditional Holter monitor [40], b) the Mindray Netguard [41], c) the Intelesens V-Patch [42], and d) the Corventis NUVANT [43].

3.2 The Head ECG

3.2.1 Head ECG Measurements

Because the body is a conductive medium, an ECG signal from the heart can be detected elsewhere on the body in an attenuated form. To avoid ECG wires from the ear-worn heart monitor to the chest, the ECG is measured locally near the ear. One electrode is placed on the mastoid area, and the second electrode is placed on the upper middle neck. The mastoid's bony structure and the neck's flat surface allow a stable electrode contact. Together, the two electrodes measure a single-lead ECG.

Usually, a third driven-right-leg (DRL) electrode is used for common-mode feedback (CMFB). This DRL electrode aims to reduce common-mode powerline interference and to set the circuit's DC potential to the body's potential. However, because of the limited skin area near the ear, this DRL electrode is omitted. This decision leads to certain circuit design considerations as discussed below.

The ECG front-end circuit is shown in Figure 3-5.

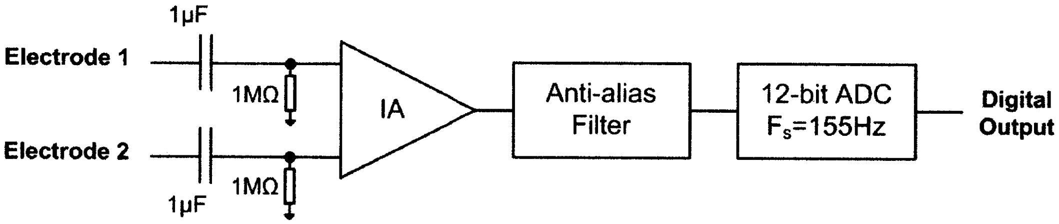

Figure 3-5: The head ECG front-end circuit.

The two differential electrodes go through a high pass filter with a corner frequency of $0.16Hz$. This high pass filter is necessary to isolate the DC voltage of the body (due to the absence of the DRL electrode) and to remove the near-DC electrode offset voltage (EOV) at the electrode-skin interface.

The filtered differential signal is amplified by an instrumentation amplifier (IA). The IA gain is adjustable to account for ECG amplitude variations across subjects. Because the ECG amplitude near the ear is in the range of $30\mu V_{pp}$, the IA's noise performance is important. The selected IA (TI INA333) has an input-referred noise that is comparable to the thermal noise generated by the $1M\Omega$ biasing resistors within a bandwidth of $78Hz$ ($1.1\mu V_{rms}$).

The amplifier output is low pass filtered at $117Hz$ to prevent the aliasing of out of band noise. Then, the signal is digitized by a 12-bit SAR ADC at a sampling frequency of 155Hz. This sampling frequency is determined by the radio bandwidth for real time transmission. Because there is no DRL electrode, powerline interference is removed by digital filters after the ECG front-end.

Using clinical AgCl electrodes, Figure 3-6 shows ECG measurements taken from the chest (lead II, $15cm$ apart, gain of 250) and from the left mastoid area ($4cm$ apart, gain of 7,000).

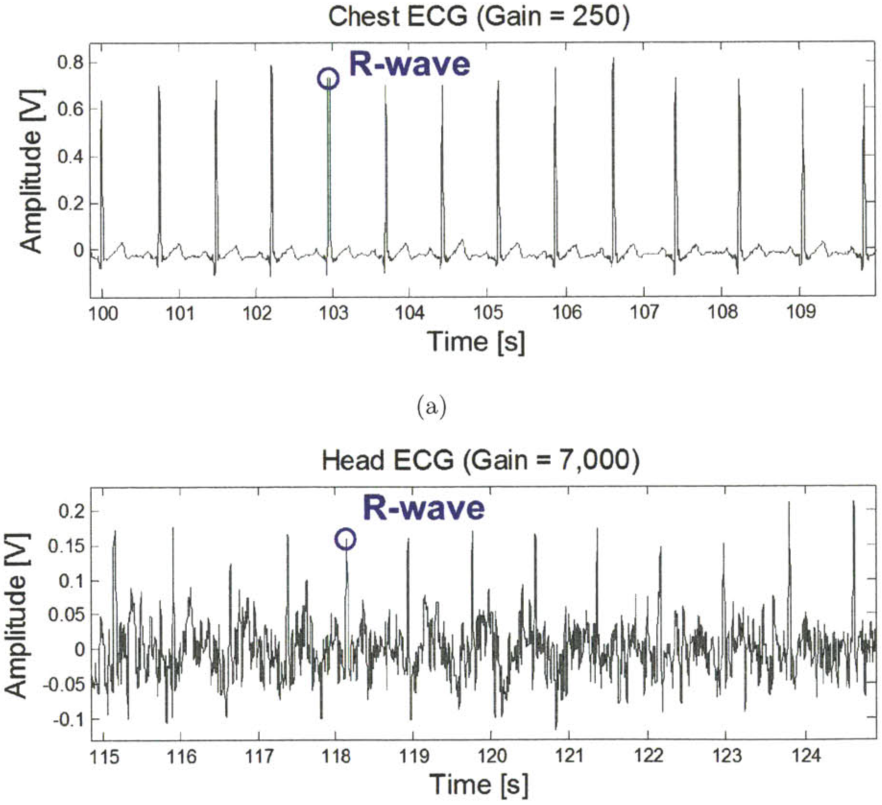

(a)

(b)

Figure 3-6: a) The ECG measured from the chest, and b) the ECG measured from the mastoid area behind the left ear. The ECG's are filtered with a $1-50Hz$ bandpass filter. Measurements are not simultaneous.

As seen in Figure 3-6, the ECG measured at the mastoid area is in the range of $30\mu V_{pp} - 40\mu V_{pp}$, which is two orders of magnitude smaller than the standard chest ECG. This attenuation is due to the pattern of the ECG field lines at the head, which yield a very small potential difference when projected onto the mastoid lead. Because of this attenuation, the head ECG has a poor signal-to-noise ratio and only R-waves are immediately visible.

3.2.2 The Head ECG Morphology

Figure 3-7 shows a longer duration of the head ECG used for ensemble averaging.

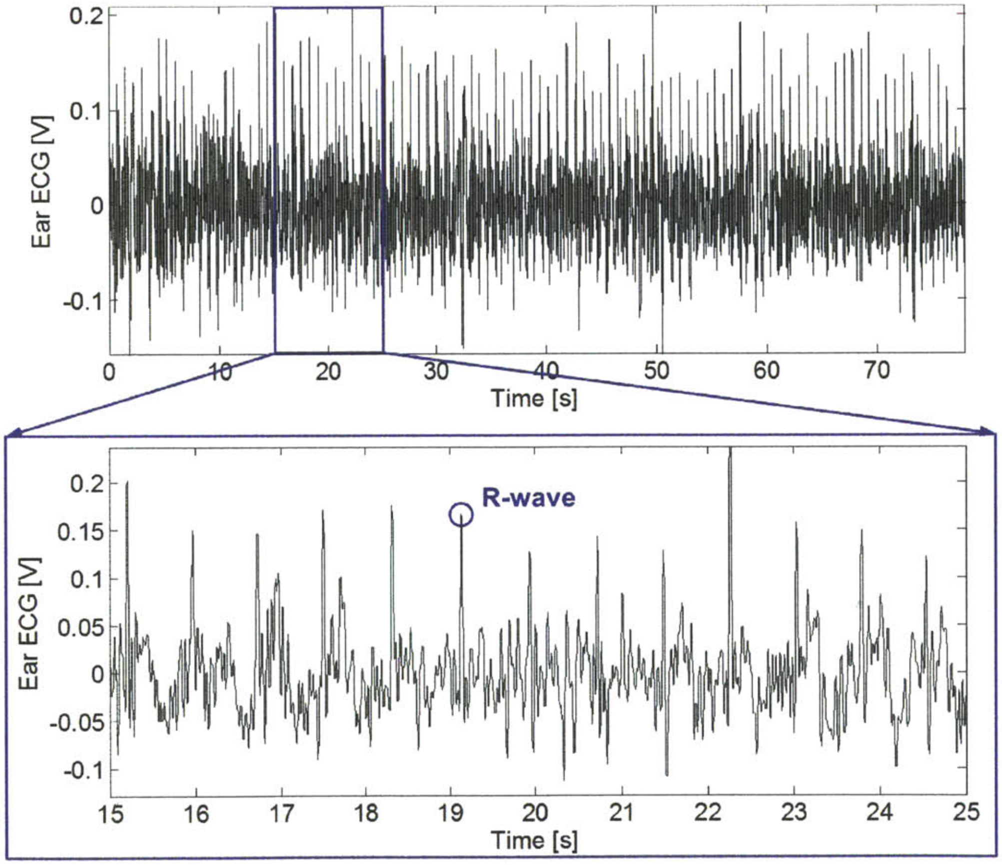

Figure 3-7: The head ECG measured over 78 seconds.

To examine the secondary ECG waves, the ensemble averages of the head ECG are created by aligning each beat's R-wave and then averaging the beats. As shown in Figure 3-8, with an increasing number of ensemble averages, P, Q, S, and T-waves become visible. For reference, Figure 3-8(f) shows an ensemble Lead II chest ECG measured from the same subject under the same heart rate immediately following the head ECG measurements. One can observe that the head ECG's wave timings are representative of the chest ECG's wave timings. This demonstrates that the mastoid-neck ECG lead can provide the standard ECG waves when ensemble averaging is used to remove uncorrelated signal fluctuations.

3.2.3 The Head ECG Frequency Content

Figure 3-9 plots the power spectral density (Welch's method with $190Hz$ sampling frequency, $8s$ hamming window, $4s$ overlap, and 6032-point FFT) of 78 seconds of the head ECG and the chest ECG from the same subject under the same average beat-to-beat interval of $0.75s$, which corresponds to $1.3Hz$ of beat-to-beat frequency. While the chest ECG's peak power content is at $1.3Hz$, the head ECG's $1.3Hz$ peak is submerged below the significant "noise" below $4Hz$. Because the ECG amplifier is chopper modulated at the inputs, its $1/f$ noise is suppressed and the amplifier input noise from $0.1Hz$ to $10Hz$ is only $1\mu V_{pp}$ (the head ECG is approximately $30\mu V_{pp}$). Therefore, the sub-$4Hz$ content in the head ECG arises from either motion artifacts or muscle signals (electromyography).

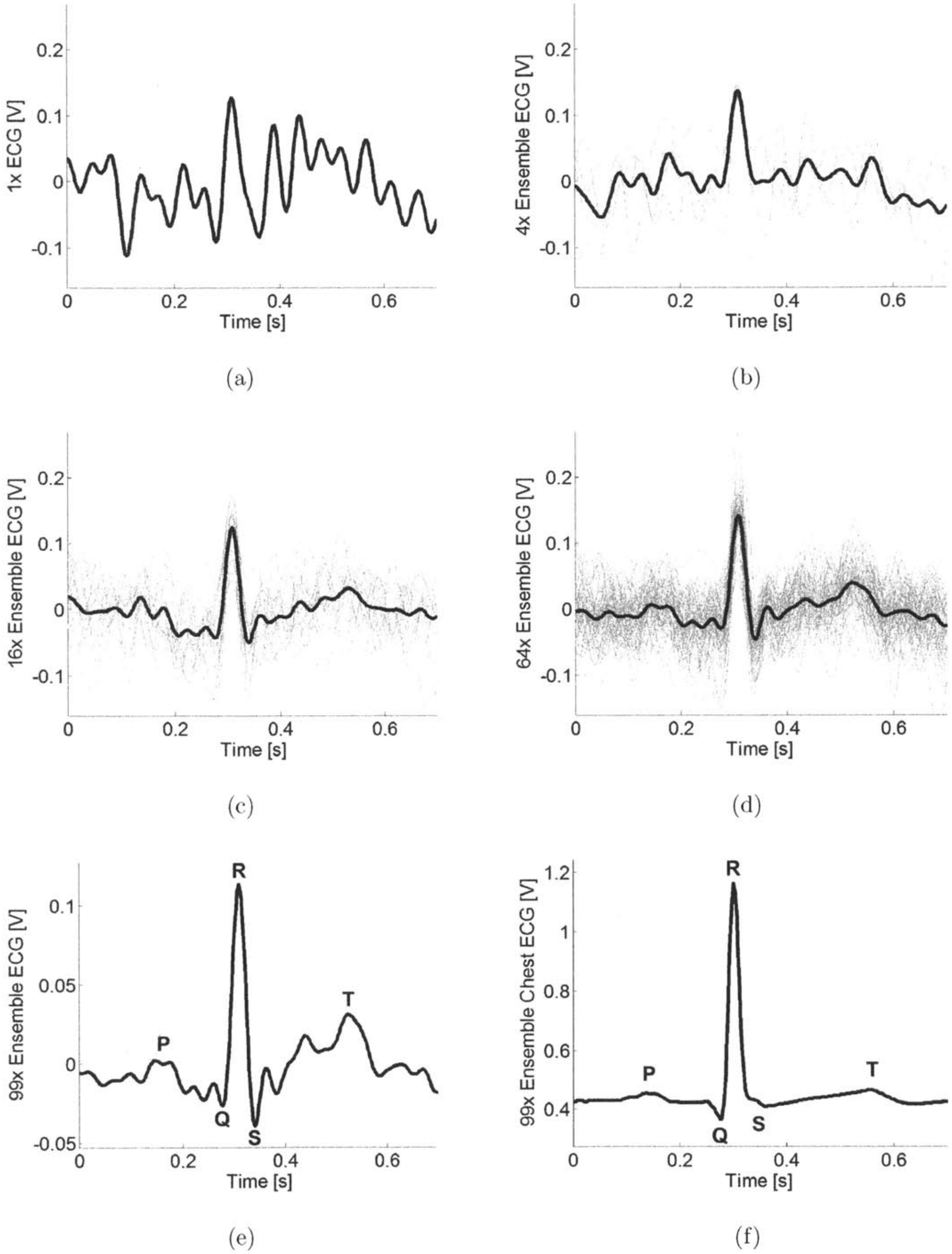

(a) (b)

(c) (d)

(e) (f)

Figure 3-8: a) The head ECG from the first beat, and the ensemble head ECG's from b) the first 4 beats, c) the first 16 beats, d) the first 64 beats, e) the first 99 beats, and f) the ensemble Lead II chest ECG from the same subject under the same heart rate. The underlying individual ECG waveforms are shown in grey. The subject's average beat-to-beat interval is $0.75s$.

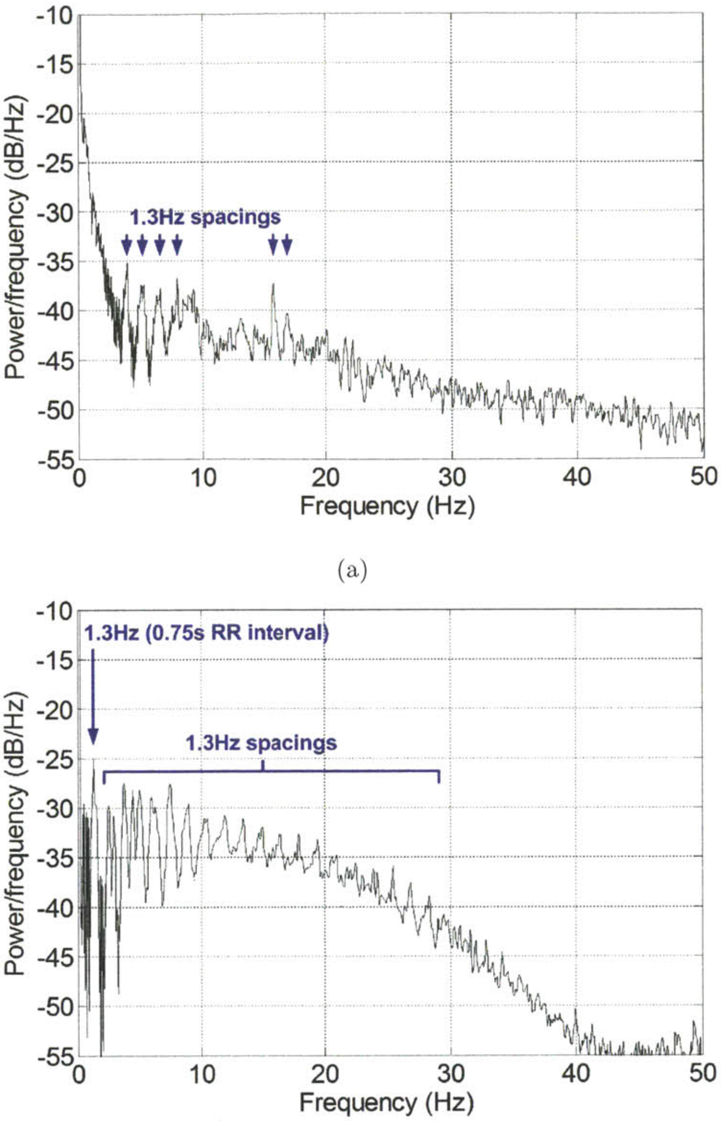

(a)

(b)

Figure 3-9: a) The power spectral density of the head ECG, and b) the power spectral density of the chest ECG from the same subject. The subject's average beat-to-beat frequency is $1.3Hz$.

The harmonics of the $1.3Hz$ fundamental beat-to-beat frequency can be seen throughout the chest ECG, but only appear intermittently in the head ECG. This is because the head ECG's morphology is not as repeatable as that of the chest ECG, thus reducing signal periodicity and harmonics.

3.2.4 Concluding Remarks

The value of the head ECG to the wearable heart monitor is in the R-wave timings. Just like the BCG's J-waves, the R-waves can be used to measure heart rate. This redundancy can be used to detect errors in heart rate data. Chapter 4 explains how the R-waves can be used in conjunction with the J-waves to derive the heart's pre-ejection period. A statistical method to extract this heart interval from low quality signals will be discussed in Section 4.1.1. A low power integrated circuit that can extract R-wave timings from the head ECG will be presented in Chapter 6.

Chapter 4

Heart Intervals

This chapter begins with the definition of pre-ejection period (PEP) and a discussion of the current non-invasive PEP measurement methods. Through timing diagrams, PEP is shown to relate to a delay interval between the ECG and the BCG called the RJ interval. A statistical method to extract the RJ interval from the ECG and the BCG is presented. Then, the photoplethysmogram (PPG) is introduced to define another interval called pulse arrival time (PAT). With PEP and PAT, pulse transit time (PTT) can be obtained. The value of PTT is in its relationship with blood pressure, which is derived based on fluid dynamics.

4.1 Pre-ejection Period (PEP)

PEP is defined as the time period from the beginning of the ECG's Q-wave, which marks the beginning of the ventricular depolarization, to the opening of the aortic valve, which marks the ejection of blood into the aorta [16].

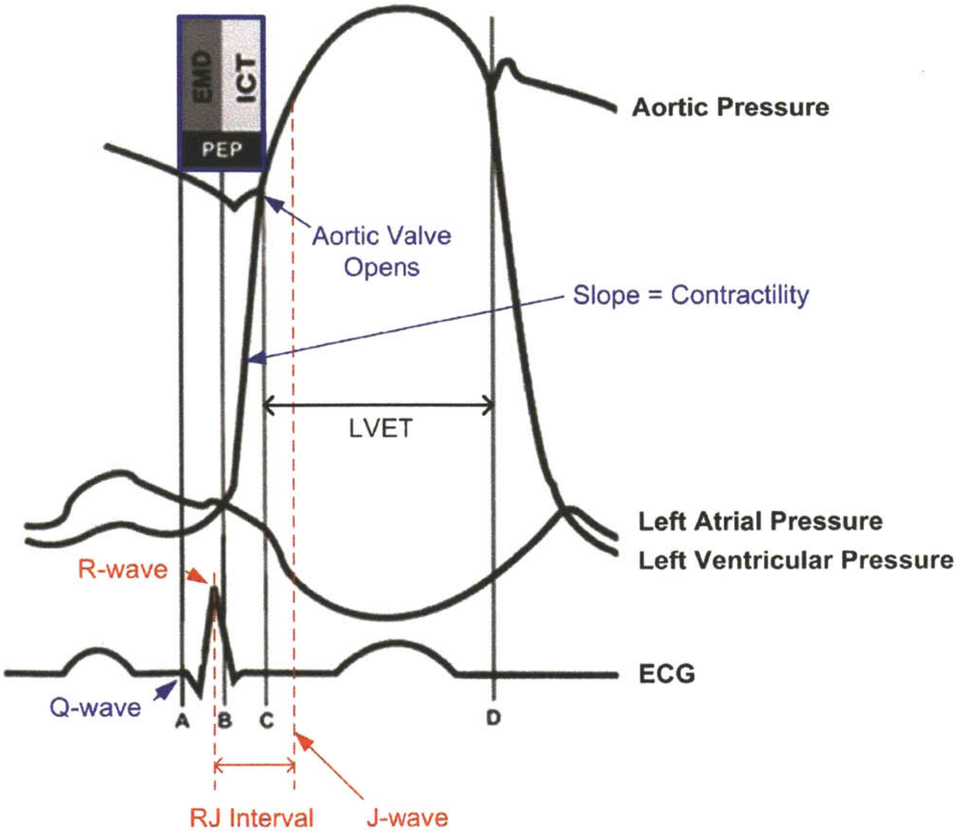

Figure 4-1: A Wiggers diagram showing the definition of PEP in the context of pressure waveforms, the ECG, and the RJ interval (figure adapted from [44]).

PEP is denoted by the period between time markers A and C in Figure 4-1. PEP is the sum of two components: electromechanical delay (EMD) and isovolumic contraction time (ICT). EMD (AB interval in Figure 4-1) is the time needed for the electrical stimulus to activate the ventricular heart muscles. Following EMD, left ventricular pressure increases until it reaches the aortic pressure. This period is ICT (BC interval in Figure 4-1). After ICT, the equalization of ventricular and aortic pressure opens the aortic valve and ventricular ejection occurs. This interval is marked by the CD interval in Figure 4-1 and is known as the left ventricular ejection time (LVET). It should be noted that the ratio of PEP to LVET ($PEP/LVET$) has an inverse relationship with stroke volume (SV), which is the volume of blood ejected per beat and correlates with cardiac function [16].

During ICT, the maximum rate of left ventricular pressure increase ($max(dP/dt)$) is a measure of contractility, which is the intrinsic ability of the heart muscle to produce force [16]. While EMD is relatively constant, ICT is highly variable because contractility changes under different sympathetic responses and cardiac diseases [45] [46] [47]. Therefore, PEP is inversely related to contractility (given a constant cardiac afterload). As a result, PEP can be used to determine left ventricular performance in patients with cardiovascular disease such as cardiomyopathy and abnormal left ventricular contractions [5] [6].

There are several non-invasive methods to measure PEP. The impedance cardiogram (ICG) is widely used in conjunction with the ECG as a non-invasive method to measure PEP. The ICG uses thoracic impedance (Z), which is measured by applying a continuous AC current through the chest and sensing the resulting AC voltage ($Z = V/I$). The ICG current flows through the aorta, which provides a path of least resistance due to its blood volume. The time derivative of impedance (dZ/dt) is the ICG signal [48].

Figure 4-2 shows simultaneously measured ECG, the absolute change of thoracic impedance from baseline (ΔZ), and ICG (dZ/dt). During PEP, there is minimal blood volume in the aorta, which sets the baseline impedance. At the end of PEP, the opening of the aortic valve causes an increase in aortic blood volume and a decrease in impedance (conventionally marked by an increase in ΔZ in literature), which leads to a beginning of incline in the ICG marked by the B-wave. After the blood has been ejected from the left ventricle, the aortic valve closes and causes a drop in aortic blood volume and an increase in impedance (conventionally marked by a decrease in ΔZ). This is marked by a local minimum in the ICG known as the X-wave. Therefore, PEP can be measured by the delay between the ECG's Q-wave and the ICG's B-wave. The interval between the ICG's B-wave and X-wave is LVET. Using both PEP and LVET, the ICG can calculate SV.

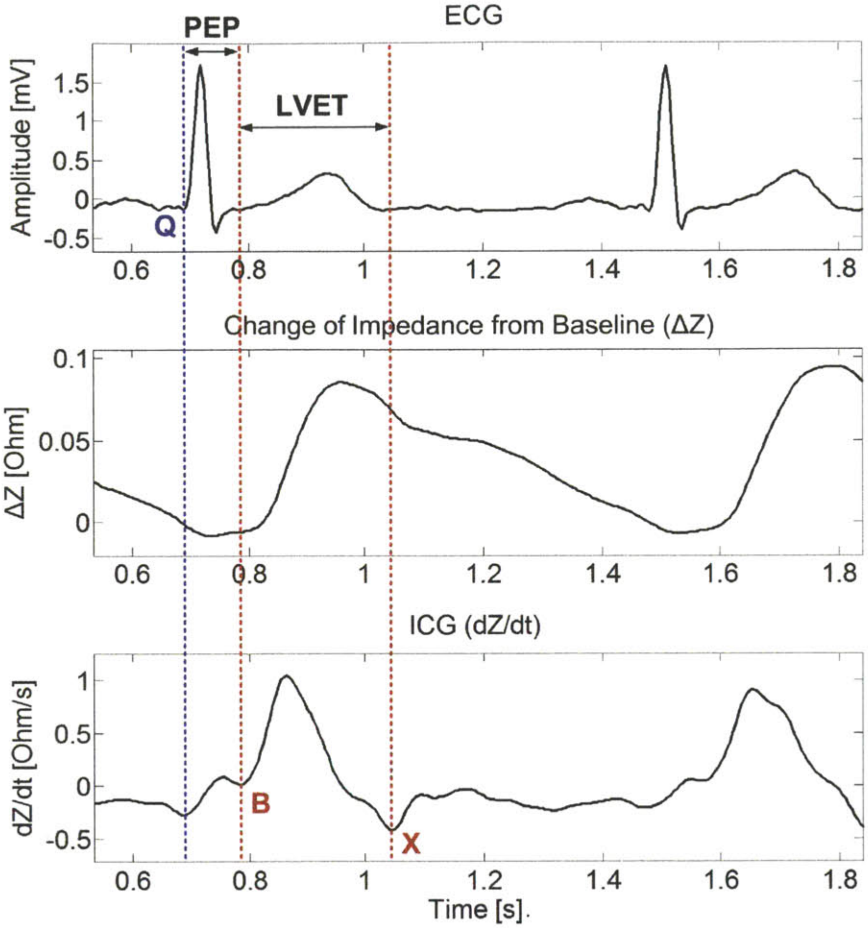

Figure 4-2: Simultaneous ECG, thoracic impedance, and ICG measured by the BioZ ICG machine on a subject.

Another method to measure PEP is to use echocardiography with the ECG. Echocardiography uses ultrasound to determine blood flow in the heart. Therefore, by measuring the delay from the ECG's Q-wave to the left ventricular ejection, PEP can be obtained. An echocardiogram with the ECG is shown in Figure 4-3, where PEP and LVET are denoted.

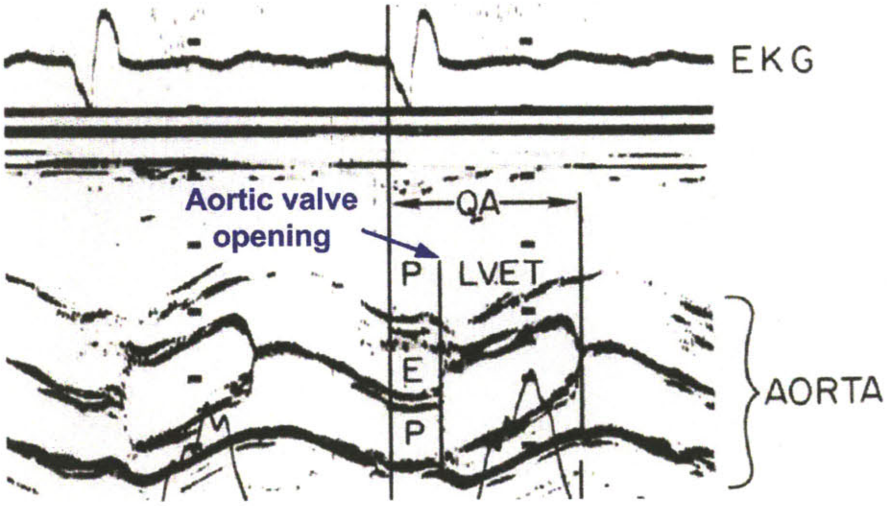

Figure 4-3: Simultaneous ECG and aorta echocardiogram with PEP and LVET shown (figure from [49]).

In all methods mentioned above, the PEP measurement requires a large stationary apparatus and in the case of echocardiography, a trained operator. Currently, no portable measurement method of PEP exists.

4.1.1 Estimating the PEP using the RJ interval

When combined, the BCG and the ECG can be used to extract the RJ interval. The RJ interval is defined as the interval between the ECG's R-wave and the BCG's J-wave. In terms of cardiac events, the RJ interval is the delay between the left ventricular depolarization and when the ejected blood reaches maximum acceleration in a major artery such as the descending aorta [22] [45] [46].

Figure 4-4 shows the RJ interval denoted on simultaneously measured head ECG and head BCG. As shown in Figure 4-1, the RJ interval includes ICT and an offset. Because PEP also consists of ICT and an offset (EMD), the RJ interval is linearly related to PEP. From previous work, linearity is indeed observed between the RJ interval and PEP from foot scale measurements of BCG [45].

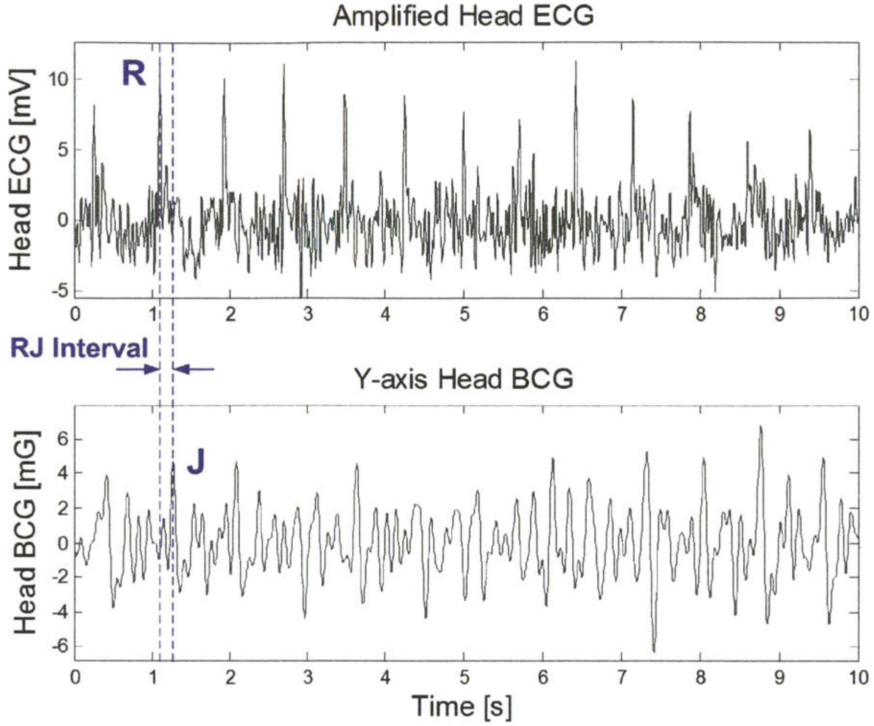

Figure 4-4: Simultaneously measured head ECG and head BCG with the RJ interval labeled.

Extracting the RJ interval using Cross-correlation

To measure the RJ interval, the simplest method is to use a peak detection algorithm to determine the delay between the ECG's R-wave and the BCG's J-wave. However, as shown in Figure 4-4, the BCG and ECG signals at the head have low amplitudes in the respective ranges of $10mG_{pp}$ and $30\mu V_{pp}$, thus leading to low signal-to-noise ratios where a peak detection algorithm would be prone to error.

Instead, cross-correlation is proposed as a statistical method for determining the RJ interval. Cross-correlation between two real signals is defined in Equation (4.1), where the cross-correlation at a particular time is the dot product of the first signal and a time-shifted version of the second signal. Maximum cross-correlation occurs when the shape of the time-shifted version of the second signal most closely resembles the shape of the first signal.

$$(f \star g)[n] \overset{\text{def}}{=} \sum_{m=-\infty}^{\infty} f[m]g[n+m] \tag{4.1}$$

This method takes advantage of the fact that both head BCG and head ECG waveforms have a similar morphology and are phase-locked to a lag index equal to the RJ interval. Instead of relying on peak detection of individual beats, this method's noise tolerance is provided by statistical information from multiple beats.

To demonstrate this, Figure 4-5 shows a time window of head ECG signal cross-correlated with a simultaneous head BCG signal. The highest peak of the cross-correlation result occurs when the R-wave of the ECG and the J-wave of the BCG coincide during time-shifting. As expected, the lag index of the highest cross-correlation peak is the RJ interval.

To reduce the amount of computation, cross-correlation can be limited to a lag range of $0.1s$ to $0.3s$ because the RJ interval is physiologically within this range [21]. This range is shown as the shaded region in Figure 4-5(b). For example, if the time window is $8s$ long, then this $0.2s$ truncation allows a 97.5% computational saving compared to a complete cross-correlation. Another benefit to this truncation is that it removes nearby cross-correlation peaks from consideration, thus improving peak confidence.

Additional cross-correlation peak confidence can be achieved by lengthening the time windows of the BCG and ECG signals. This uses more R-waves and J-waves to calculate the correct correlation at the cost of smoothing higher frequency features of the RJ interval and increasing the amount of computation. To quantify the cross-correlation peak confidence versus time window length, we use the ratio of the highest cross-correlation peak (within $0.1s - 0.3s$) magnitude to its adjacent peak (with positive lag) magnitude (see circled peaks in Figure 4-5(b)). A higher ratio means greater confidence that the highest cross-correlation peak corresponds to the RJ interval. Figure 4-6 plots this ratio versus time window length for a sample data segment.

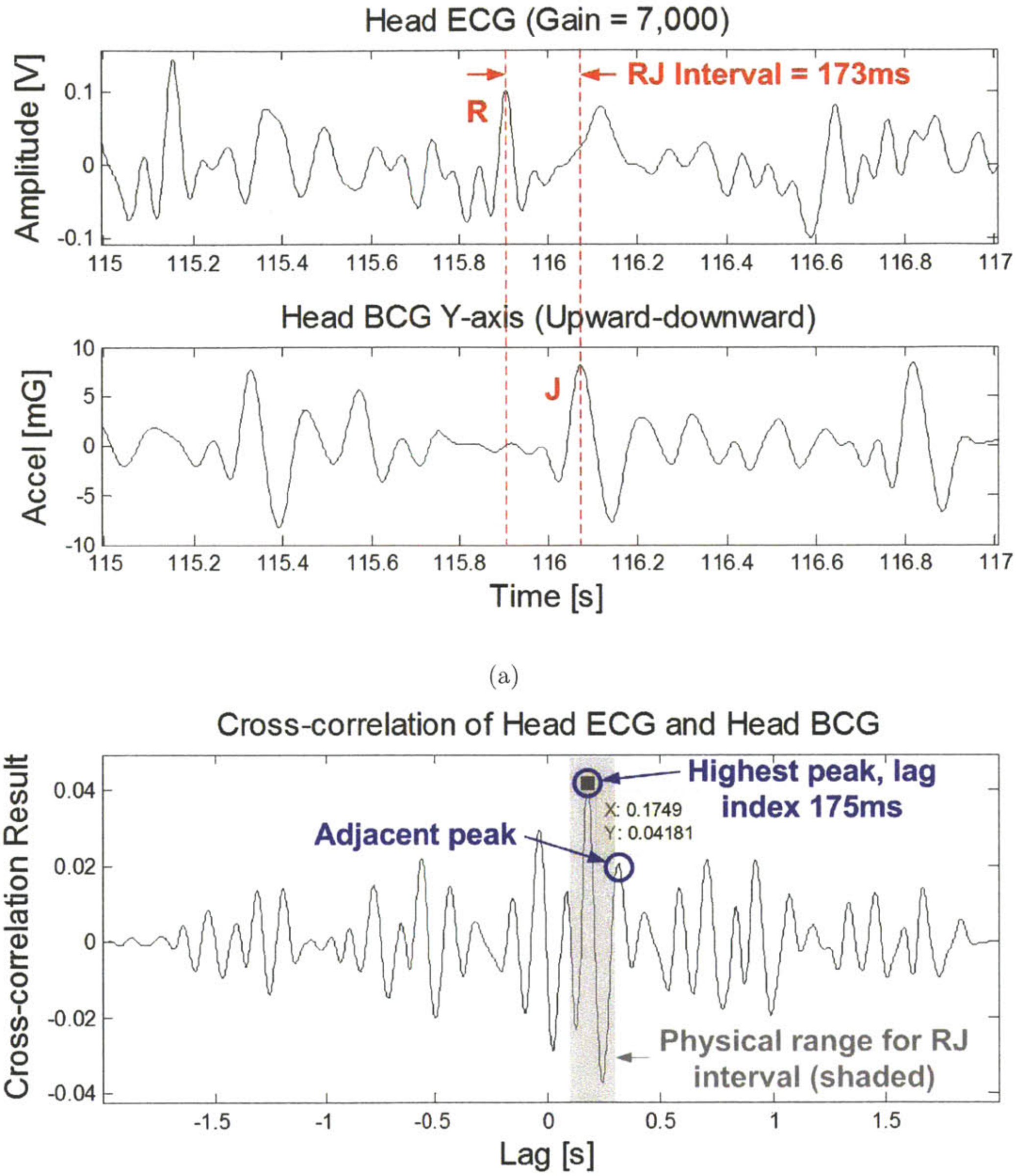

(a)

(b)

Figure 4-5: a) Simultaneous time windows of the head ECG and the head BCG, and b) the cross-correlation result showing that the highest peak's lag index is the RJ interval. The highest peak and the adjacent peak (with positive lag) are circled in blue.

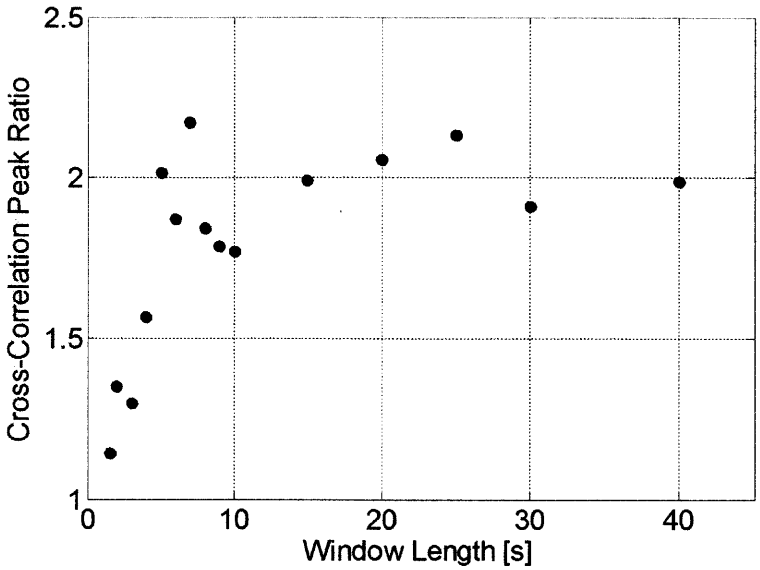

Figure 4-6: The ratio of the highest cross-correlation peak (within $0.1s - 0.3s$) magnitude to its adjacent peak (with positive lag) magnitude, plotted versus cross-correlation window length.

In Figure 4-6, it can be seen that after the window length reaches $6s$, a point of diminishing return is reached where additional signals are sufficiently similar that there is no improvement in cross-correlation peak confidence. In the clinical test in Chapter 5, a window length of $8s$ is chosen to reliably extract the RJ intervals from measured ECG and BCG data.

4.2 Pulse Arrival Time (PAT)

The photoplethysmogram (PPG) is an optical volumetric measurement of blood by sensing changes in light absorption. The PPG is usually obtained with a pulse oximeter (Figure 4-7), which measures optical transmission at the finger to determine heart rate and peripheral oxygen saturation (SpO_2). The mastoid area behind the ear contains bony structures that allow reflectance PPG to be measured. Figure 4-8 demonstrates that simultaneously measured reflectance ear PPG and transmittance finger PPG have the same underlying morphology, which consists of a principal peak signifying the arrival of the pulse wave, and a secondary peak signifying the reflected pulse wave. The work on PPG measurements is being done by Eric Winokur.

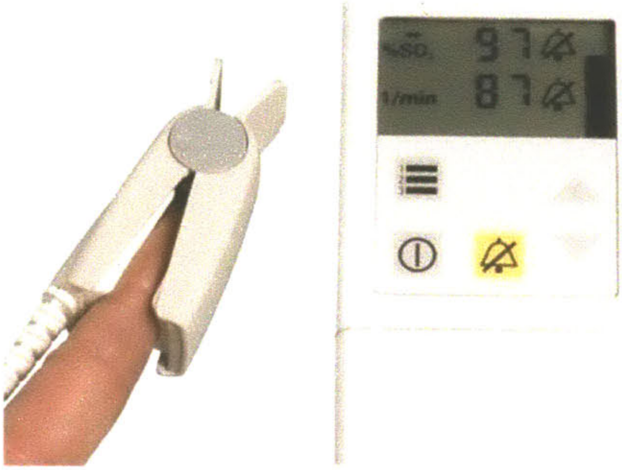

Figure 4-7: A finger clip pulse oximeter uses the PPG to measure heart rate and blood oxygenation (figure from [50]).

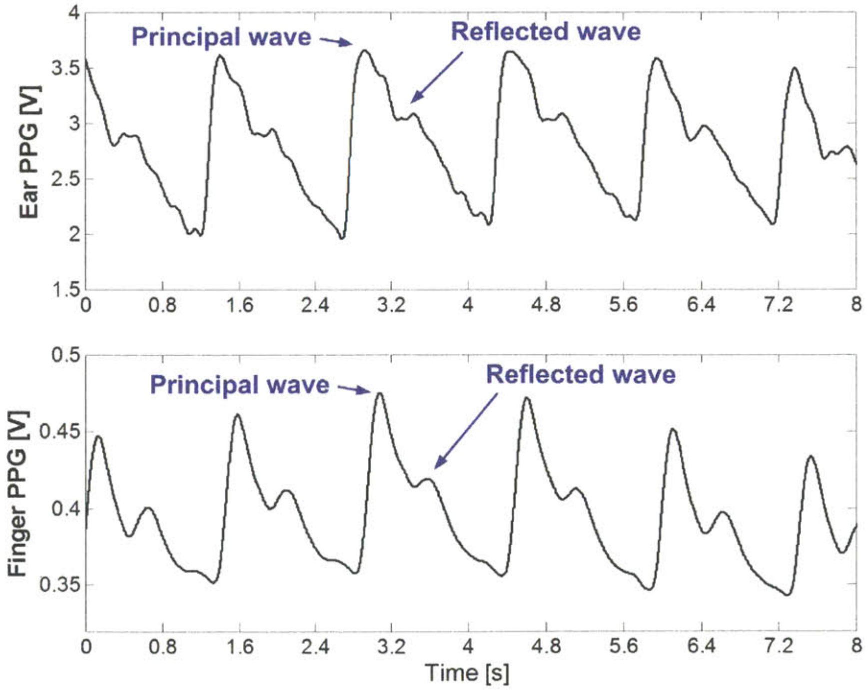

Figure 4-8: Simultaneously measured reflectance ear PPG and transmittance finger PPG showing the principal and reflected waves.

Pulse arrival time (PAT) is defined as the delay between the ECG's Q-wave and the point of the PPG's maximum positive slope. This is illustrated in Figure 4-9. It is worth noting that most current work uses the ECG's R-wave instead of Q-wave due to R-wave's ease of detection [51] [52].

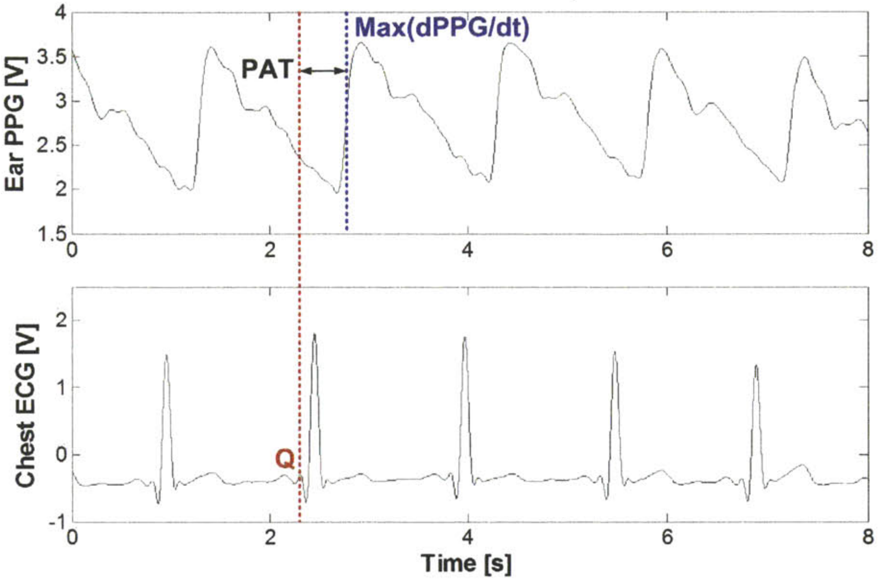

Figure 4-9: Pulse arrival time (PAT) is defined as the interval between the ECG's Q-wave and the PPG's maximum increase.

Physiologically, PAT signifies the entire interval from the beginning of the heart's depolarization to the arrival of the blood pulse wave at a peripheral location. PAT's usefulness arises from its relation with PEP and pulse transit time (PTT), as will be explained in the next section.

4.3 Pulse Transit Time (PTT)

PTT is defined as the time interval for a blood pulse wave to travel between two locations in the artery. Figure 4-10 shows the chronological order of cardiac timings starting with the ECG's Q-wave, which is the beginning of ventricular depolarization. Q-wave also marks the beginning of PEP, during which the heart builds its internal pressure to eject blood. The opening of the aortic valve marks the end of PEP.

At this moment, the blood pulse wave starts its transit to the peripherals and PTT begins. At the peripherals, the point of the PPG's maximum positive slope marks the local arrival of the pulse wave, or the end of PTT. The entire duration between the ECG's Q-wave and the point of the PPG's maximum positive slope is PAT. Therefore, $PAT = PEP + PTT$ [51] [52].

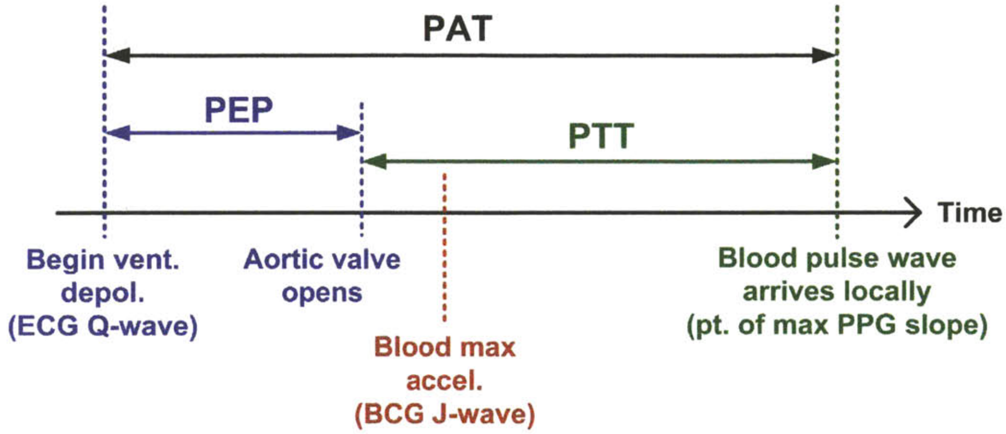

Figure 4-10: The relationship between PAT, PEP, and PTT.

Since PAT can be measured using the ECG and the PPG, and PEP can be estimated by measuring the RJ interval between the ECG and the BCG, then PTT can be estimated using the ECG, BCG, and PPG. In fact, only the BCG and the PPG are needed for PTT. This is because the delay between the BCG's J-wave and the PPG's maximum slope consists purely of PTT, as shown in Figure 4-10.

PTT is important due to its relationship with blood pressure [51] [53] [54]. This relationship is derived using the Moens-Korteweg equation (Equation (4.2)), which relates PTT to the arterial wall elasticity, E [55] [56].

$$PTT = \frac{L}{PWV} = \frac{L}{\sqrt{\frac{Eh}{2\rho r}}} \tag{4.2}$$

In Equation (4.2), L is the arterial length, PWV is the pulse wave velocity, E is the modulus of elasticity (or Young's modulus) of the arterial wall, h is the arterial wall thickness, ρ is the blood density, and r is the average arterial radius. It is assumed that h, ρ, and r remain relatively constant while E undergoes the largest variations.

E can be related to arterial wall pressure using Hughes equation (Equation (4.3)), where E_o is a subject dependent elasticity parameter, $\alpha \approx 0.017mmHg^{-1}$, and P is the arterial pressure [57]. Equation (4.3) states that a greater arterial wall pressure leads to a greater modulus of elasticity, or a stiffer artery.

$$E = E_o e^{\alpha P} \tag{4.3}$$

Combining Equations (4.2) and (4.3) yields Equation (4.4), which shows a logarithmic relationship between PTT and arterial wall pressure P. Constants A and B are subject-dependent parameters that can be solved through calibration with cuffed blood pressure measurements. Once the constants are determined, PTT can be used for cuffless blood pressure estimation.

$$\begin{aligned} P &= A\ ln(PTT) + B \\ \text{where}: & \\ A &= -\frac{2}{\alpha} \\ B &= \frac{1}{\alpha} ln\left(\frac{2L^2\rho r}{E_o h}\right) \end{aligned} \tag{4.4}$$

The majority of the work on PTT relates the estimated blood pressure P to diastolic blood pressure (DBP) because the blood pulse wave transits a vessel at the end of diastole [58] [59] [60]. Through the use of the PPG morphology such as the reflected peak timing (reflected waves travel in vessels pressurized in the systolic state, Figure 4-8), estimates of both systolic blood pressure (SBP) and DBP have been preliminarily demonstrated [61] [62]. However, more clinical work is needed to determine the relation of PTT-estimated blood pressure to DBP, SBP, and mean arterial pressure (MAP).

Chapter 5

The Clinical Test

The goal of the clinical test is to validate the ability of the wearable heart monitor to measure heart rate, stroke volume (SV), and pre-ejection period (PEP). To achieve this, reference clinical equipment and noninvasive hemodynamic maneuvers are applied on 13 test subjects. This chapter first introduces the wearable heart monitor system. Then, the design of the clinical test is explained with the goal of achieving the desired hemodynamic responses. The measurement results are analyzed to characterize the head BCG morphology across test subjects and to assess the ability of the device to measure heart rate, SV, and PEP.

5.1 The Clinical Prototype

The wearable clinical prototype's function is to measure the BCG, ECG, and PPG at the ear and to send the data to a computer for visualization, recording, and analysis. A block diagram of the system is shown in Figure 5-1.

5.1.1 The Device Hardware

The BCG accelerometer is a tri-axial MEMS accelerometer with digital output. Because the head BCG is in the range of $10mG_{pp}$, a highly sensitive and low noise accelerometer is needed. Bosch's BMA180 accelerometer is chosen for its 14-bit reso-

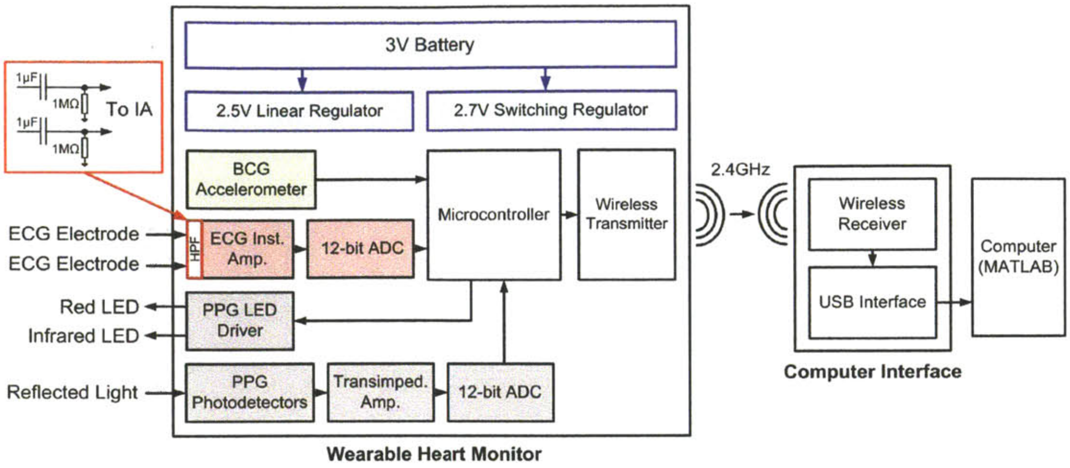

Figure 5-1: The system block diagram of the wearable heart monitor with arrows indicating the signal path.

lution and $0.69mG_{rms}$ of measured noise at $10Hz$ bandwidth with $\pm 2G$ range. Furthermore, BMA180 has a configurable integrated digital low pass filter that can be set at $10Hz$.

The ECG front-end uses a low noise instrumentation amplifier (INA333) and a 12-bit SAR analog-to-digital converter (ADC) (AD7466) to amplify and digitize the single-lead ECG from two gel electrodes. INA333 has an input noise of $0.16\mu V_{rms}$ for $0.1Hz - 10Hz$, which is sufficiently low to sense the $30\mu V_{pp}$ of head ECG. As shown in Figure 5-1, there is a high pass filter ($0.16Hz$) at the inputs to isolate DC voltages and to remove electrode offsets. This is necessary because there is no third electrode to equalize the circuit ground to the body.

The PPG front-end uses an LED driver (AD5398) that powers a red and an infrared LED. To measure the light reflection, four photodetectors (PDB-C160SM) are used in parallel. The signals from the photodetectors are amplified by a transimpedance amplifier (LMV341) and are digitized using a 12-bit SAR ADC (AD7466). The PPG front-end is designed by Eric Winokur.

The microcontroller (MSP430) continuously samples the BCG, ECG, and PPG sensors and sends the data to the radio using an SPI interface. The microcontroller also controls the PPG front-end to output the correct LED intensity and to correctly bias the PPG transimpedance amplifier.

The radio is a CC2500 2.4GHz low power wireless transceiver using the open source SimpliciTI protocol. The radio communicates wirelessly with a USB receiver that is attached to a computer.

The power management circuit draws power from a single 3V 220mAh lithium coin cell battery (CR2032) and consists of a DC-DC regulator (TPS60242) and a linear regulator (ADP150). The digital circuits are powered from the DC-DC regulator at 2.7V, and the analog circuits are powered from the linear regulator at 2.5V.

The computer interface consists of a CC2500 transceiver and a MSP430 microcontroller, which sends the received data to a UART-to-USB interface IC (FT232RL). The USB IC creates a virtual COM port that can be accessed by computer software. The computer records, plots, and filters the BCG, ECG, and PPG data in real time using MATLAB.

The entire prototype is shown in Figure 5-2 with labeled components. The microcontroller and the radio are on the red colored daughter board, which is attached to the main board using a header. The PPG board is attached to the main board through an integrated flex board that is designed to bend 180° so that the PPG LED's and photodiodes rest on the mastoid of the wearer.

The PCB's are mechanically supported by a modified hearing aid housing manufactured by Taising Hearing Amplifier Ltd. The device is anchored to the ear using the attached earbud. Two ECG electrodes are attached to the ear and neck area using 3M Red Dot AgCl gel electrodes. The PPG board is folded 180° backwards onto the mastoid area behind the ear. All components on the side facing the wearer are coated in parylene to ensure electrical isolation as part of clinical safety requirements. Figure 5-3 shows the device being worn at the ear with the ECG electrodes applied and with the PPG board on the mastoid area hidden from view.

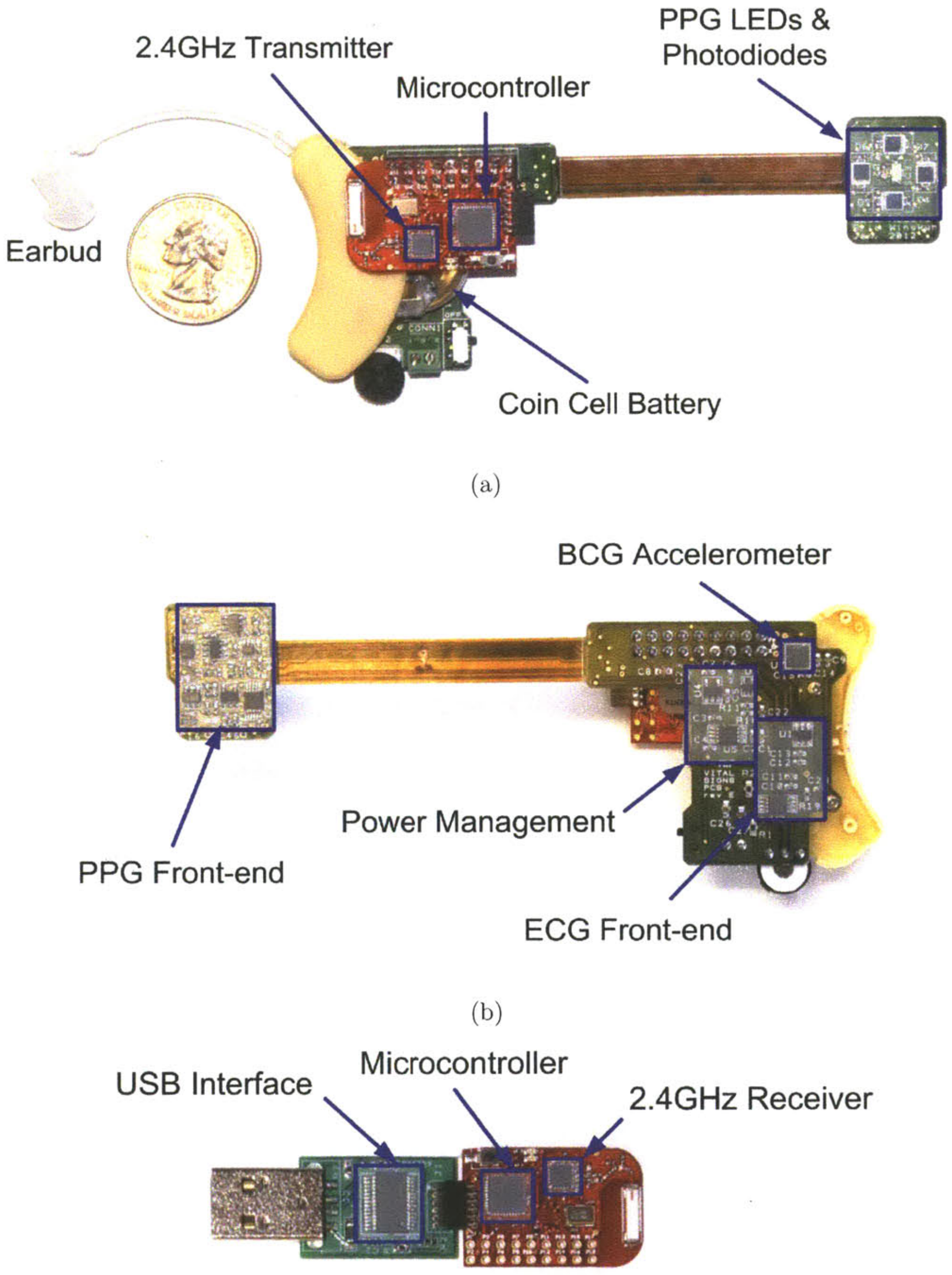

(a)

(b)

(c)

Figure 5-2: a) The wearable heart monitor used in the clinical test, b) the device backside with the case removed, and c) the computer interface.

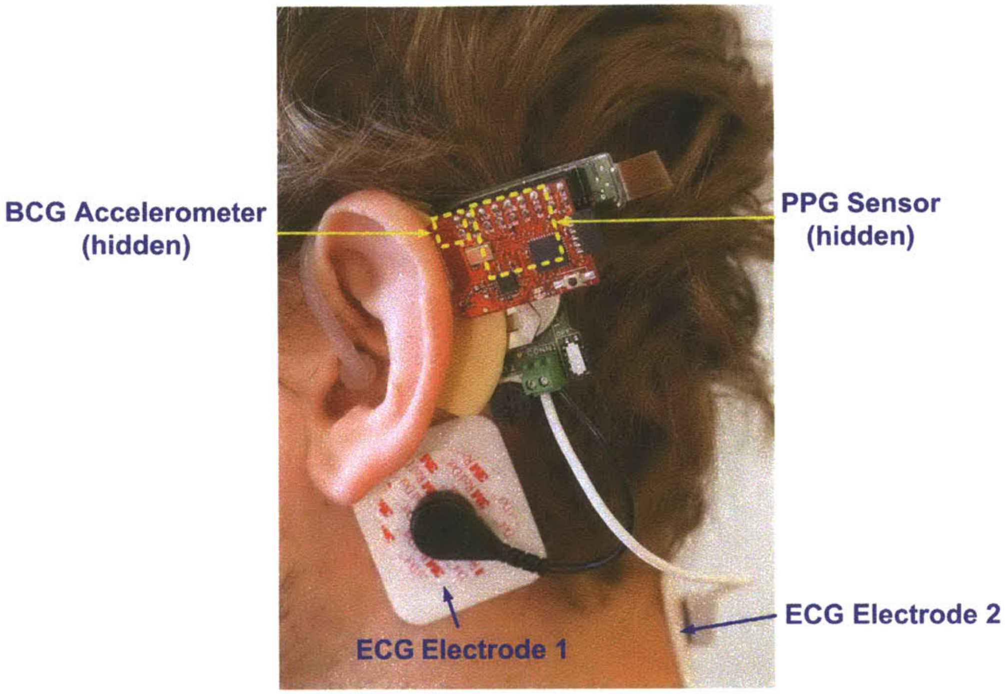

Figure 5-3: The clinical prototype being worn at the ear.

5.1.2 The Microcontroller Firmware

The MSP430 microcontroller firmware on the wearable heart monitor serves three functions: the initialization of all circuits, the polling of sensor data, and the transmission of packetized data to the radio. The MSP430 firmware on the USB receiver unpacketizes the received data and sends it to the USB IC, which in turn sends the data to the computer. The firmware is written in C in Code Composer Studio v4 and can be represented by the flowcharts in Figure 5-4.

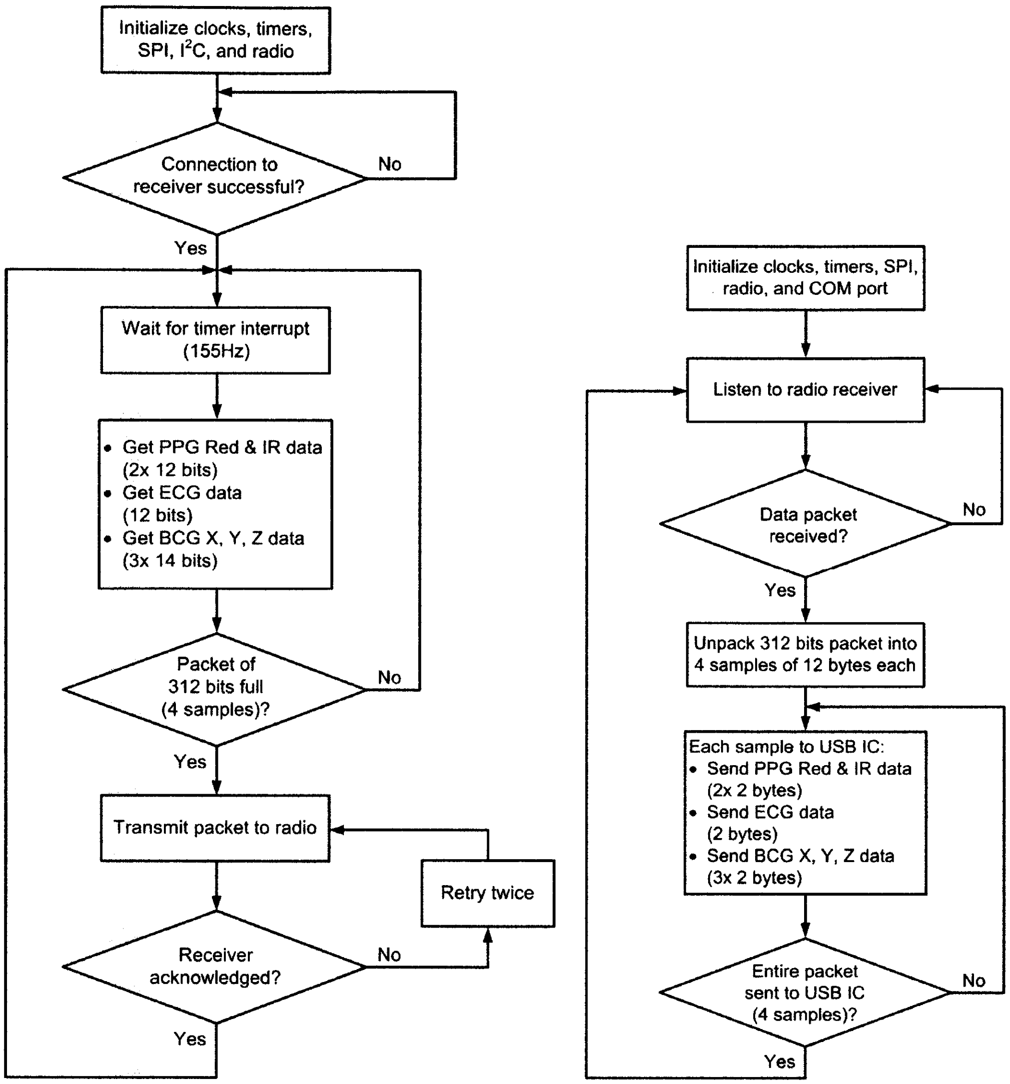

(a) (b)

Figure 5-4: Firmware flowcharts of a) the wearable heart monitor and b) the computer receiver.

5.1.3 The Computer Software

The MATLAB script on the computer reads the received data from the virtual COM port, records the data into memory, and plots the data with real time filtering. Figure 5-5 shows a flowchart of the MATLAB script.

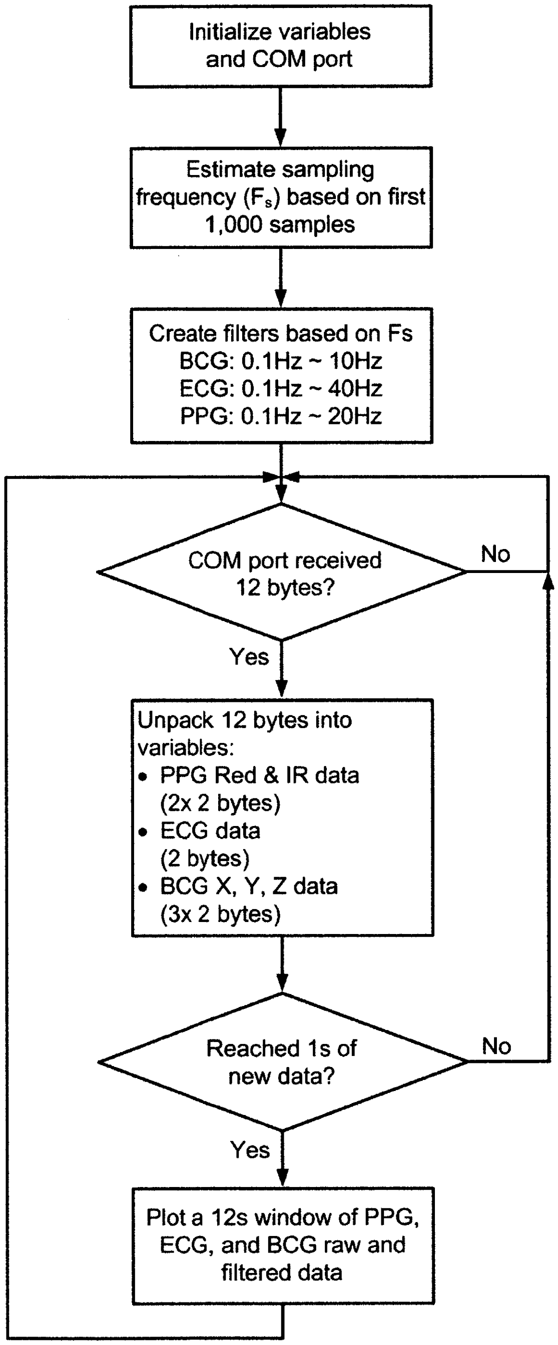

Figure 5-5: The MATLAB script flowchart.

Figure 5-6 shows a screenshot of the real time plots displayed by MATLAB. Plots of red PPG, infrared PPG, filtered PPG, ECG, filtered ECG, and tri-axial accelerations are displayed simultaneously for immediate feedback during the clinical test.

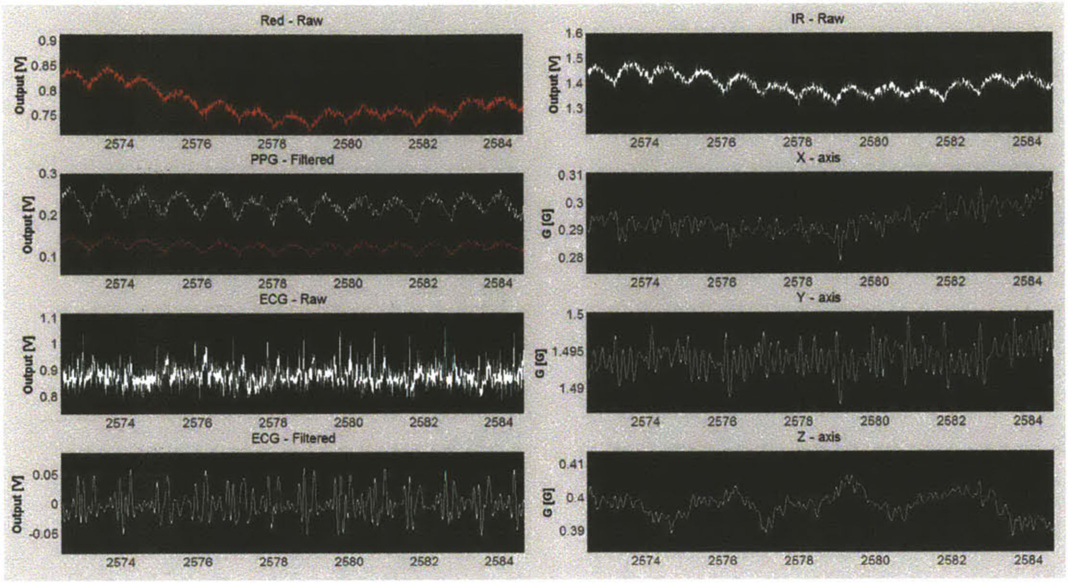

Figure 5-6: A screenshot of the MATLAB real time plotter.

5.2 The Clinical Test Design

The clinical test's goal is to alter the subject's PEP and heart rate through non-invasive hemodynamic maneuvers. The first maneuver is the head-up tilt maneuver, where the subject lies facing up on a motorized tilt table that is tilted between horizontal and 75° vertical. The second maneuver is the Valsalva maneuver, which is a breath-hold exercise where the subject tries to forcibly exhale against a closed airway. From these maneuvers, the signals measured from the device are compared against reference measurements from commercially available equipment.

The test begins with consenting the subject and then completing a health questionnaire to ensure that the subject has no previous cardiovascular conditions. Then, reference measurement equipment is connected to the subject. The equipment is shown in Figure 5-7 and includes the Criticare 504-US chest ECG and finger pulse oximeter, the Finapres Portapres for continuous blood pressure, and Sonosite BioZ Dx impedance cardiography (ICG) machine for continuous PEP and SV. The ECG, PPG, and Portapres data are recorded on an Agilent DSO6104A oscilloscope sampling at $500Hz$ in high resolution acquisition mode where the oscilloscope internally oversamples to achieve greater resolution. The ICG data is internally recorded on the BioZ device.

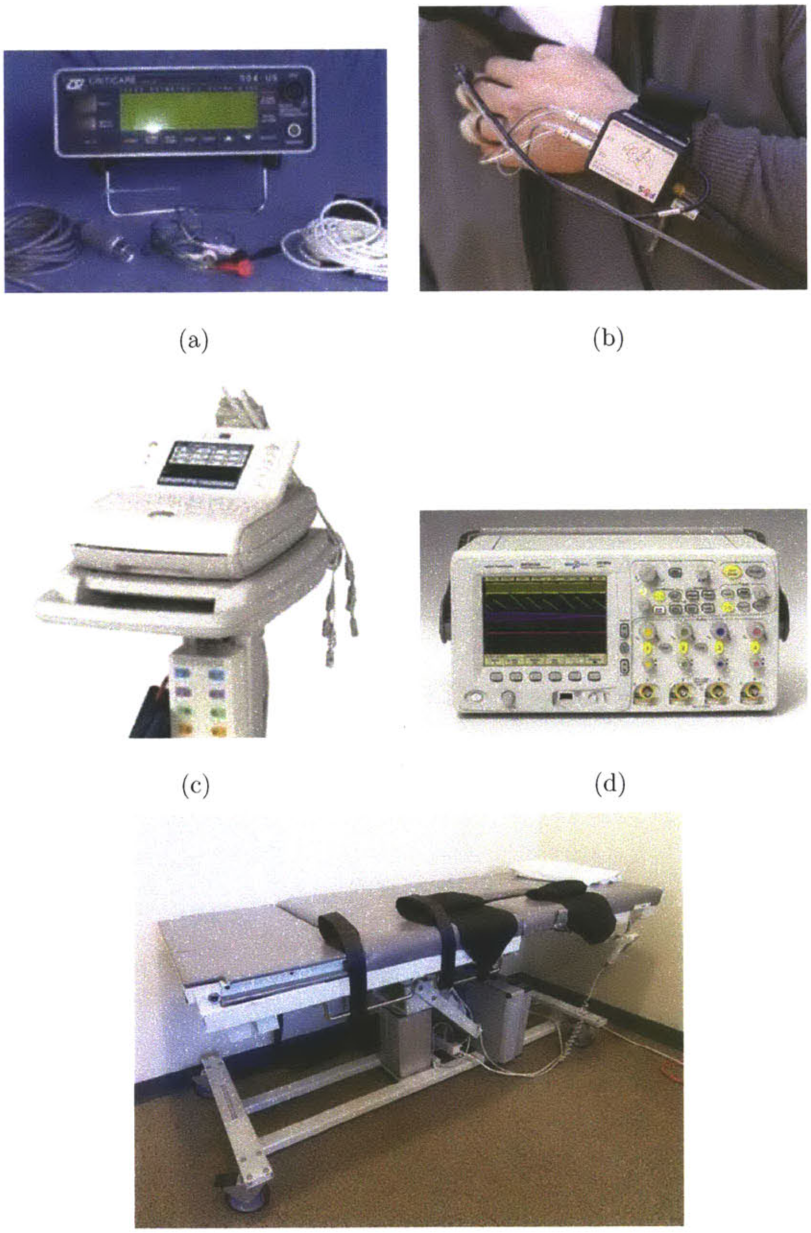

(a) (b)

(c) (d)

(e)

Figure 5-7: The measurement equipment: a) the Criticare 504-US (with transducers), b) the Finapres Portapres, c) the Sonosite BioZ Dx ICG, d) the Agilent DSO6104A, and e) the motorized tilt table.

The Criticare unit measures the chest ECG in a modified Lead II configuration with one electrode placed on the left chest (left mid-clavicle and sixth intercostal), and the second electrode placed on the right chest (right mid-clavicle and first intercostal). The ground ECG electrode is placed at the right mid-clavicle and sixth intercostal. The Criticare unit also measures transmission PPG on the left index finger. The Portapres unit obtains continuous blood pressure through peripheral pressure detected at the left middle or ring finger using the volume clamp method [63]. The ICG machine obtains PEP by detecting the delay between the ECG's Q-wave and the ICG's B-wave (Section 4.1). The ICG machine also calculates SV based on SV's dependence on $PEP/LVET$ as described in Section 4.1. Two ICG electrodes are placed on each side of the torso (midaxillary and sixth intercostal), and two ICG electrodes are placed on each side of the neck along the midaxillary. Lastly, the wearable heart monitor is attached onto the subject with the PPG sensor placed on the mastoid area above Reid's line, one ECG electrode placed below the mastoid, and one ECG electrode placed on the upper middle neck.

The test procedure is summarized below:

1. Subject consent
2. Nurse assessment
3. Administer and review health questionnaire
4. Setup equipment and device on subject
5. Tilt maneuver
    - 5.1 Portapres calibration and cuffed blood pressure (automatic oscillometric monitor at arm) measurement
    - 5.2 Supine (2 min) to tilted (2 min)
    - 5.3 Portapres calibration and cuffed blood pressure measurement
    - 5.4 Tilted (2 min) to supine (2 min)
    - 5.5 Portapres calibration and cuffed blood pressure measurement
    - 5.6 Supine (2 min) to tilted (2 min)
    - 5.7 Portapres calibration and cuffed blood pressure measurement
    - 5.8 Tilted (2 min) to supine (2 min)

6. Valsalva maneuver
    6.1 Portapres calibration and cuffed blood pressure measurement
    6.2 Stand at rest (40 sec), Valsalva (20 sec), then stand at rest (40 sec)
    6.3 Portapres calibration and cuffed blood pressure measurement
    6.4 Stand at rest (40 sec), Valsalva (20 sec), then stand at rest (40 sec)
    6.5 Portapres calibration and cuffed blood pressure measurement
    6.6 Stand at rest (40 sec), Valsalva (20 sec), then stand at rest (40 sec)
7. Exit cuffed blood pressure measurement
8. Exit questionnaire

The setup time and the test duration are each approximately one hour. 13 healthy subjects are tested, consisting of 10 males subjects and three female subjects. The subjects varied from 25 to 63 years old, 1.55m to 1.93m in height and 49.9kg to 103kg in mass. The clinical test is conducted at the MIT Catalyst Clinical Research Center (CRC) under IRB approval #1104004449, CRC protocol #615, and grant #UL1 RR025758.

5.3 The Clinical Test Results

5.3.1 Head BCG Measurements

Table 5.1 summarizes the subject parameters and individual head BCG characteristics in the standing posture, where BMI is the Body Mass Index ($BMI \overset{\text{def}}{=} mass(kg)/height(m)^2$), HR is the average heart rate obtained over a $40s$ time window, and RJI is the average RJ interval obtained over the same $40s$ time window. Amplitudes of I, J, and K-waves are extracted from the individual ensemble averages. NSDE is the normalized standard deviation of beat-to-beat waveforms from the ensemble average of 20 beats (Section 2.4.1). SV is measured by the BioZ ICG machine as described in Section 5.2. All BCG signals are bandpass filtered from $1Hz$ to $10Hz$ prior to analysis to remove gravity contribution and higher frequency artifacts. Figure 5-8 shows the 20-beat head BCG ensemble averages from all subjects in the standing posture.

Subject	Age	Height (m)	Mass (kg)	BMI	HR (bpm)	RJI (ms)	I Amp (mG)	J Amp (mG)	K Amp (mG)	NSDE (%)	SV (mL)
H001	27	1.78	67.1	21.2	100	159	-1.5	3.9	-2.0	41	67
H002	27	1.80	74.8	23.1	90	166	-1.6	3.4	-2.6	41	72
H003	28	1.83	81.6	24.4	95	157	-1.4	3.8	-2.6	42	83
H004	31	1.70	70.3	24.3	68	160	-0.6	3.3	-2.8	37	71
H005	26	1.83	72.6	21.7	71	132	-0.2	4.7	-5.8	33	72
H006	40	1.93	103	27.7	70	153	-4.3	6.0	-5.6	35	122
H007	49	1.78	78.0	24.6	65	159	-3.3	5.4	-2.9	24	102
H008	53	1.75	85.3	27.9	73	187	-2.4	3.0	-1.7	47	82
H009	60	1.83	78.0	23.3	60	184	-1.4	4.5	-3.5	34	102
H010	33	1.55	49.9	20.8	67	169	-0.8	2.6	-1.7	29	60
H011	25	1.70	66.7	23.1	73	188	-2.4	2.7	-0.9	45	56
H012	54	1.83	83.9	25.1	76	143	-0.3	3.6	-2.2	43	76
H013	63	1.65	61.7	22.7	78	201	-0.5	3.1	-1.3	48	67
Mean	39.7	1.77	74.8	23.8	76	166	-1.6	3.8	-2.7	38	79
Stdev	14.2	0.097	12.9	2.2	12	20	1.2	1.0	1.5	7.1	19

Table 5.1: A summary of subject parameters and head BCG characteristics in the standing posture.

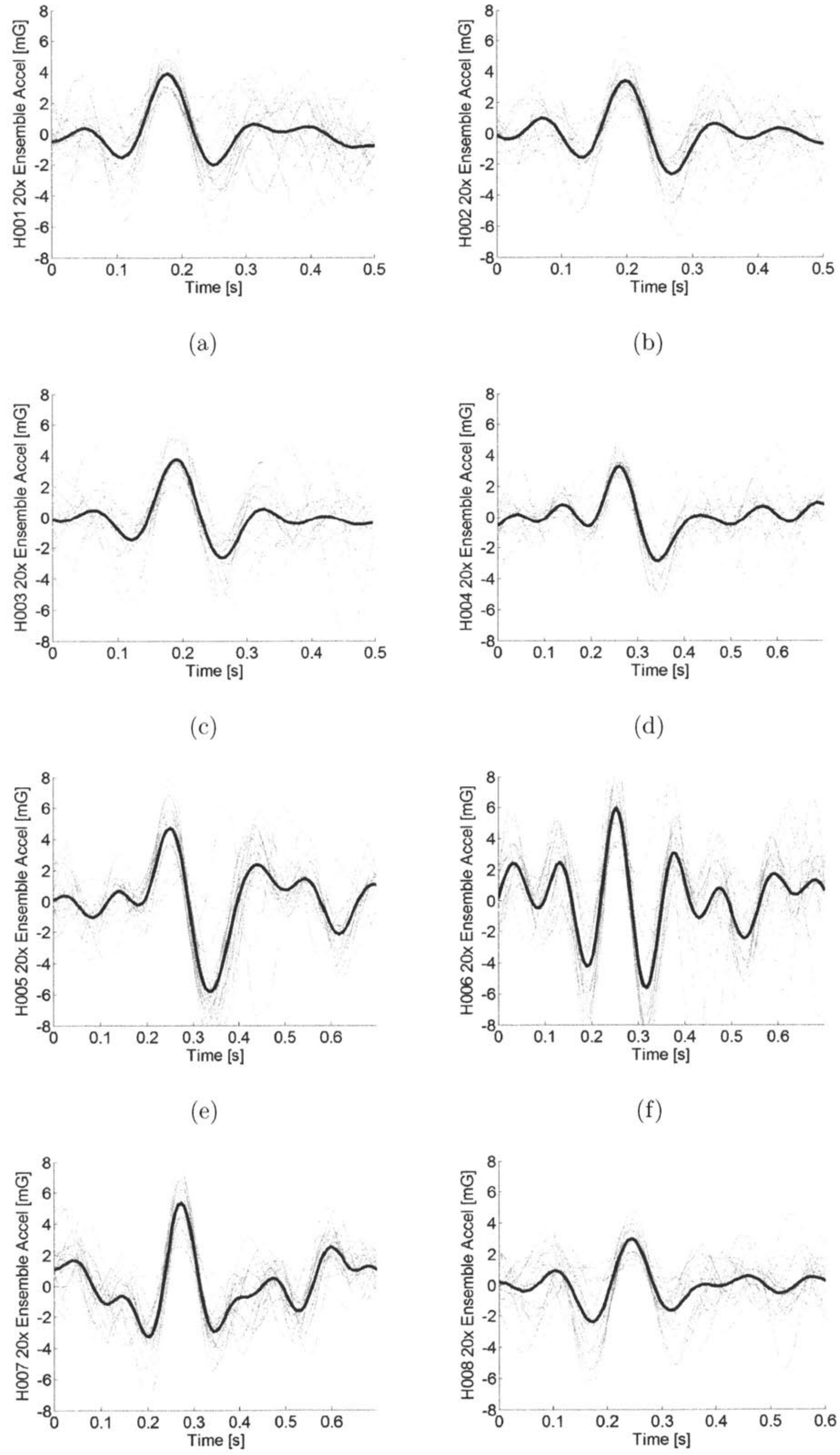
H001 20x Ensemble Accel [mG]
H002 20x Ensemble Accel [mG]
H003 20x Ensemble Accel [mG]
H004 20x Ensemble Accel [mG]
H005 20x Ensemble Accel [mG]
H006 20x Ensemble Accel [mG]
H007 20x Ensemble Accel [mG]
H008 20x Ensemble Accel [mG]
Time [s]
8
6
4
2
0
-2
-4
-6
-8
0
0.1
0.2
0.3
0.4
0.5
0.6

(a) (b)

(c) (d)

(e) (f)

(g) (h)

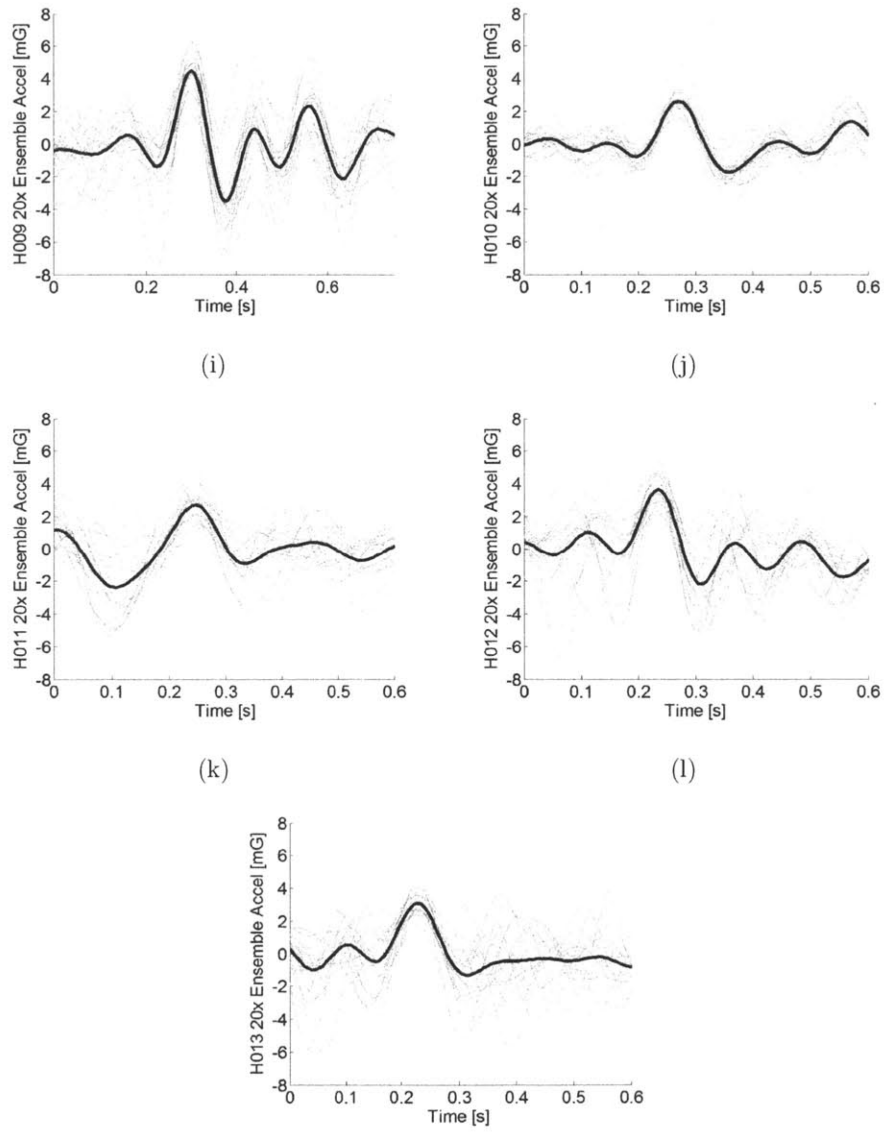

(i) (j)

(k) (l)

(m)

Figure 5-8: 20-beat head BCG ensemble averages in the standing posture from a) H001 to m) H013. The gray traces indicate the underlying individual BCG waveforms.

Several observations can be made from Table 5.1 and Figure 5-8. While there are significant variations in the H, L, M, and N-waves, all subjects possess an IJK wave complex in the ensemble BCG, with an average IJ amplitude of $5.4mG$ and an average JK amplitude of $-6.5mG$. The average NSDE is 38%, which is equivalent to meaning that at any point in time, an average subject's BCG can fluctuate with

$\overline{NSDE} \times \overline{JAmp} = 38\% \times 3.8mG = 1.44mG$ of standard deviation from the ensemble average.

Figure 5-9 plots measured heart rate and SV versus the RJ interval. As expected, no correlation is observed because there is no direct physiological relationship. In fact, the RJ interval does not show correlation to any of the other parameters in Table 5.1.

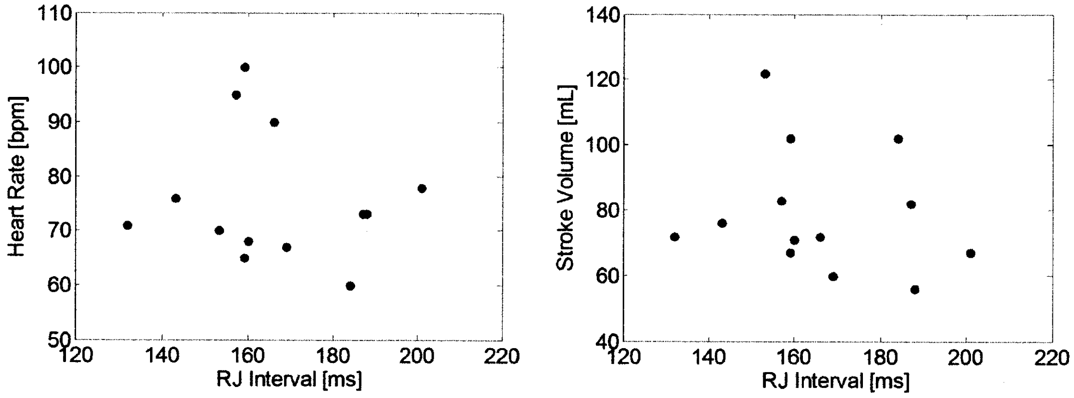

(a)

(b)

Figure 5-9: a) Heart rate versus the RJ interval and b) stroke volume versus the RJ interval.

5.3.2 Heart Rate Measurements

To demonstrate the ability to extract heart rate from the head BCG, Figure 5-10 shows simultaneously extracted heart rates from the ECG and the head BCG from 27,900 heartbeats from 13 subjects in postures of standing, sitting, and supine.

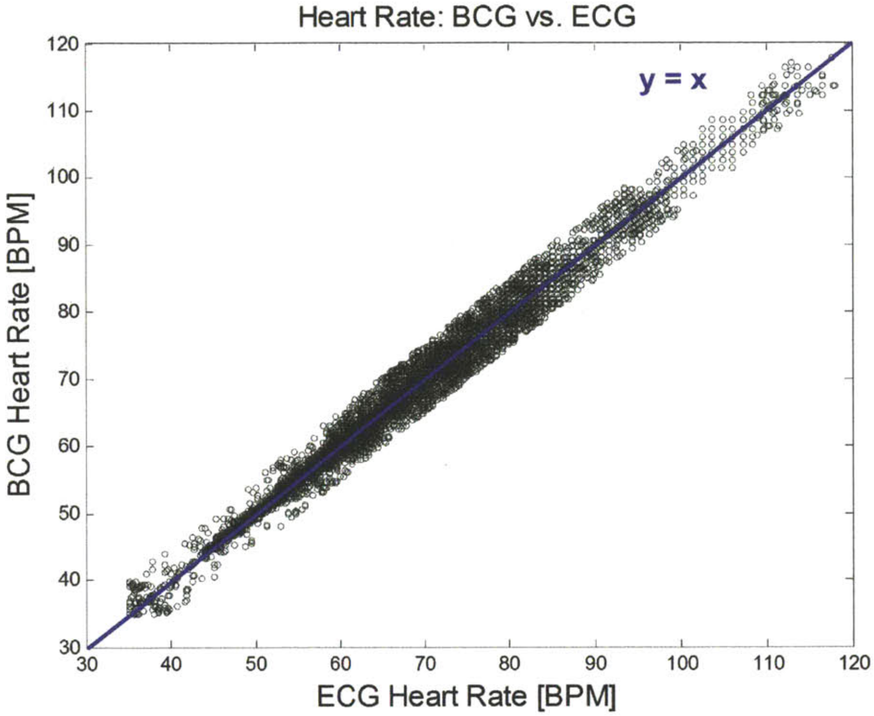

Figure 5-10: A comparison of simultaneously measured heart rates from the ECG and the head BCG.

Table 5.2: Mean absolute error of heart rate between the ECG and the head BCG.

Posture	**Standing**	**Sitting**	**Supine**
Mean absolute HR error [bpm]	0.72	1.27	0.84

With an overall mean absolute error of 0.76 beats per minute and a standard deviation of error of 1.27 beats per minute, it is shown that the head BCG can be used to accurately monitor heart rate in states of rest without the use of electrodes.

5.3.3 Stroke Volume Measurements

Figure 5-11 plots SV (measured by the BioZ ICG machine) versus I, J, and K-wave amplitudes.

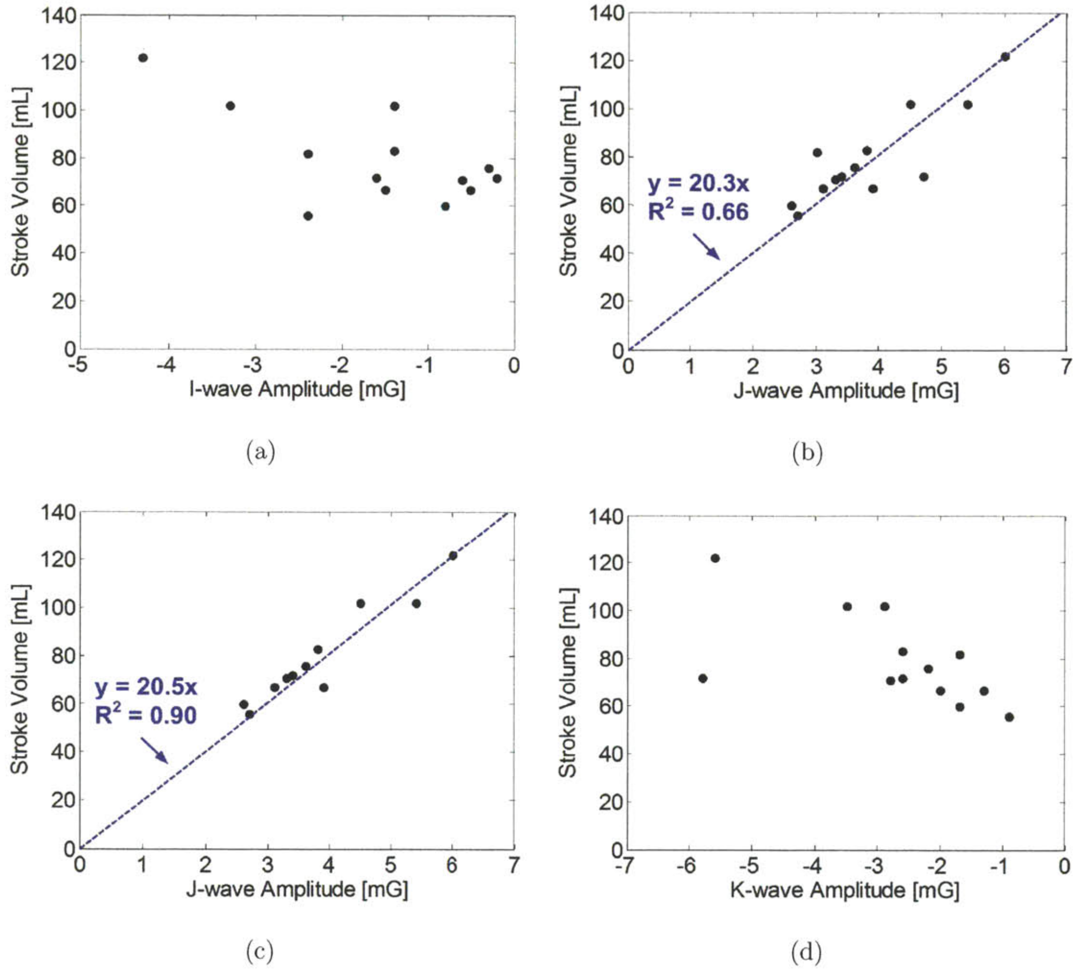

(a) (b) (c) (d)

Figure 5-11: a) I-wave amplitude versus stroke volume, b) J-wave amplitude versus stroke volume, c) J-wave amplitude (with H005 and H008 removed) versus stroke volume, and d) K-wave amplitude versus stroke volume.

J-wave shows the highest correlation with SV. This correlation exists because the BCG recoil is directly related to the mass (or volume) of the pumped blood. Figure 5-11(b) shows a linear fit to the origin with $R^2 = 0.66$. However, if outlier subjects H005 (had chest surgery to correct for pectus excavatum) and H008 (BMI is 1.9 standard deviations higher than the average BMI of tested subjects) are removed in Figure 5-11(c), the R^2 value improves to 0.90 for the remaining 11 subjects. An interesting observation is that the ratio of SV to J-wave amplitude is relatively constant across the test subjects. However, a larger scale study needs to be performed to make a conclusion about the general population.

The immediate value of the observed relationship between J-wave amplitude and SV is the ability to continuously trend a subject's SV and cardiac output (CO). This is demonstrated in Figure 5-12 where a subject performs a brief weight lifting exercise. Here, SV is estimated by multiplying the ensemble J-wave amplitude with $20.3 mL/mG$ (the slope from Figure 5-11(b)), and CO is estimated by multiplying the heart rate by the estimated SV. As expected, the estimated SV and CO are heightened due to exercise and then slowly decrease to the resting baseline. It should be noted that during exercise, SV and CO cannot be estimated because the J-waves are overwhelmed by motion artifacts.

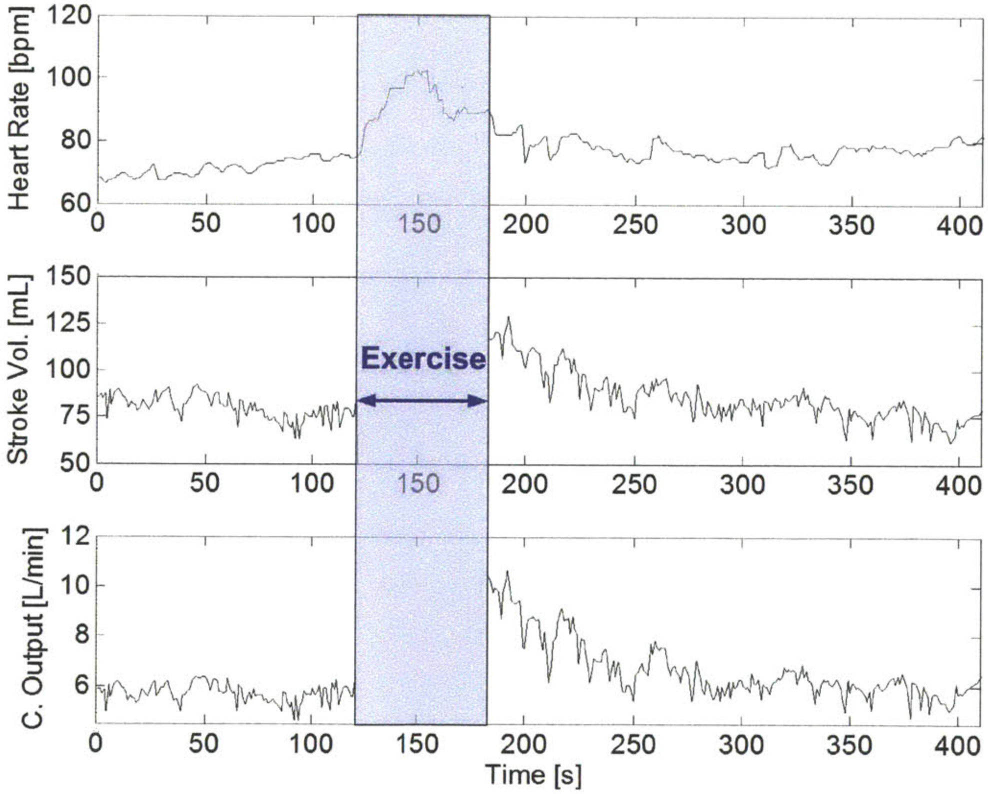

Figure 5-12: Heart rate, estimated stroke volume, and estimated cardiac output before and after exercise for one subject.

5.3.4 RJ Interval and Pre-ejection Period Measurements

The RJ interval's significance lies in its correlation to the heart's PEP. For the study, both head-up tilt and Valsalva maneuvers are designed to induce a temporary increase in PEP in the subjects. The RJ interval is extracted by cross-correlating (Section 4.1.1) the wearable heart monitor's ECG and BCG, while the reference PEP is measured using the ICG machine.

Figure 5-13 shows a representative example of measured RJ intervals and PEP from a subject who performs a Valsalva maneuver from 43s to 63s.

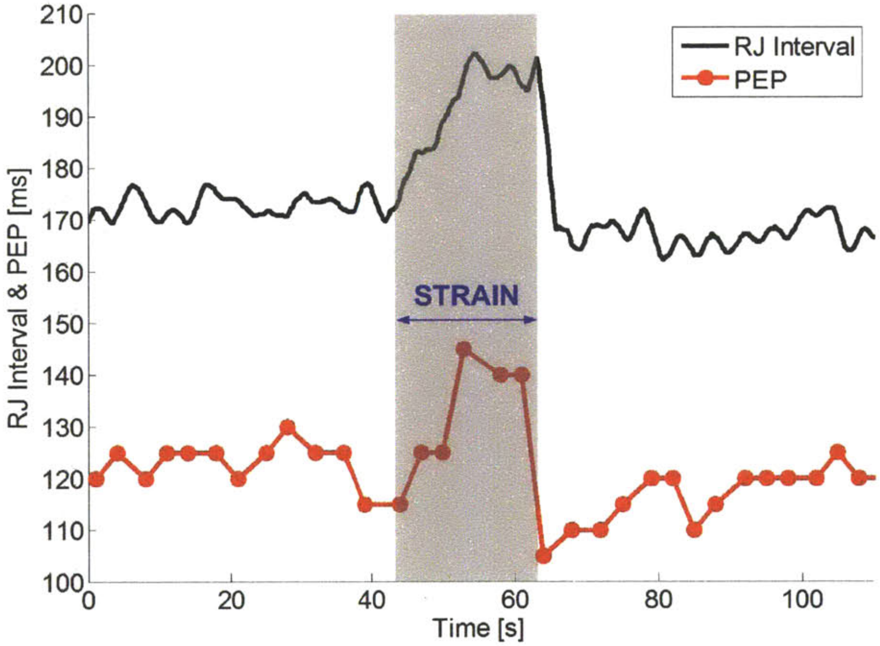

Figure 5-13: Simultaneously measured RJ intervals and PEP during a Valsalva maneuver.

During a Valsalva's intra-thoracic strain, venous return and ventricular filling volume are reduced. The smaller filling volume reduces cardiomyocyte stretching, which leads to a weaker contraction and hence a prolonged PEP [47] [64]. The PEP's increase of $30ms$ corresponds to an equal increase in the RJ interval during the strain. The results in Figure 5-13 are consistent with the RJ interval trends during Valsalva and with the PEP correlation documented in [45] and [46].

In the head-up tilt maneuver, the subject is tilted between 0° (supine) and 75° (tilted). A representative example of simultaneously measured RJ intervals and PEP is shown in Figure 5-14.

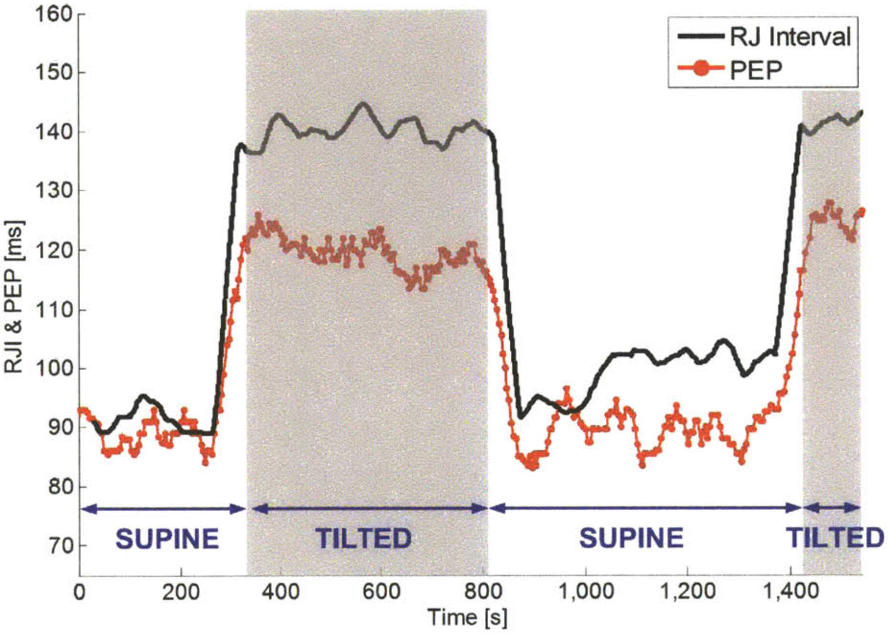

Figure 5-14: Simultaneously measured RJ intervals and PEP on a subject that is tilted twice.

From Figure 5-14, we see that PEP increases when the body is tilted. By the same principle of reduced cardiomyocyte stretching during Valsalva, the increase in PEP is caused by the reduction of ventricular filling volume, this time due to venous pooling at the lower extremities [47] [64]. Similarly, the RJ interval also increases when the body is tilted.

In both maneuvers during the clinical test, it is observed that the RJ interval is always longer than PEP by an offset duration that is subject dependent. This is because the end of PEP is marked by the opening of the aortic valve, while the J-wave occurs when the blood is accelerating after exiting the heart. This offset is affected by variables such as body height and blood pressure, thus making it subject dependent. Furthermore, PEP begins at the ECG's Q-wave, while the RJ interval begins at the ECG's R-wave. The QR interval marks a delay in the electrical propagation of cellular depolarization. This delay is another reason why the offset between the RJ interval and PEP is subject dependent. The relationship between PEP and the RJ interval is illustrated in Figure 5-15.

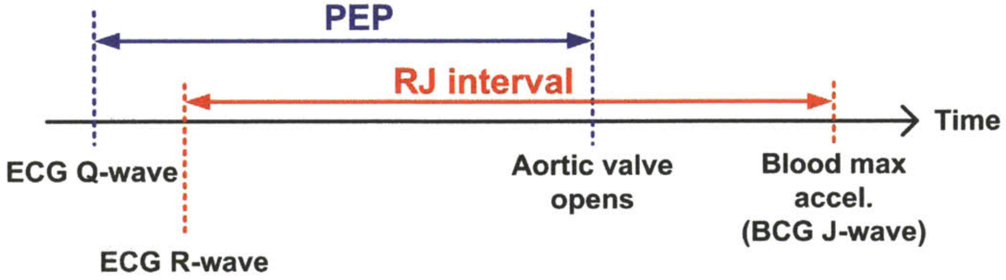

Figure 5-15: The sequence of events from the ECG's Q-wave to the BCG's J-wave illustrating the offset between PEP and the RJ interval.

Figure 5-16 plots the beat-to-beat RJ interval versus PEP after removing the subject-dependent RJ interval-PEP offsets. The data consists of 28 tilt maneuvers from seven subjects with 2,258 beats total. The remaining six subjects had faulty PEP measurements as the BioZ ICG machine was unable to locate B-waves on certain subjects.

As seen in Figure 5-16, the RJ interval exhibits a near one-to-one linear dependence on PEP, with a slope of 0.96 and an R^2 value of 0.96. Subject 7 contains some spread of data which is caused by measurements taken during the tilting of the table. A Bland-Altman representation of the data is shown in Figure 5-17, where the standard deviation in differences between the beat-to-beat RJ interval and PEP is $9.6ms$ for seven subjects.

This clinical data verifies that the RJ interval measured at the head can be used to estimate PEP after removing subject-dependent timing offsets. This supports the hypotheses in Chapter 4 and demonstrates that a portable and wearable method of PEP measurement is possible using the head BCG and the head ECG.

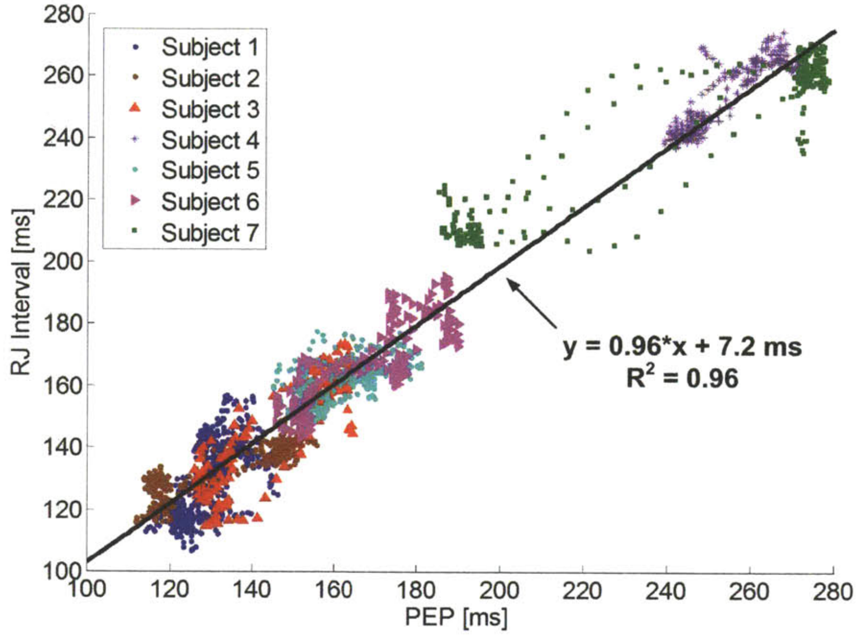

Figure 5-16: The beat-to-beat RJ interval and PEP among seven subjects during 28 tilt maneuvers.

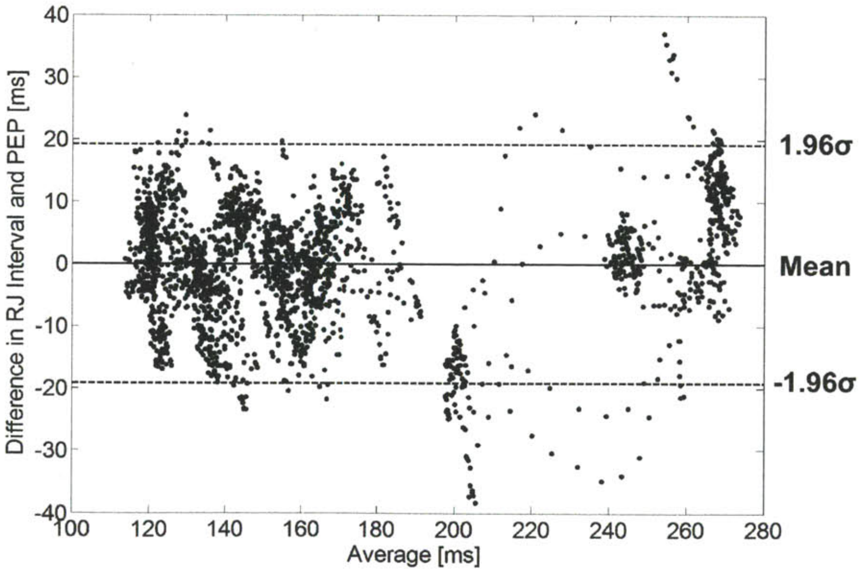

Figure 5-17: The Bland-Altman representation of the beat-to-beat RJ interval and PEP from the same data set used in Figure 5-16.

Chapter 6

A Nanowatt ECG ASIC for Motion-tolerant Heartbeat Detection and R-wave Timing Extraction

This chapter presents the design and measurement results of a nanowatt electrocardiogram (ECG) application-specific integrated circuit (ASIC) that performs heartbeat detection. The ECG ASIC is capable of extracting R-wave timings, which can be used by the wearable heart monitor to determine heart intervals such as the RR interval, the RJ interval, and pulse arrival time (PAT). Based on the knowledge of ECG morphology at the chest and the head, a new circuit topology is implemented to significantly reduce power consumption and circuit constraints. Each circuit block is discussed in detail. Measured IC results from both electrical and human tests are presented. Finally, a method to extract R-wave timings from the ASIC output is validated using clinical data.

6.1 The Standard Topology for ECG Heartbeat Detection

Traditionally, the topology for an ECG heartbeat detection circuit consists of a low noise instrumentation amplifier (IA), an anti-alias filter, an analog-to-digital converter (ADC), and a digital signal processor (DSP) or microcontroller [65] [66] [67]. This topology is employed in the clinical wearable heart monitor prototype and is shown in Figure 6-1.

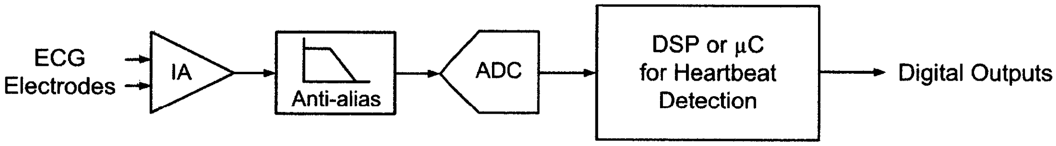

Figure 6-1: The standard topology of an ECG heartbeat detection circuit.

In this topology, the IA amplifies the differential ECG signal with low noise op amps to minimize the addition of circuit noise. The gain of the IA is set so that the amplified output is not saturated. After the anti-alias filter, the ADC uniformly quantizes the ECG signal, treating small features such as the ECG's P wave and large features such as the ECG's R wave with equal resolution. The ADC is usually implemented with a medium resolution successive approximation (SAR) architecture to minimize power consumption. Finally, to detect heartbeats, the digitized ECG is processed by a microprocessor using a peak detection algorithm to detect R-waves. Depending on the computational power available, such an algorithm ranges from simple thresholding to wavelet transforms.

The traditional topology is necessary for clinical ECG measurements, where multilead ECG signals are acquired with high quality in order to diagnose complex arrhythmias. These recordings are usually quantized with at least 12 bits to preserve P wave details [68]. The American Heart Association recommends a sampling frequency of at least $150Hz$ to capture all features, while stating that a bandwidth of $1Hz$ to $30Hz$ generally produces a stable ECG without artifacts [69].

6.2 A New Topology for ECG Heartbeat Detection

For applications such as the wearable heart monitor, only the R-wave timing is relevant. To take advantage of this fact, a new topology is designed to remove the need for ADC and signal processing to significantly decrease the circuit's power and area. At the same time, the new topology can robustly extract heartbeat timings in the presence of motion artifacts and degraded signal quality.

The proposed topology is based on the fact that heartbeat detection relies on the ECG's QRS complex, which has a higher frequency content and a greater magnitude than adjacent ECG features. This circuit topology is shown in Figure 6-2 along with an ECG illustration.

In Figure 6-2, the differential ECG signal is first amplified by a low noise programmable gain amplifier (PGA). The PGA's output splits into two paths. The first path goes through the "QRS Amp," which has a bandwidth that preserves the QRS complex. The second path goes through the "Baseline Amp," which has an equal gain but a lower bandwidth to preserve only the low frequency baseline drift caused by motion artifacts. Then, a positive inline DC offset V_{DC} is added to $V_{Baseline}$ to create an adaptive threshold $V_{Baseline+DC}$. One can observe that a QRS complex (or heartbeat) occurs whenever $V_{QRS} > V_{Baseline+DC}$. This comparison is performed by a comparator, which consequently pulses a high D_{OUT} when a heartbeat is detected.

To correctly set V_{DC}, it is incremented until the period between D_{OUT} pulses is regular and is in the range of human beat-to-beat interval. As shown in Figure 6-2, there is a wide range of valid V_{DC} values since V_{DC} can be set at any level between the R-wave and the next highest feature (usually the T-wave). V_{DC} is set by an external microcontroller at the beginning of measurement and the one-time calibration takes less than one minute. The microcontroller is powered off afterwards. If the subject's R-waves are consistently irregular, then the calibration would be unable to complete, which by definition can be used to imply the presence of irregular beats.

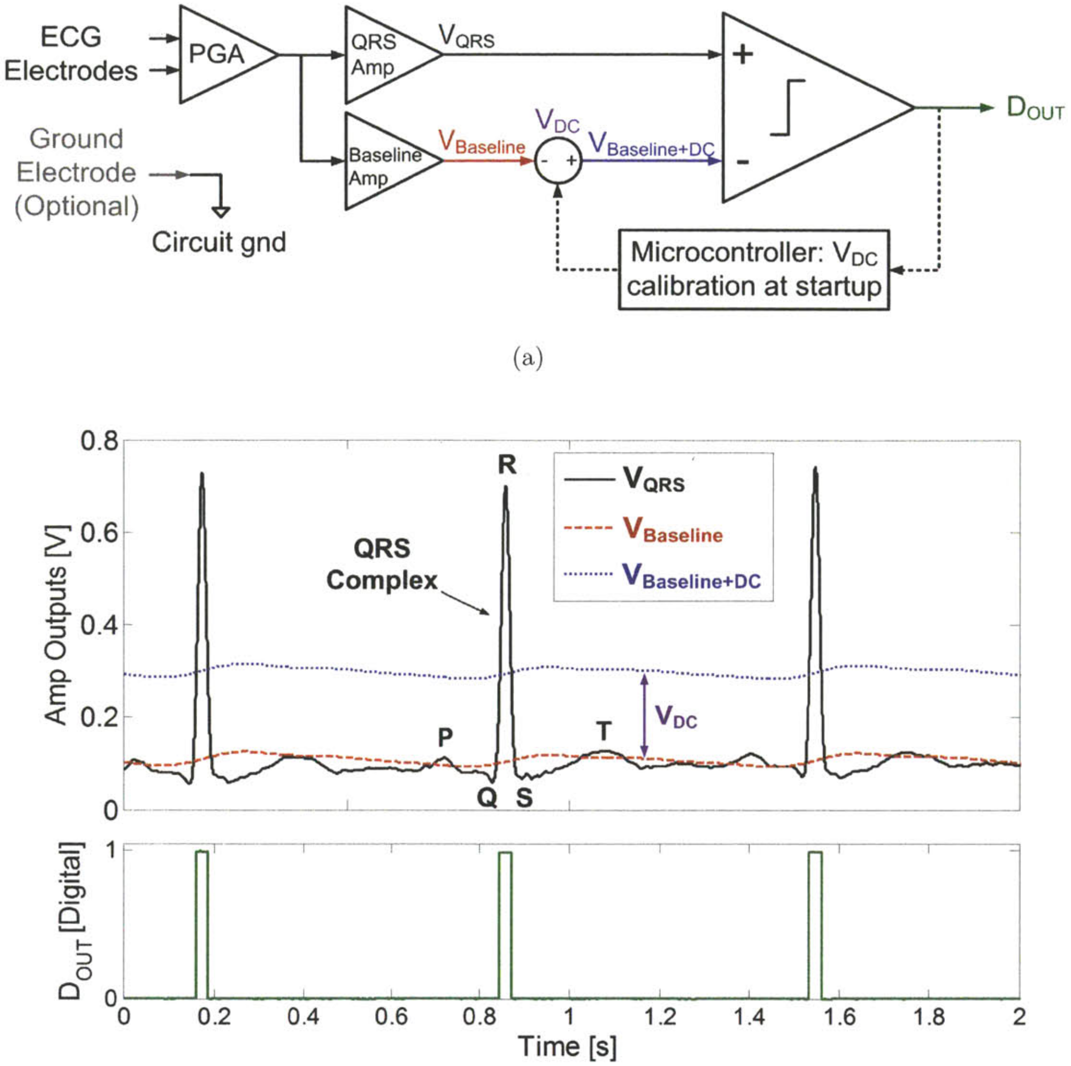

(a)

(b)

Figure 6-2: a) The new topology for ECG heartbeat detection with voltage nodes labeled, and b) color-matched time waveforms illustrating the QRS complex, baseline, baseline with V_{DC} offset, and digital output.

The above method of setting V_{DC} can be accelerated if the R-wave voltage is known, in which case V_{DC} can be initially set at the midpoint between baseline and R-wave voltage. This skips the region of V_{DC} where $V_{Baseline+DC}$ is close to $V_{Baseline}$ and thus D_{OUT} is noisy and invalid. However, to process the peak R-wave voltage information in the V_{DC} algorithm, an ADC is needed. The power consumption of this ADC is unimportant because it can be turned off after calibration. Also, this ADC can be low resolution and requires insignificant die area. Such an ADC is not implemented in the current design because it is proposed after fabrication, but it is a useful addition for a future iteration.

There are several advantages to this topology in terms of circuit design. First, no signal processor or ADC is required, which significantly reduces the device power and die area. Second, a low voltage supply is possible because a clipped R-wave that exceeds the amplifier's dynamic range still possesses beat information. Third, any comparator offset is automatically compensated due to the V_{DC} calibration. Fourth, amplifier linearity is unimportant because the signal path is highly nonlinear. In terms of practical usage, this topology is tolerant to motion artifacts because the signal is compared against its own baseline. Furthermore, no predefined subject-dependent parameters are needed.

6.3 The ECG ASIC Circuit Design

The ASIC is designed in the TSMC $0.18\mu m$ CMOS technology. $V_{DD} = 0.8V$ is chosen as a compromise between low power and the dependence on threshold voltage variation. This section will describe each of the circuit blocks in Figure 6-3.

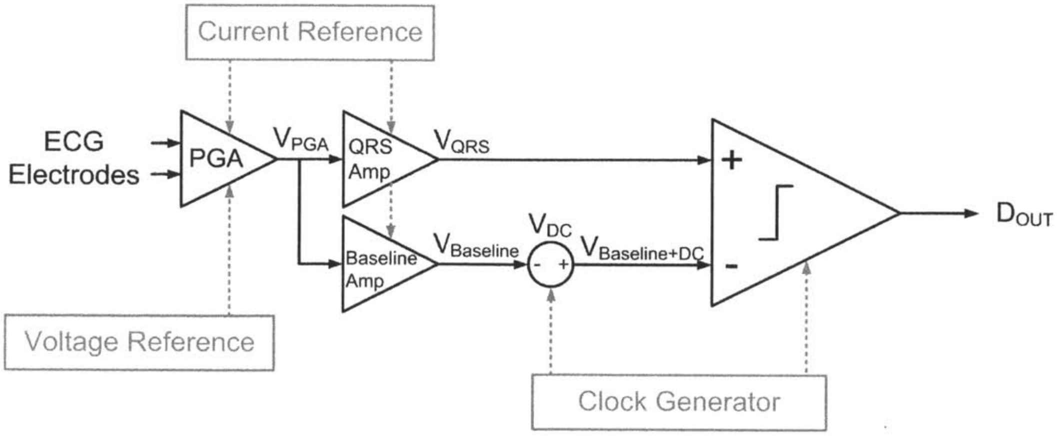

Figure 6-3: The circuit blocks of the ECG ASIC.

6.3.1 The Programmable Gain Amplifier Design

The PGA's function is to amplify the ECG directly from the electrodes with minimal circuit noise and power while having a range of gain to adapt to ECG's at various locations on the body. Figure 6-4 shows the schematic of the PGA, which consists of an op amp in the difference configuration.

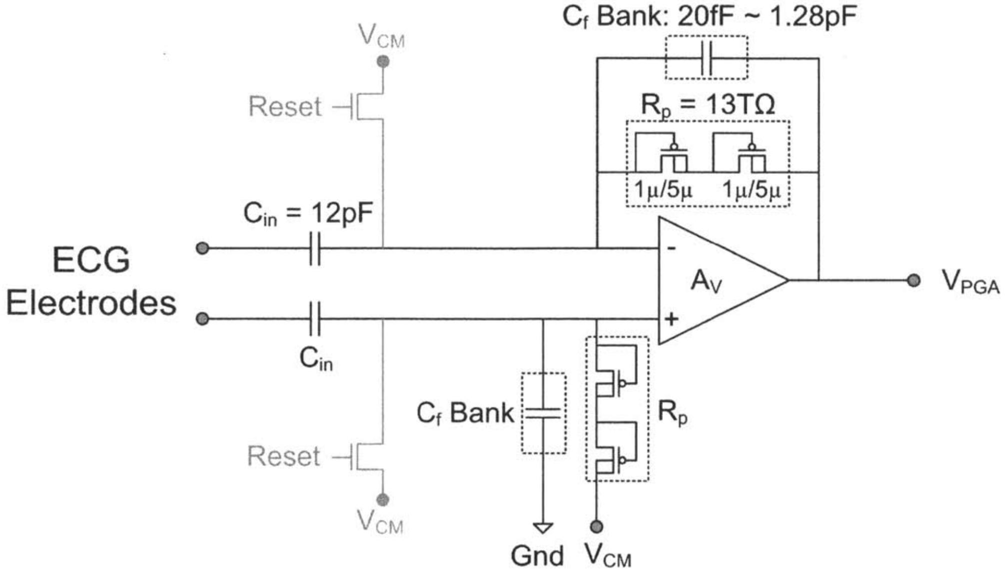

Figure 6-4: The PGA schematic.

Sensing a biopotential such as the ECG creates several circuit requirements. First, because the ECG amplitudes vary between different body locations and different subjects by up to two orders of magnitude, an adjustable gain is required. The gain of the PGA is set by C_{in}/C_f, where $C_{in} = 12pF$ and C_f is implemented as a 6-bit binary weighted capacitor bank of $20fF$ to $1.28pF$ to adjust the PGA gain from $19dB$ to $56dB$. The capacitor bank is shown in Figure 6-5.

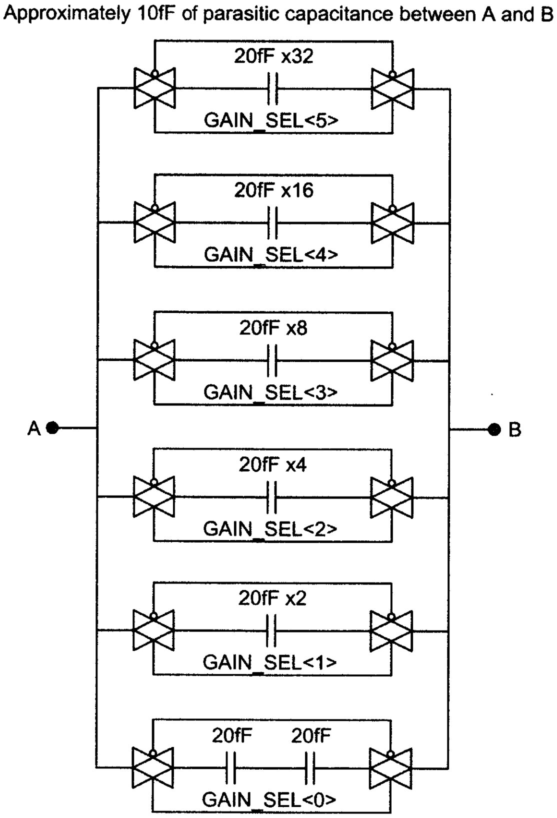

Figure 6-5: The 6-bit binary weighted capacitor bank used for gain adjustment.

Second, the $AgCl$ electrode's half-cell potential generates approximately $200mV$ of near-DC electrode offset voltage (EOV) which will saturate the amplifier if not removed. To filter this EOV, thick-oxide PMOS pseudo-resistors (R_p) are used [70]. The R_p's are diode-connected PMOS transistors when V_{SG} is positive. When V_{SG} is negative, the R_p's are diode-connected source-well-drain PNP bipolar junction transistors. In either case, R_p's incremental resistance is very high when the voltage across the pseudo-resistors is low, as shown in Figure 6-6.

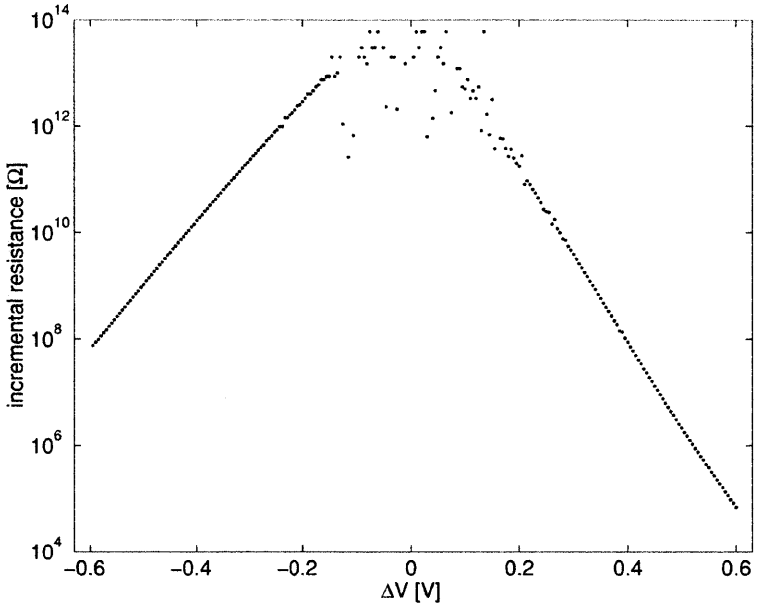

Figure 6-6: Measured incremental resistance versus applied voltage of a single-transistor R_p in $1.5\mu m$ process (Figure from [70]).

In the current design, the R_p's are $13T\Omega$ but only occupy $10\mu m^2$. This makes on-die sub-Hz high pass filters feasible ($f_h = 1/(2\pi R_p C_f) = 0.61Hz$ in the case of $C_f = 20fF$), which effectively filters the EOV. For any PGA gain setting except for the highest gain, C_f would be greater than $20fF$ and a smaller value of R_p (such as caused by process variations) can be tolerated while maintaining a sub-Hz high pass corner frequency.

The third requirement on the PGA is a large input impedance. The ECG voltage V_{in} sensed at the PGA inputs is voltage divided across Z_f and R_p ($Z_f = 0.80T\Omega$ at $20fF$ and $10Hz$), which is in series with the electrode resistance ($R_{elec} \approx 300k\Omega$) and Z_{in} ($Z_{in} = 1.3G\Omega$ at $12pF$ and $10Hz$). This series connection is shown in Figure 6-7.

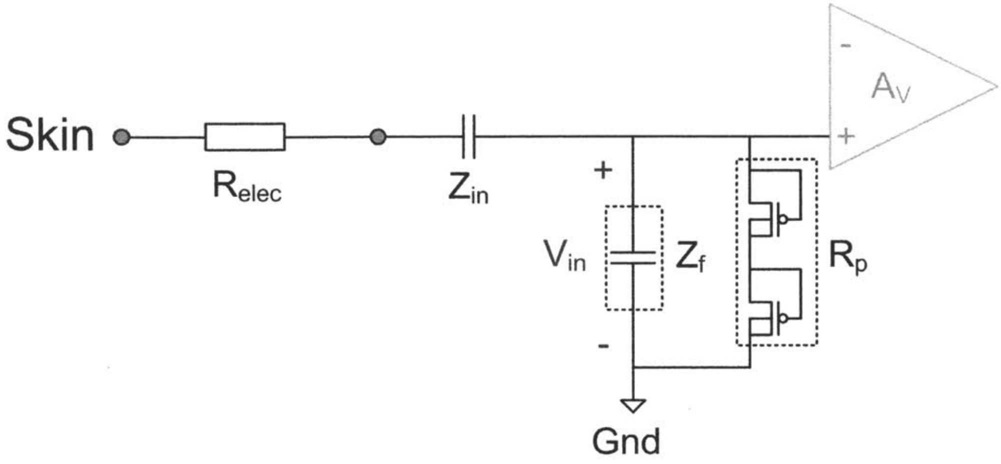

Figure 6-7: The voltage division that occurs at the PGA input.

By having $R_p = 13T\Omega$, the input impedance ($Z_f \| R_p$) is at least two orders of magnitude greater than $Z_{in} + R_{elec}$, resulting in less than 1% of attenuation due to voltage division. Furthermore, because the input impedance is significantly larger than R_{elec}, any differential voltage caused by unequal and varying R_{elec} (such as during motion) is negligible.

It should be noted that the high impedance at the PGA input nodes leads to long start-up settling times. As a solution, reset switches shown in Figure 6-4 are added to the PGA inputs to immediately shunt the input nodes to their final common-mode DC voltage V_{CM}, which is a mid-rail voltage generated by the voltage reference (Section 6.3.5).

The PGA's op amp is a two-stage Miller-compensated op amp. This topology is chosen because of its compatibility with low voltage supply, wide output swing, and self-bias. Because the ECG at remote locations on the body can be as low as $30\mu V_{pp}$, the op amp needs to minimize circuit noise while consuming very low power. At the low frequencies of ECG signals ($1Hz - 25Hz$), amplifier noise is dominated by 1/f noise instead of thermal noise. In addition, the low signal bandwidth allows the op amp to have a correspondingly low bandwidth. This means that the op amp can be in deep subthreshold with low g_m without compromising signal quality.

Chopper modulation at the PGA inputs is a possible method to eliminate 1/f noise. However, chopper switches introduce a current path between the PGA inputs. If there is any input offset voltage, then an offset current will exist that can saturate the PGA through the high resistance feedback R_p. A solution is to use a $G_M - C$ servo-loop to provide a current path, but it consumes additional current and adds complexity [71]. For this reason, chopper modulation is not used.

The PGA op amp schematic is shown in Figure 6-8.

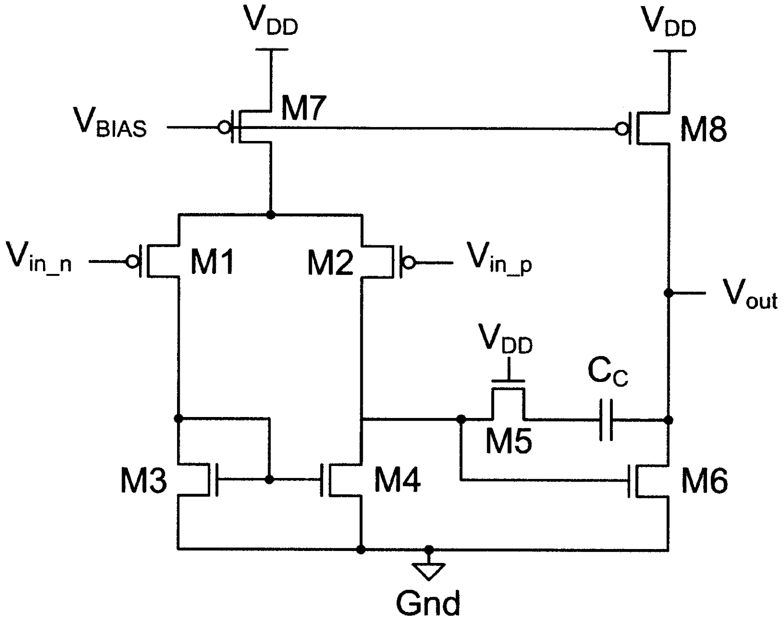

Figure 6-8: The PGA two-stage op amp schematic.

The transistors are sized to minimize 1/f noise. The input-referred 1/f noise spectral density for this op amp in subthreshold is shown in Equation (6.1) [72]:

$$\frac{v_{ifsub}^2}{\Delta f} = \frac{2 \cdot K_1}{W_1 L_1 C_{ox}^2 f} + \frac{2 \cdot K_3}{W_3 L_3 C_{ox}^2 f} \tag{6.1}$$

According to Equation (6.1), the following design choices are made to minimize 1/f noise:

- PMOS input transistors are used because they offer lower noise coefficients than NMOS transistors: $K_1 = K_p < K_n$.

- Increasing W_3 and L_3 will reduce the noise contribution of the mirror transistors. However, signal swing places an upper limit on W_3 and process technology places an upper limit on L_3. A dimension of $100\mu m/20\mu m$ is chosen so that M3 and M4's 1/f noise contributes to 20% of total input noise.

- Increasing W_1 and L_1 will reduce the noise contribution of the input transistors. However, excessive input transistor area will introduce significant parasitic capacitance at the drain of M2. This decreases the frequency of the second pole and lowers the phase margin. A dimension of $864\mu m/1.5\mu m$ is chosen as a compromise between noise and phase margin. L_1 does not need to be as long as L_3 because PMOS transistors generate less 1/f noise: $K_1 = K_p < K_n = K_3$. At this dimension, M1 and M2's 1/f noise contributes to 40% of total input noise. Additionally, by being eight times longer than the minimum length, the gate length of $1.5\mu m$ reduces the input transistors' geometry mismatch.

The transistor dimensions are listed in Table 6.1.

Transistor	**W/L × fingers** $[\mu m/\mu m]$
M1, M2	$9/1.5 \times 96 = 864/1.5$
M3, M4	$12.5/20 \times 8 = 100/20$
M5	2/0.5
M6	6.22/1
M7	$2/1 \times 80 = 160/1$
M8	$2/1 \times 16 = 32/1$

Table 6.1: Transistor dimensions of the PGA op amp.

M5 is used to insert finite nulling resistance to improve stability. M6 is sized to eliminate systematic offset voltage in simulation. M7 and M8 are biased by V_{Bias}, which is produced by the current reference (Section 6.3.5). The compensation capacitor C_C is a $1.9pF$ MIM capacitor which sets the op amp phase margin to be 55° at the minimum gain of $19dB$. Although the PGA is not unity-gain stable, no power-on (step V_{DD} and step input) instability is observed in transient simulation until the phase margin is decreased to be near 0° at the set gain.

Table 6.2 summarizes the simulated results of the PGA at $V_{DD} = 0.8V$:

Parameter	**Simulated Result**
Open loop DC gain	$91dB$
Open loop bandwidth	$2.9Hz$
Unity gain bandwidth	$90kHz$
Closed loop midband gain	$20dB - 56dB$
Closed loop bandwidth at max gain	$0.52Hz - 130Hz$
Phase margin at min. gain	55°
CMRR at 60Hz	$78dB$
PSRR at 60Hz	$53dB$
Input-referred noise, $0.1Hz - 50Hz$	$0.98\mu V_{rms}$
Current consumption	$91nA$

Table 6.2: Simulated results of the PGA op amp.

6.3.2 The QRS and Baseline Amplifier Design

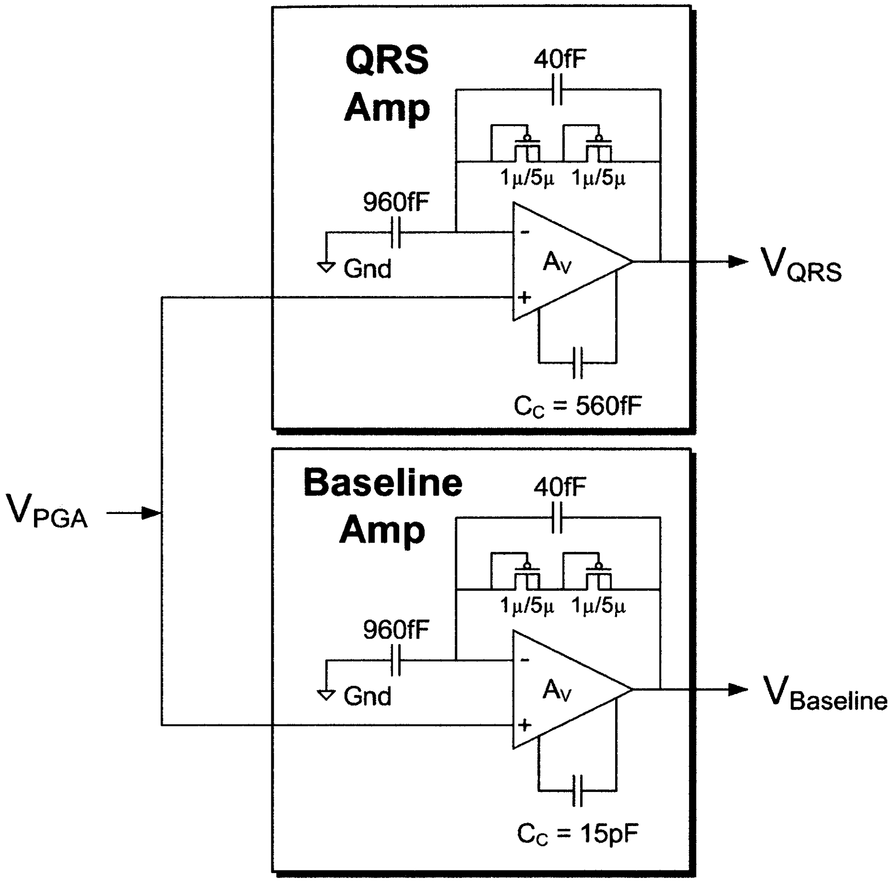

Figure 6-9: The QRS Amp and the Baseline Amp.

The PGA's output is connected to the inputs of the QRS and Baseline Amps. As previously mentioned, the function of the QRS Amp is to amplify the ECG signal with a bandwidth that passes the QRS complex, while the Baseline Amp has the same gain but with a lower bandwidth that only passes the baseline signal.

In Figure 6-9, both amplifiers use identical two-stage Miller-compensated op amps in the non-inverting configuration. The only difference is in the compensation capacitors (C_C). The C_C and a sub-nA bias current create very low corner frequencies while being area-efficient. For the QRS Amp, $C_C = 560fF$ sets the low pass corner frequency at $25Hz$, which passes the QRS complex. For the Baseline Amp, $C_C = 15pF$ sets the low pass corner frequency at $1Hz$, which only passes the baseline drift. Pseudo-resistors are used to bias the inverting node and to create a sub-Hz high pass characteristic, which reduces sub-Hz 1/f noise contributions from the PGA.

Both QRS and Baseline Amps have a fixed gain of $960fF/40fF = 28dB$, thus resulting in an overall gain range of $47dB$ to $84dB$. At this overall gain range and with $V_{DD} = 0.8V$, the full dynamic range can be used to measure ECG signals on various wearable locations on the body where the ECG ranges from $30\mu V_{pp}$ (ear) to $3mV_{pp}$ (chest).

The QRS and Baseline op amp schematic is shown in Figure 6-10, where $C_C = 560fF$ for the QRS Amp, and $C_C = 15pF$ for the Baseline Amp.

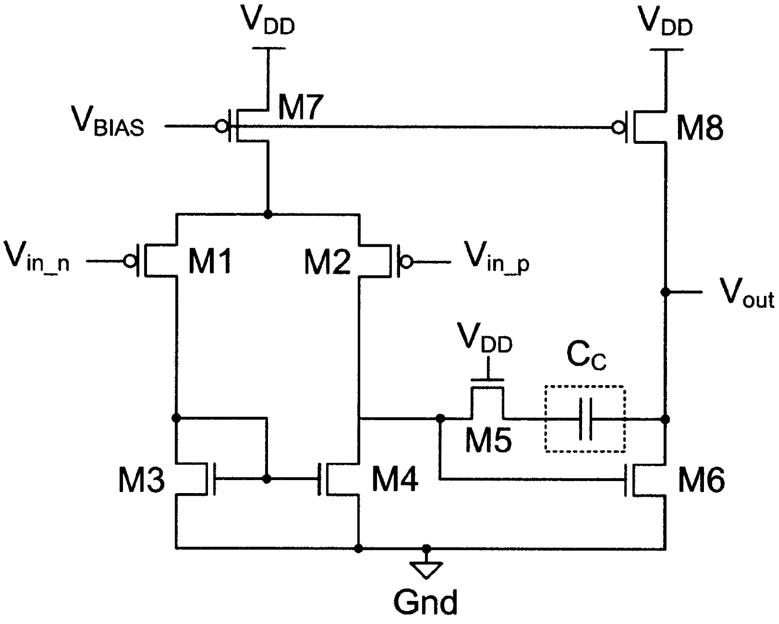

Figure 6-10: The QRS and Baseline two-stage op amp schematic.

The transistors are sized for low power. The dimensions are listed in Table 6.3.

Transistor	**W/L × fingers** $[\mu m/\mu m]$
M1, M2	$5/5 \times 6 = 30/5$
M3, M4	$2.5/20 \times 4 = 10/20$
M5	$2/0.5$
M6	$1.39/1$
M7	$0.5/8 \times 4 = 2/8$
M8	$0.5/8 \times 2 = 1/8$

Table 6.3: Transistor dimensions of the QRS and Baseline op amp.

Table 6.4 summarizes the simulated results of the QRS and Baseline Amps at $V_{DD} = 0.8V$:

Parameter	**Simulated Result**
Open loop DC gain	$85dB$
Open loop bandwidth	$51mHz$
Unity gain bandwidth	$990Hz$
Closed loop midband gain	$28dB$
Closed loop bandwidth, $C_C = 560fF$	$0.18Hz - 51Hz$
Closed loop bandwidth, $C_C = 15pF$	$0.16Hz - 1.9Hz$
Phase margin at gain	85°
Input-referred noise, $0.1Hz - 50Hz$	$8.3\mu V_{rms}$
Current consumption	$560pA$

Table 6.4: Simulated results of the QRS and Baseline op amp.

6.3.3 The V_{DC} Generator Design

The V_{DC} generator's function is to add V_{DC} to $V_{Baseline}$ to produce an adaptive threshold $V_{Baseline+DC}$. The V_{DC} generator schematic is shown in Figure 6-11.

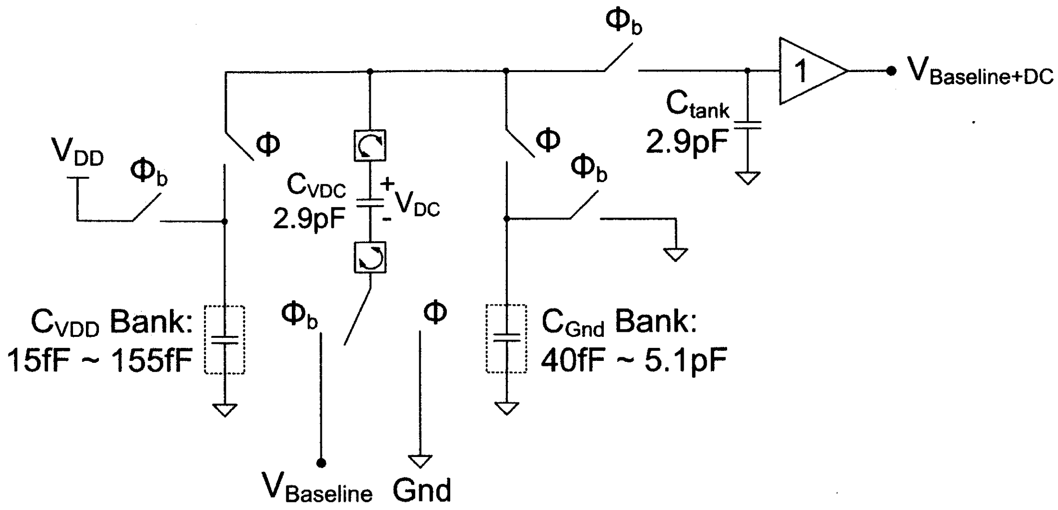

Figure 6-11: The V_{DC} generator schematic.

C_{VDD} is a 4-bit binary weighted capacitor bank of $15fF$ to $155fF$, and C_{Gnd} is a 7-bit binary weighted capacitor bank of $40fF$ to $5.1pF$. C_{VDD} and C_{Gnd} values are selected during the initial V_{DC} calibration by the microcontroller.

Non-overlapping clock phases Φ and Φ_b are generated on-chip at $1.9kHz$ by the clock generator (Section 6.3.5). The clock frequency is chosen as a compromise between low power (favors lower frequency) and low charge leakage (favors higher frequency).

During clock phase Φ_b (Figure 6-12(a)), C_{VDD} and C_{Gnd} are respectively reset to V_{DD} and ground. During the following clock phase Φ (Figure 6-12(b)), C_{VDC} is charged to a final voltage of $V_{DC} = V_{DD}C_{VDD}/(C_{VDD} + C_{Gnd})$. During the following clock phase Φ_b, V_{DC} is added to $V_{Baseline}$ to produce $V_{Baseline+DC}$, while C_{VDD} and C_{Gnd} are again reset. C_{tank} is present to reduce voltage ripples. With the selectable ranges of C_{VDD} and C_{Gnd}, V_{DC} can be adjusted from 0.29% to 79% of V_{DD}.

The simulated current consumption of the entire V_{DC} generator at $V_{DD} = 0.8V$ and $V_{DC} = 50mV$ is 2.0nA, of which 80% is used by the buffer amplifier.

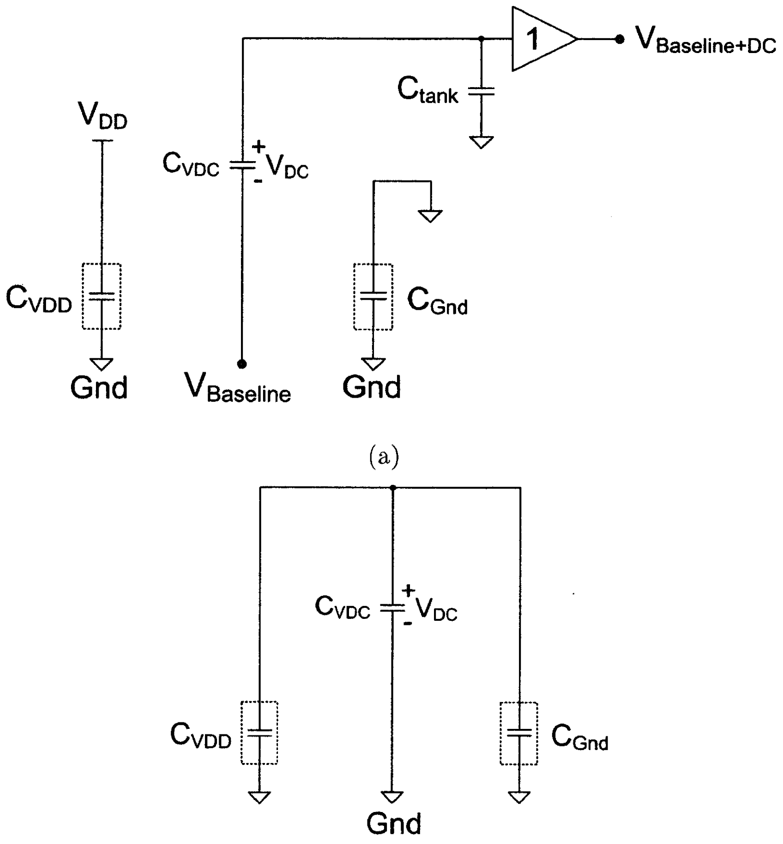

(a)

(b)

Figure 6-12: The V_{DC} generator in a) clock phase Φ_b and b) clock phase Φ.

In consideration for long term at-home usage where the ECG electrodes are applied by the wearer, the V_{DC} generator has the ability to generate negative V_{DC} if the user accidentally reverses the electrodes. This is symbolized by the two digital blocks in Figure 6-11 that can flip C_{VDC} during phase Φ_b. In the case that the ECG is reversed and C_{VDC} is flipped, then the heartbeat occurs when $D_{OUT} = 0$ instead of $D_{OUT} = 1$. These digital blocks are expanded in Figure 6-13.

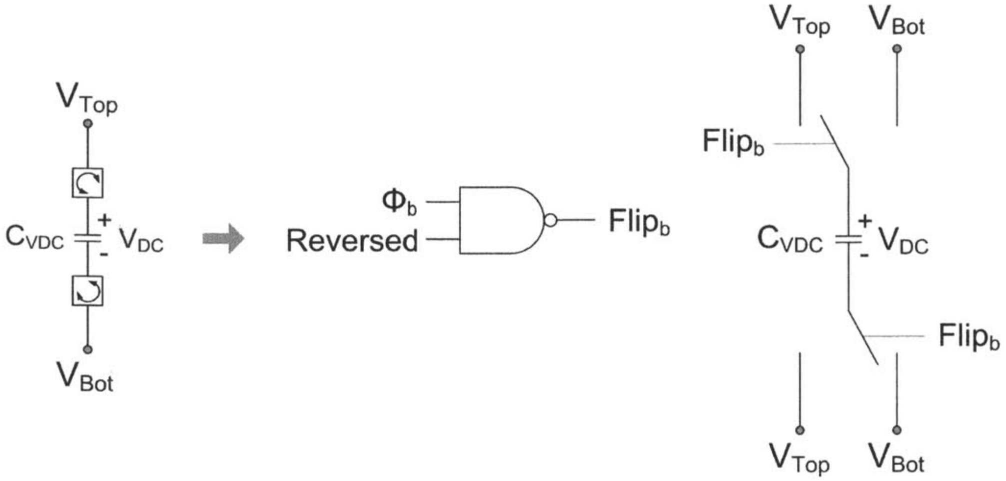

Figure 6-13: C_{VDC} can be flipped during phase Φ_b in case of reversed electrodes.

Because the switching frequency is only $1.9kHz$ and $C_{VDC} = 2.9pF$, a leakage current of only $5.5pA$ can reduce V_{DC} by $1mV$ between clock cycles. Therefore, all switches need to be low leakage switches to prevent capacitor discharge. To reduce leakage, stacked switches with a feedback buffer are implemented based on [73]. The switch schematic is shown in Figure 6-14.

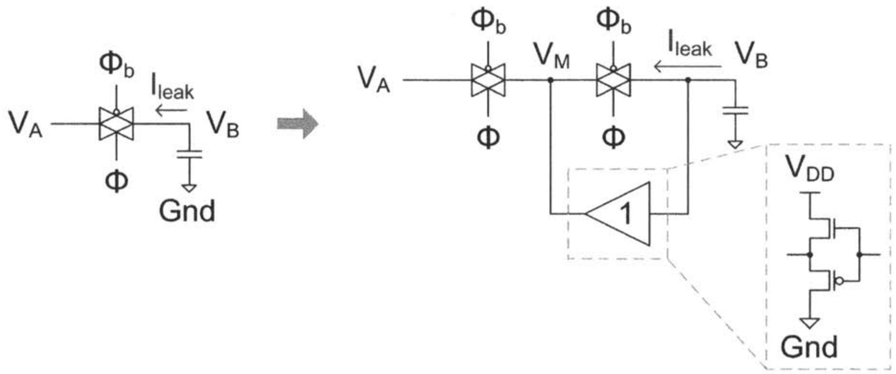

Figure 6-14: Low leakage switch implementation to prevent capacitor discharge.

The stacked switches reduce I_{leak} by decreasing the $|V_{GS}|$ of the switches. The feedback buffer uses a self-biased source follower to drive V_M to the same voltage as V_B, thus further decreasing I_{leak} by reducing the $|V_{DS}|$ of the switch closest to the capacitor.

6.3.4 The Comparator Design

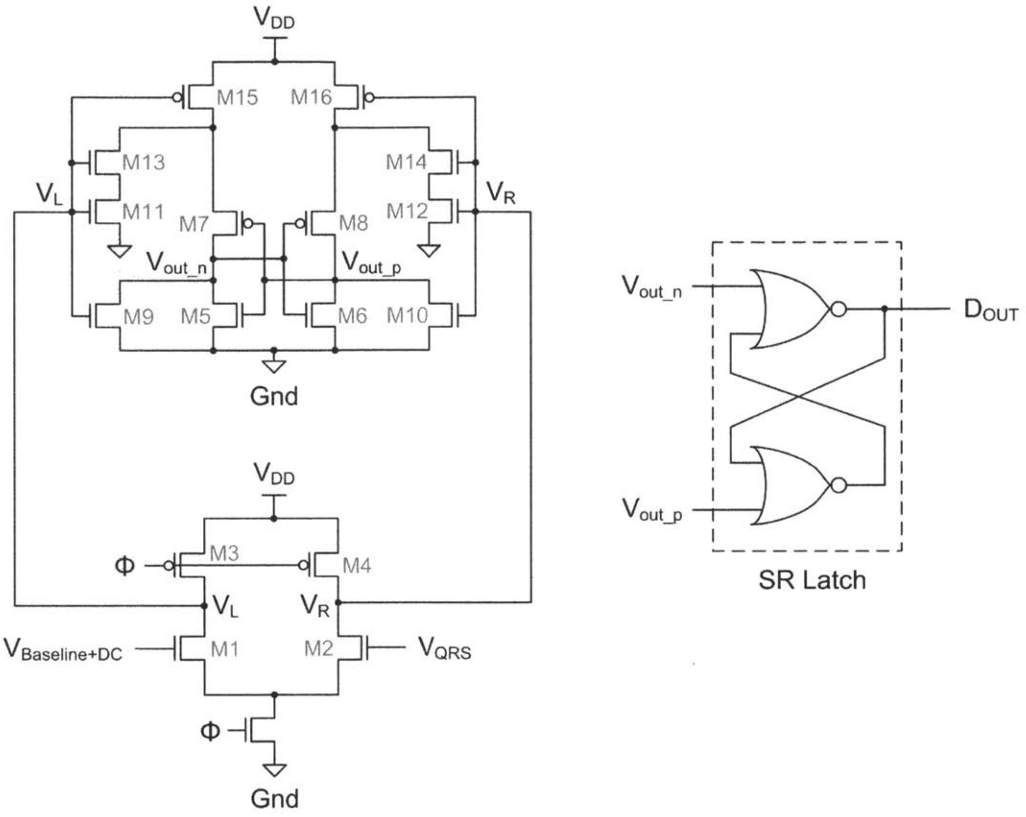

Figure 6-15: The dynamic latched comparator with SR latch.

The comparator's role is to output a digital "1" (or a digital "0" if the electrodes are reversed) when a QRS complex has occurred, which is when $V_{QRS} > V_{Baseline+DC}$. A dynamic latched comparator based on [74] is used (Figure 6-15). The dynamic topology is chosen because it consumes power only when latching. This topology offers the additional benefit of only using a single clock signal Φ, thus placing no requirements on Φ_b timing.

In Figure 6-15, when clock Φ is low, V_L and V_R are precharged to V_{DD} and all nodes of the cross-coupled inverter pair are discharged to ground. When clock Φ transitions from low to high, V_L and V_R begin to discharge through M1 and M2 to ground. If $V_{QRS} > V_{Baseline+DC}$, then V_R will discharge faster than V_L. Consequently, M12 and M14 will turn off sooner than M11 and M13, and M16 will turn on sooner than M15.

As a result, the source terminal of M8 will reach V_{DD} sooner than M7, thus raising V_{out_p} faster than V_{out_n}. The positive feedback amplifies this difference, causing the outputs to latch to a high V_{out_p} and a low V_{out_n}. Conversely, if $V_{QRS} < V_{Baseline+DC}$, then V_{out_p} will be low and V_{out_n} will be high.

M11 and M12 are added to reduce short circuit currents through M13 to M16 when V_L and V_R are transitioning. This is important because the short circuit currents can be several nano-amps. $V_{Baseline+DC}$ contains switching transients from the V_{DC} generator. However, these transients are designed to occur with Φ_b, which do not affect comparator accuracy because comparator latching occurs with Φ.

M1-M4 gate lengths are set at $1\mu m$ to reduce geometry mismatch. A Monte Carlo mismatch simulation of 100 runs produces an input-referred comparator offset range of $-13mV$ to $16mV$. However, as mentioned in Section 6.2, no comparator offset compensation is needed due to the V_{DC} calibration routine. The final output of the SR latch, D_{OUT}, is a digital signal that pulses when a heartbeat is detected.

The comparator's transistor dimensions are summarized in Table 6.5. The comparator's simulated current consumption at $V_{DD} = 0.8V$ with a clock frequency of $1.9kHz$ is $0.38nA$.

Transistor	**W/L × fingers** $[\mu m/\mu m]$
M1, M2	$1/1 \times 4 = 4/1$
M3, M4	$2/1 \times 4 = 8/1$
M5, M6	$1/0.5$
M7, M8	$2/0.5$
M9-M16	$1/2$

Table 6.5: Transistor dimensions of the comparator.

6.3.5 Peripheral Circuits

The ECG ASIC requires no off-chip active and passive components because all the peripheral circuits are on-chip. The peripheral circuits are designed to use less than 10% of the overall power consumption.

Current Reference

The current reference biases the currents of the PGA, QRS Amp, Baseline Amp, all buffer amplifiers, and clock generator. The current reference is based on the fast startup current reference in [75], which uses a startup circuit that consumes no static current. The schematic of the current reference is shown in Figure 6-16.

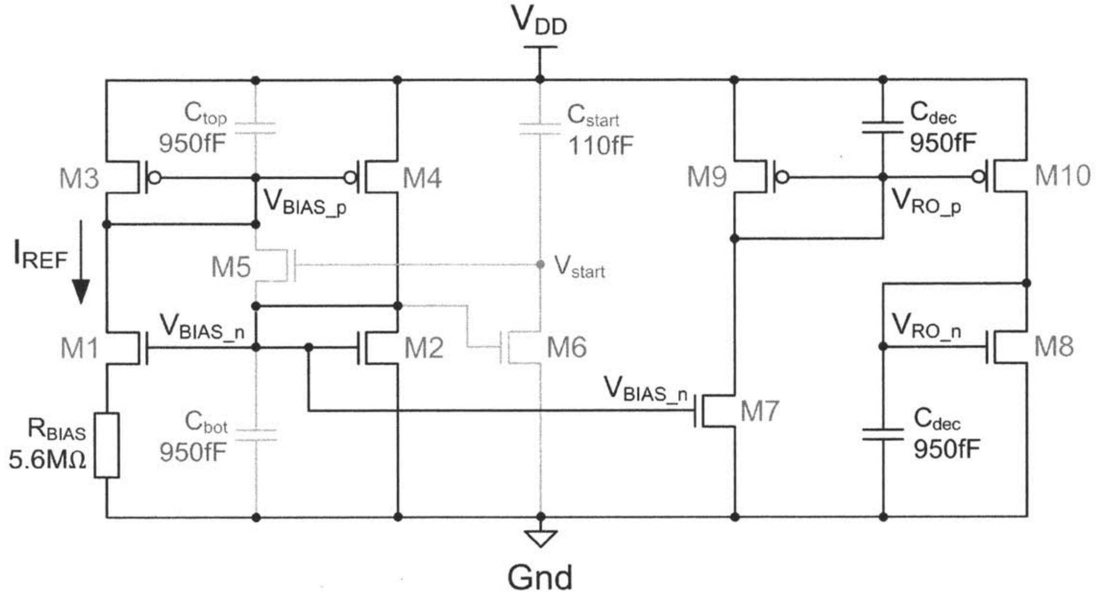

Figure 6-16: The current reference.

Transistors M1 to M4, along with R_{BIAS}, form the classic current reference where $I_{REF} = (V_{thermal}/R_{BIAS})ln(W_{M1}/W_{M2})$. R_{BIAS} is a high resistance poly resistor implemented on chip. With a designed ratio of $W_{M1}/W_{M2} = 9/8$, the I_{REF} is set to $0.55nA$. The voltage V_{BIAS_p} is distributed to all amplifiers to bias the tail current sources.

To avoid a startup state of $I_{REF} = 0$, the components in gray in Figure 6-16 comprise the startup circuit. The instant that V_{DD} is switched on, V_{BIAS_p} is at V_{DD} because of C_{top}, V_{BIAS_n} is at ground because of C_{bot}, and V_{start} is at V_{DD} because of C_{start}. This state turns on M5, which shorts V_{BIAS_p} and V_{BIAS_n}. In this instant, $V_{BIAS\_p} = V_{BIAS\_n} = V_{DD}/2$, which turns on M2 and M4 and the circuit is started. Meanwhile, M6 is on and discharges V_{start} to ground, thus turning off M5 and shutting off the startup circuit. C_{top} and C_{bot} remain as decoupling capacitors.

V_{BIAS_n} is routed to M7-M10 to create bias voltages V_{RO_p} and V_{RO_n} for biasing the starved ring oscillator in the clock generator.

The current reference's transistor dimensions are summarized in Table 6.6. The current reference's simulated current consumption at $V_{DD} = 0.8V$ is $2.8nA$.

Transistor	**W/L × fingers** $[\mu m/\mu m]$
M1	$1/1 \times 9 = 9/1$
M2	$1/1 \times 8 = 8/1$
M3, M4	2/1
M5, M6	4/0.5
M7	$1/1 \times 2 = 2/1$
M8	1/1
M9, M10	2/1

Table 6.6: Transistor dimensions of the current reference.

Voltage Reference

The function of the voltage reference is to generate $V_{CM} = V_{DD}/2$ for the common-mode voltage of the PGA. Absolute V_{CM} accuracy and temperature independence are not necessary. Therefore, a simple transistor diode ladder is used to generate V_{CM} as shown in Figure 6-17. All transistors are PMOS $(20\mu m/1\mu m)$ with body tied to source to avoid body effect. The voltage reference current consumption (including buffer) is simulated to be $2.8nA$. The simulated integrated noise is $21\mu V_{pp}$ from $1Hz$ to $100kHz$. A Monte Carlo simulation of 100 runs results in a V_{CM} standard deviation of $0.7mV$.

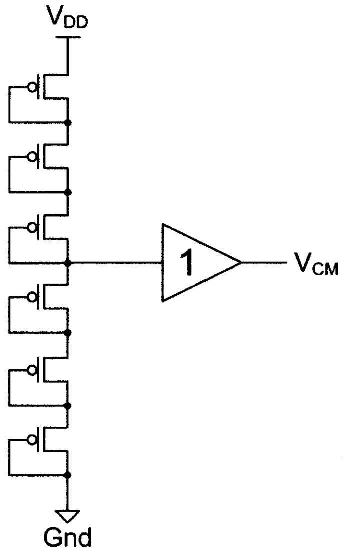

Figure 6-17: The voltage reference.

Clock Generator

The clock generator in Figure 6-18 provides the non-overlapping clock signals for the V_{DC} generator and the comparator. The clock is generated by a five-stage ring oscillator, which uses current-starved inverters biased by V_{RO_p} and V_{RO_n} from the current reference. The $30fF$ capacitive loads ensure that a rail-to-rail oscillation is achieved.

Following the ring oscillator is a four-stage starved inverter chain of increasing currents. This chain is crucial in reducing the short-circuit current in the subsequent non-starved inverters, which can be as high as tens of nano-amps. After a three-stage non-starved inverter chain, a non-overlapping clock generator is used to produce clock signals Φ and Φ_b. Non-overlapping clocks are required for the switched-capacitor V_{DC} generator. The clock generator's simulated current consumption at $V_{DD} = 0.8V$ and a clock frequency of $2kHz$ is $2.0nA$.

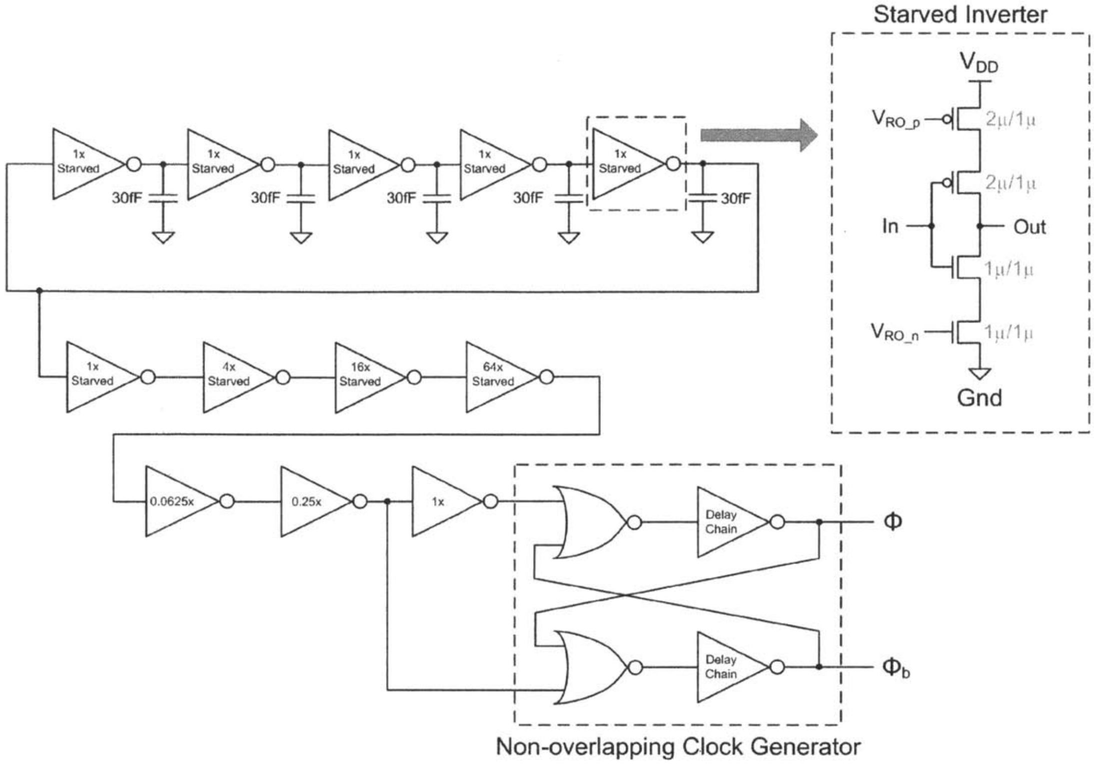

Figure 6-18: The clock generator.

Configuration Registers

The configuration registers load 77 bits of configuration settings into the ASIC using shift registers. The shift registers are modified to be able to serially read out internal bits for verification. The configuration settings include:

- PGA gain settings (6 bits)
- PGA bandwidth and power settings (10 bits)
- QRS Amp bandwidth and power settings (14 bits)
- Baseline Amp bandwidth and power settings (14 bits)
- C_{Gnd} settings (7 bits)
- C_{VDD} settings (4 bits)

- Reverse V_{DC} (1 bit)
- Current reference settings (15 bits)
- Voltage reference settings (3 bits)
- Clock frequency settings (3 bits)

6.3.6 Physical Layout Considerations

Device matching of the analog circuits is crucial because all devices operate in subthreshold and high CMRR is required to reject common-mode interferers. To improve matching, common-centroid layout with edge dummies is used for all amplifiers. To avoid geometry-dependent variations, ratioed transistors used in the current mirrors and ratioed capacitors use the same unit geometries and are scaled via multiples. All analog circuits are isolated using dual guard rings. All digital circuits are also isolated by dual guard rings and are placed apart from the analog circuits. An example is shown in Figure 6-19, where the PGA layout shows common-centroid layout of input and mirror transistors, multiples of current mirror transistors (ratioed to the current reference), and dual guard rings.

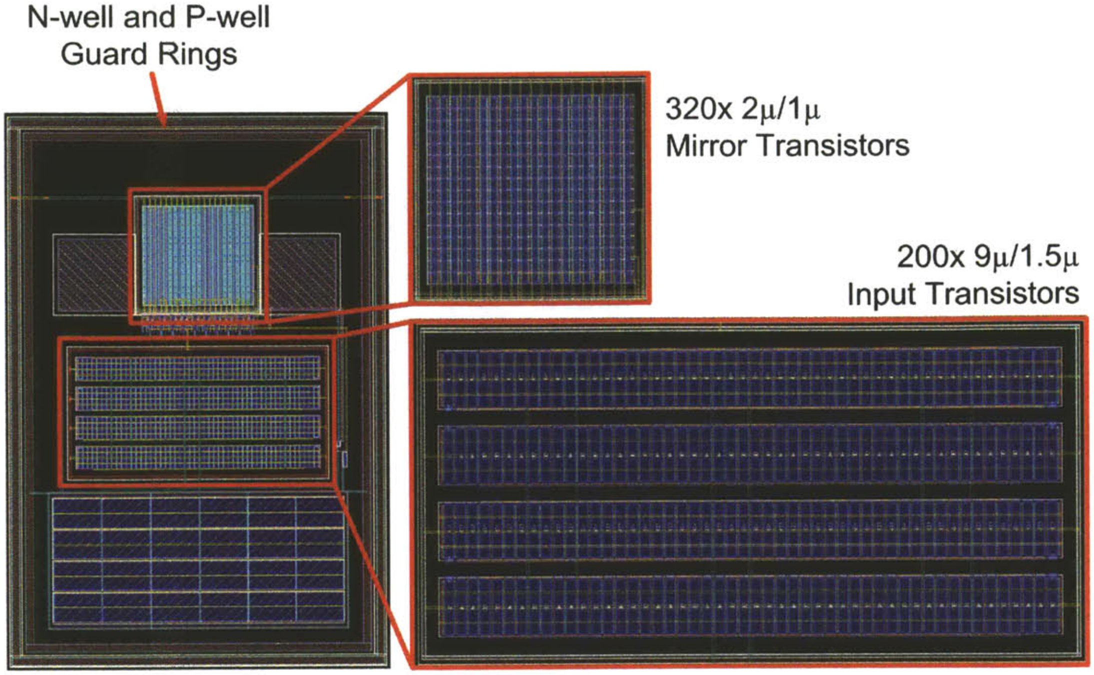

Figure 6-19: The physical layout of the PGA showing the common-centroid input transistors (denoted as A for M1, B for M2, and D for dummy), the ratioed current mirror transistors, and the dual guard rings.

6.4 The ECG ASIC Measurement Results

The ASIC is fabricated using the TSMC $0.18\mu m$ CMOS technology. The die area is $1.8mm \times 1.8mm$ with an active area of $0.76mm^2$ as shown in Figure 6-20.

The die is packaged in a $9mm \times 9mm$ QFN-64 chip for bench testing where V_{DD}'s are isolated and all internal blocks can be probed (Figure 6-21(a)). The die is also packaged in a $3mm \times 3mm$ QFN-16 chip for mounting onto the existing wearable platform for wireless and mobile measurements (Figure 6-21(b)).

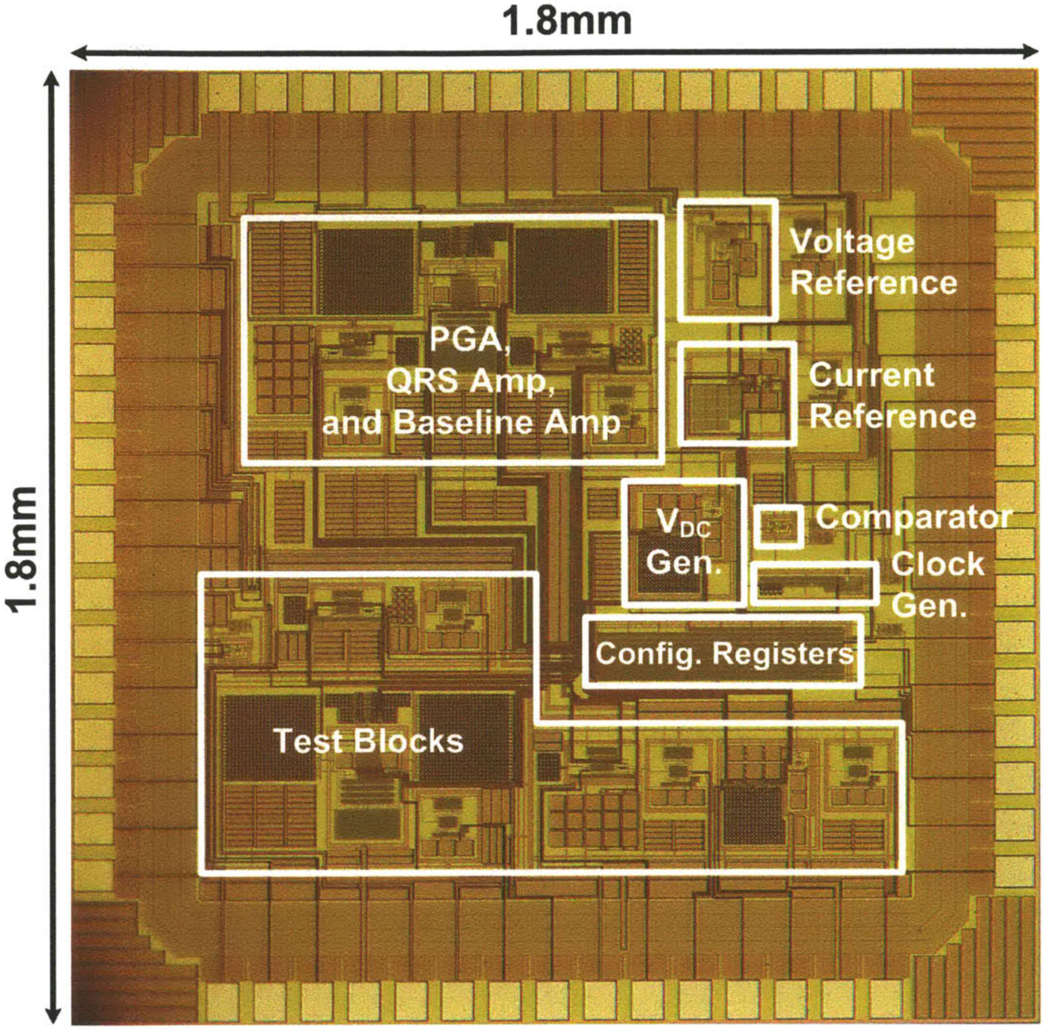

Figure 6-20: Die micrograph of the ECG ASIC with the circuit blocks labeled.

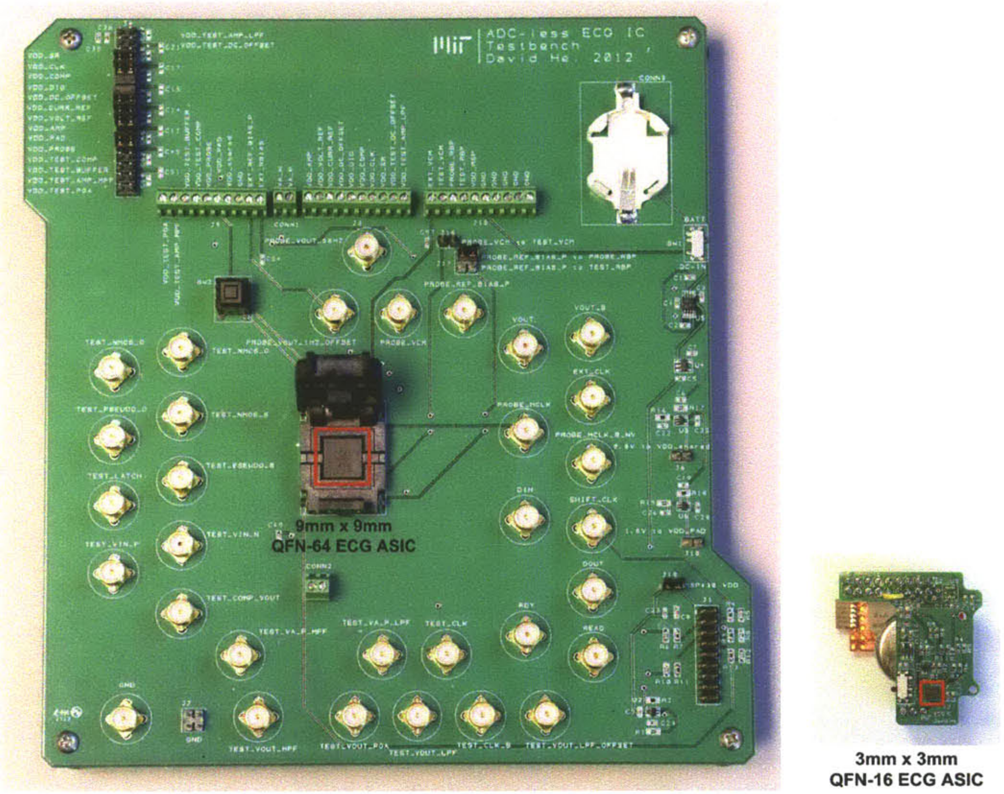

(a) (b)

Figure 6-21: a) The bench-level PCB with the QFN-64 ASIC in socket, and b) the wearable PCB with the QFN-16 ASIC. The figures are to scale.

6.4.1 The Amplifier Gain and Noise Response

The ECG's amplification path goes through the PGA and then the QRS Amp. Figure 6-22 shows the gain response and input-referred noise response at the highest gain setting. In the gain response, the plot shows the sub-Hz high pass corner enabled by the PGA and QRS Amp's pseudo-resistors, the low pass corner implemented by the QRS Amp's low g_m and large compensation capacitor, and the $40dB/dec$ fall off at higher frequencies due to the two poles from the PGA and the QRS Amp. In terms of noise response, the circuit exhibits a $1/f$ characteristic below $10Hz$ (or $1/\sqrt{f}$ when using $V/\sqrt{Hz}$ as unit). The noise below 0.5Hz is filtered by two sub-Hz high pass corners from the PGA and the QRS Amp's pseudo-resistors.

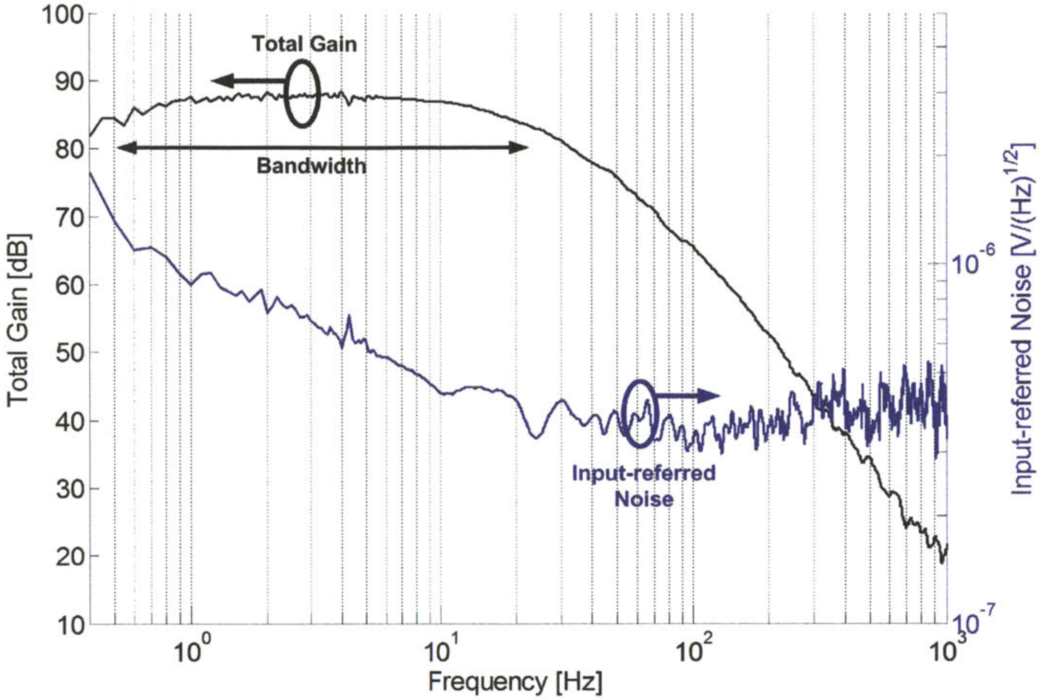

Figure 6-22: The PGA-QRS Amp signal path's gain response and noise response measured using an Agilent 35670A Dynamic Signal Analyzer.

Table 6.7 shows the simulated and measured results from the PGA-QRS Amp signal path.

Parameter	**Simulated**	**Measured**
Programmable gain range	$47dB - 84dB$	$47dB - 88dB$
Passband	$0.52Hz - 51Hz$	$0.5Hz - 22Hz$
Unity-gain bandwidth	$6.4kHz$	$2.9kHz$
Input-referred noise (in band)	$0.99\mu V_{rms}$	$2.7\mu V_{rms}$
CMRR	$78dB$	$66dB$
PSRR	$53dB$	$61dB$
Current consumption (at $0.8V$)	$92nA$	$64nA$

Table 6.7: Measured results from the PGA-QRS Amp signal path.

Increasing the transistor bias currents did not appreciably decrease the input-referred noise, which indicates that the in-band noise is 1/f dominated as Figure 6-22 indicates. The measured input-referred noise is greater than the simulated noise by 2.7 times, which is likely attributed to differences between the transistor model's and the production's 1/f characteristics. The measured level of noise is compatible with sensing the ECG at the head, where the QRS amplitude is approximately $30\mu V_{pp}$.

A widely used figure of merit for amplifier power-noise performance is the Noise Efficiency Factor (NEF) proposed in [76].

$$NEF = V_{ni,rms}\sqrt{\frac{2I_{total}}{\pi V_{thermal}4kTBW}} \tag{6.2}$$

In Equation (6.2), $V_{ni,rms}$ is the input-referred RMS noise voltage, I_{total} is the total amplifier supply current, and BW is the amplifier bandwidth in Hertz. The NEF for the PGA-QRS Amp circuit blocks is 5.7. Figure 6-23 compares the ECG ASIC's amplifier performance with published biopotential front-end amplifiers, where it is the lowest powered amplifier with an NEF of less than 10.

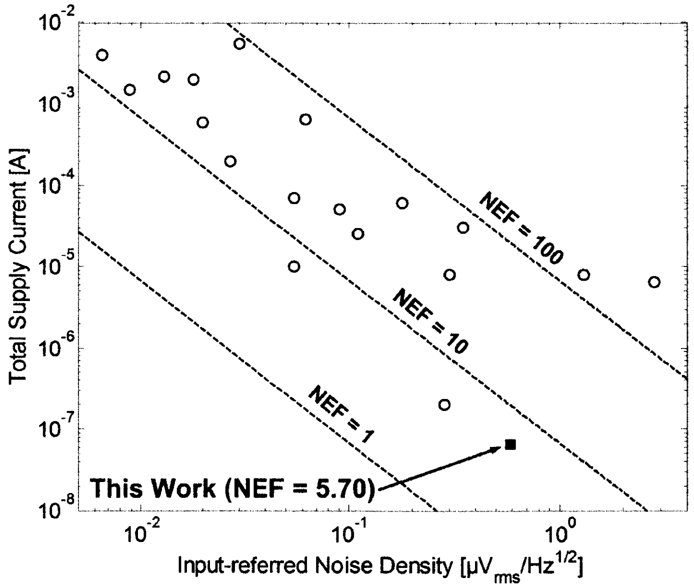

Figure 6-23: A comparison of the PGA-QRS Amp's NEF with published biopotential amplifiers. The data is adapted from [70] and [77].

6.4.2 ECG Measurements

Figures 6-24 to 6-27 show measured ECG and digital outputs from various wearable ECG scenarios to demonstrate the ASIC's robustness in the presence of baseline drift, muscle artifacts, and attenuated signal.

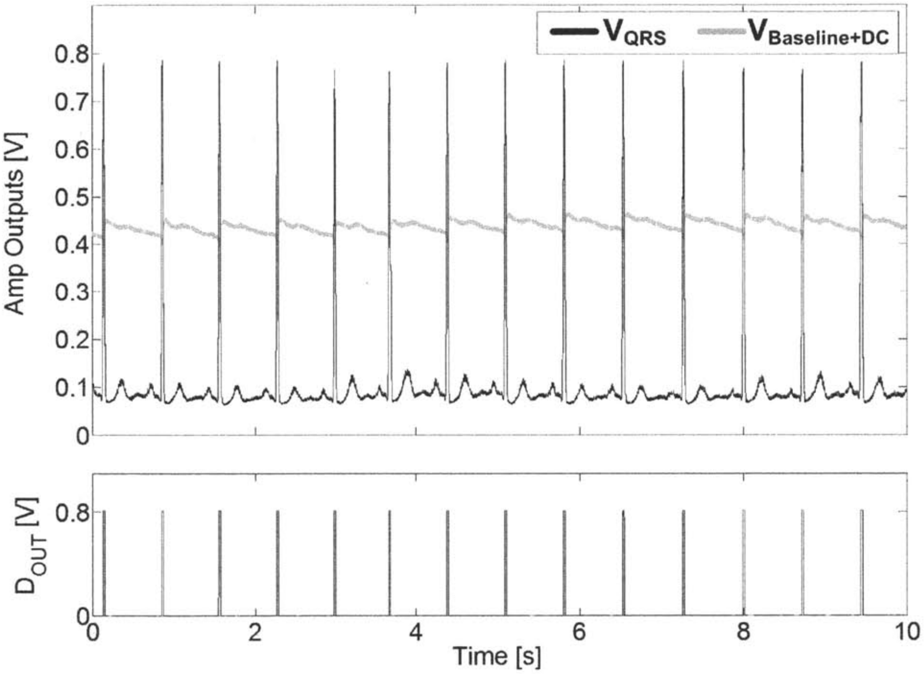

Figure 6-24: Chest ECG at rest ($gain = 52dB$).

In Figure 6-24, the at-rest chest ECG offers $1.8mV_{pp}$ of stable signal. Here, V_{DC} is set to $0.3V$ so that $V_{Baseline+DC}$ is approximately half of the V_{QRS} amplitude. However, any V_{DC} setting between $0.1V$ and $0.65V$ would produce the correct digital QRS output at D_{OUT}.

In Figure 6-25, the chest ECG contains significant baseline drift due to motion. Despite the baseline drift, the same V_{DC} setting as in Figure 6-24 results in a correct D_{OUT}. In fact, any V_{DC} setting between $0.1V - 0.5V$ would be valid. This demonstrates the ASIC's tolerance to motion artifacts because its adaptive threshold $V_{Baseline+DC}$ tracks the baseline drift.

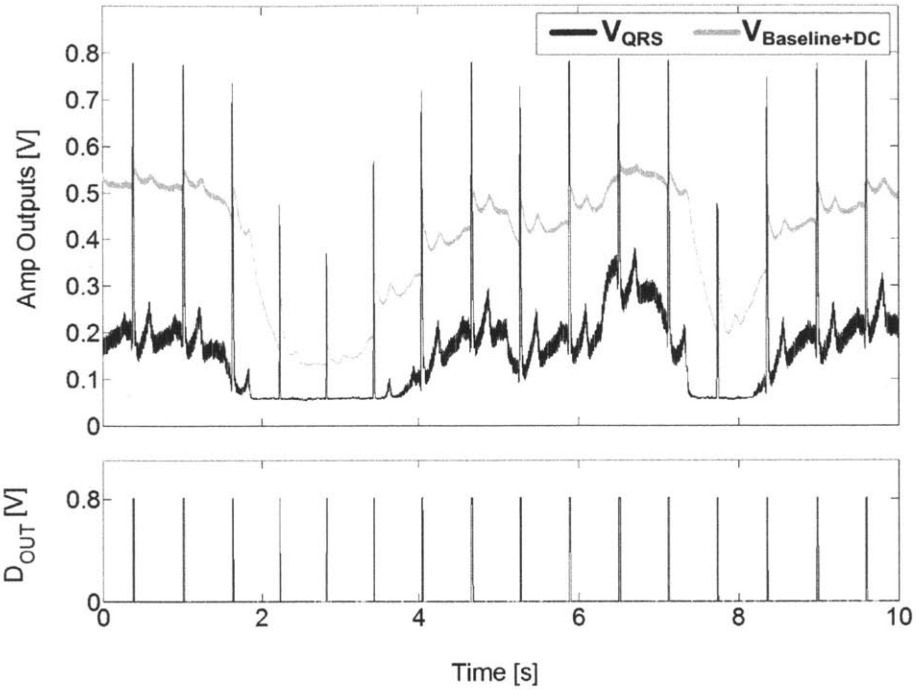

Figure 6-25: Chest ECG with baseline drift due to motion ($gain = 52dB$).

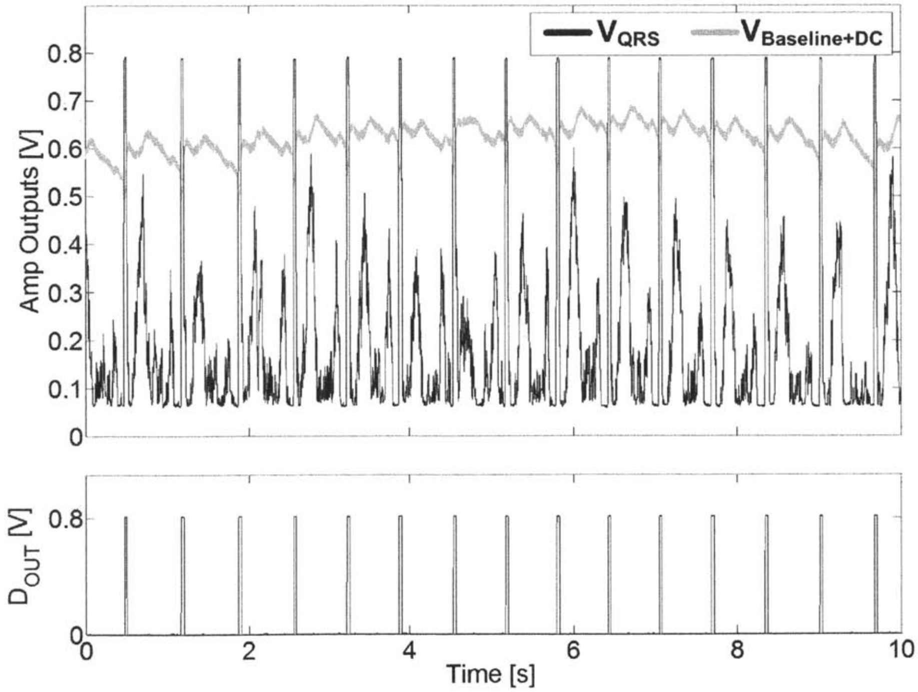

Figure 6-26: Chest ECG with muscle artifacts and signal clipping ($gain = 64dB$).

In Figure 6-26, pectoral muscle artifacts are present from a rapid horizontal 90° arm movement. Also, the higher gain of $64dB$ increases the amplified ECG to $2.8V_{pp}$, which is beyond $V_{DD} = 0.8V$ and is clipped. To produce the correct D_{OUT}, V_{DC} needs to be increased to $0.5V$ so that $V_{Baseline+DC}$ rises above V_{QRS}'s muscle artifacts and heightened T-waves. The QRS complex's clipping does not matter because the beat information is still present. From this scenario, it can be seen that as the measurement condition changes, new V_{DC} settings are required. The need to recalibrate V_{DC} can be detected in real time when D_{OUT} exceeds human heart rate range or when D_{OUT} becomes irregularly spaced. Once detected, the calibration routine described in Section 6.2 can be rerun to update V_{DC}.

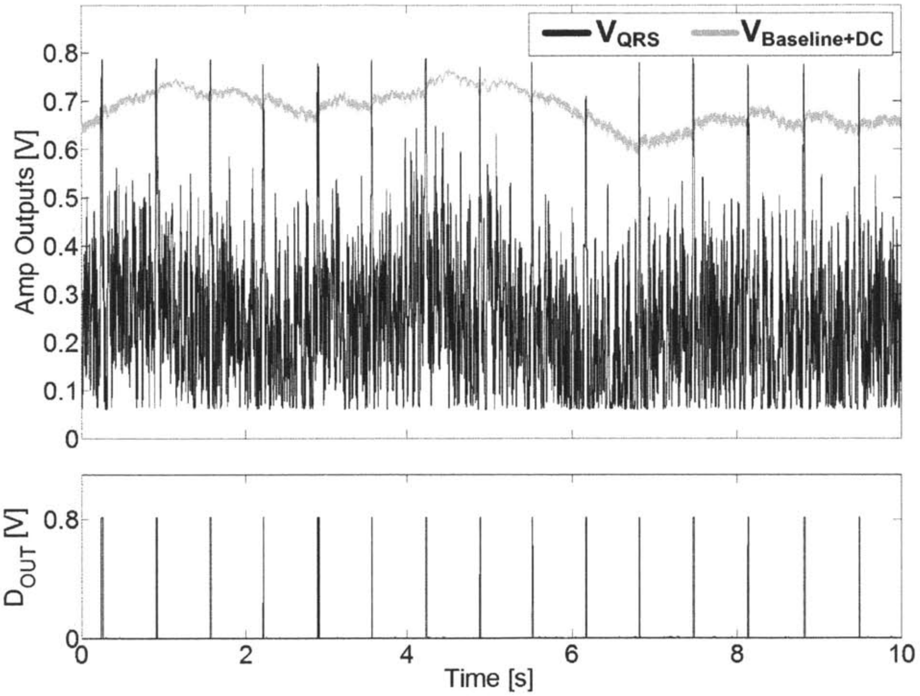

Figure 6-27: Ear-neck ECG with high gain and low SNR ($gain = 84dB$).

In Figure 6-27, the ECG is measured across the ear and the middle upper neck. This remote ECG vector is used in the wearable heart monitor. The gain is increased to $84dB$ to sense the $30\mu V_{pp}$ of ear ECG. At this high gain, a significant portion of the amplified output is noise and QRS clipping is present. However, with the identical

V_{DC} setting as in Figures 6-24 and 6-25, $V_{Baseline+DC}$ is able to rise above the noise and correctly capture the QRS complexes as shown by D_{OUT}.

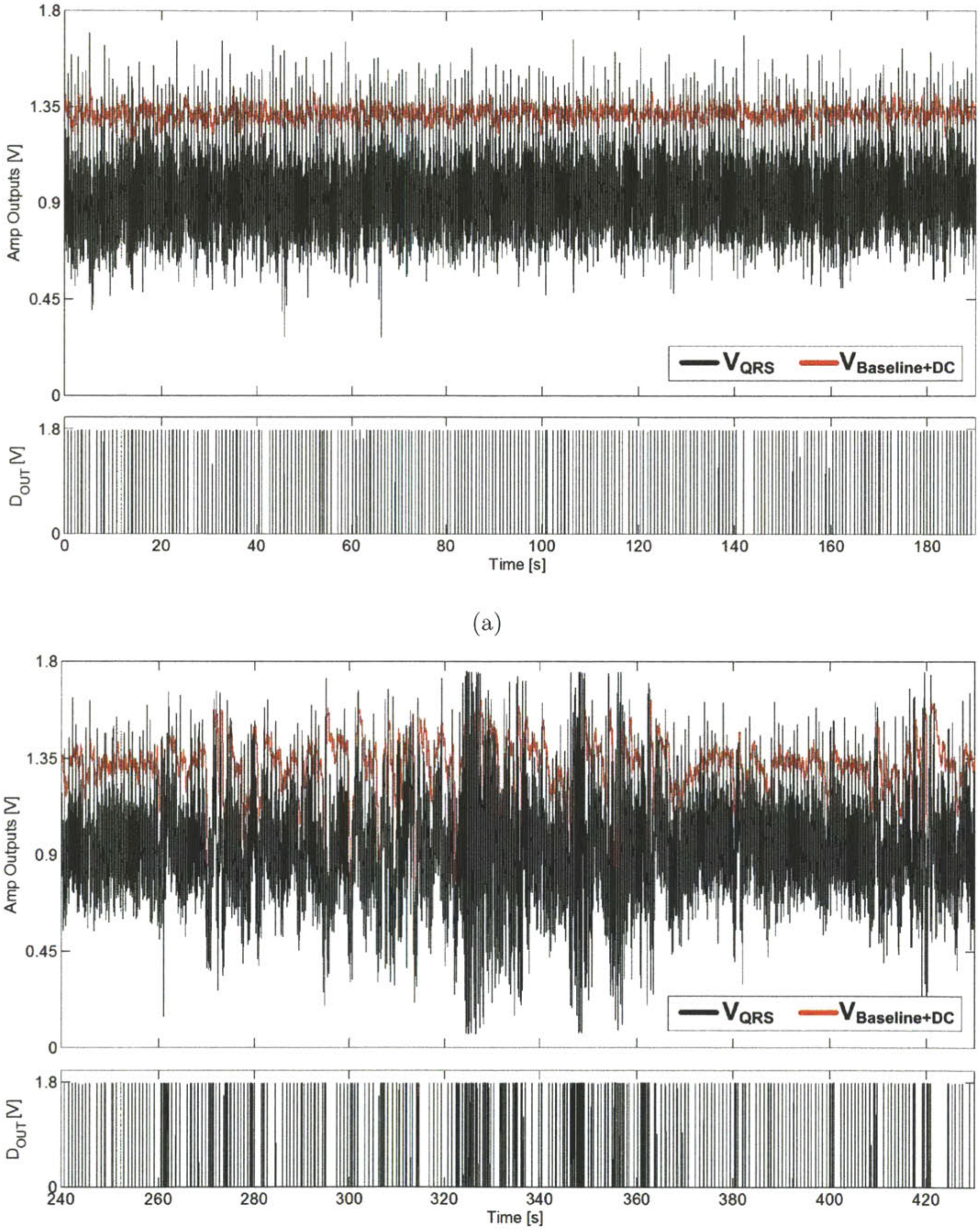

(a)

(b)

Figure 6-28: Ear-neck ECG at $V_{DD} = 1.8V$ and $gain = 84dB$ during a) rest, and b) moderate head motion.

Because the attenuated ECG near the ear requires high gain, it is very sensitive to motion. In this scenario, a higher V_{DD} is beneficial to provide a wider dynamic range. Figure 6-28(a) shows a 190s measurement of the head ECG at $V_{DD} = 1.8V$ using the same lead as in Figure 6-27. Among the total number of 255 heartbeats, the ASIC misses 11 beats (sensitivity of 95.7%) and erroneously captures 4 extra beats (positive predictive value of of 98.5%). However, when there is moderate head motion in Figure 6-28(b), the motion artifacts overwhelm the QRS complexes and the ASIC is unable to reliably extract heartbeats.

6.4.3 Power Measurements

The power consumptions of the circuit blocks are measured using a Keithley 2400 SourceMeter with an averaging filter of 100 samples. Table 6.8 lists the power consumption of each circuit block at $V_{DD} = 0.8V$. 87% of total power is allocated to the PGA due to bandwidth and thermal noise considerations. The peripheral circuits consume 8.6% of the total power.

Circuit block	**Simulated Power (nW)**	**Measured Power (nW)**
PGA	72.8	50.4
QRS Amp	0.5	0.7
Baseline Amp	0.5	0.7
V_{DC} generator	1.6	0.8
Comparator	0.3	0.4
Current reference	2.2	1.8
Voltage reference	2.2	1.0
Clock generator	2.0	2.2
Total	82.0	58.0

Table 6.8: Power breakdown of each circuit block at $V_{DD} = 0.8V$.

The ECG ASIC's elimination of ADC and signal processor enables it to reduce power consumption and to occupy a smaller die area. Another portion of the power saving is contributed by the PGA's low bandwidth and simple architecture, which is single-ended and does not use chopper modulation nor DC servo loops for biasing. A further source of power saving is the ECG ASIC's low V_{DD}, which is enabled by its tolerance to signal clipping.

The ECG ASIC has sufficiently low energy consumption for one year of continuous operation from a $0.7mAh$ thin-film battery, making it ideal for miniaturized and long term heart monitoring. Besides being suitable for the presented wearable heart monitor, the ECG ASIC is useful for battery-constrained ECG applications such as implantable pacemakers and defibrillators. Furthermore, the ECG ASIC's power consumption is in range of energy harvesting power sources, thus making batteryless heart monitors a possibility.

6.5 Recovering the ECG R-wave Timing from D_{OUT}

Accurate ECG R-wave timing is necessary for the calculations of pre-ejection period (PEP) and pulse arrival time (PAT) for cuffless blood pressure estimation, and for the calculation of the RR interval for heart rate variability (HRV) analysis. Although the R-wave is clipped and its peak is lost in the eventual digital output D_{OUT}, this section shows that the original R-wave timing can be recovered with minimal error.

As shown by Figure 6-29, the R-wave timing can be estimated from the midpoint timing of D_{OUT} pulses. This method is tested on normal chest ECG records from ten subjects totaling 2,304 heartbeats. Subjects 1 to 5 are from the MIT-BIH PhysioNet database, and Subjects 6 to 10 are from the MIT clinical test (Chapter 5). Estimated R-wave timings are compared with manually annotated timings. A sample result segment is shown in Figure 6-30. The results for all ten subjects are summarized in Table 6.9.

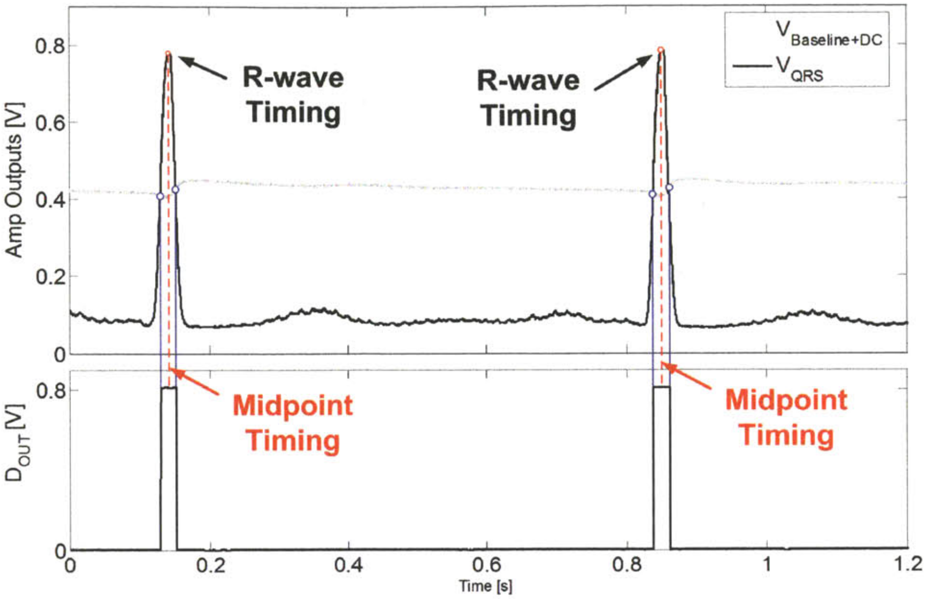

Figure 6-29: Estimation of the R-wave timing using the midpoint timing of D_{OUT}.

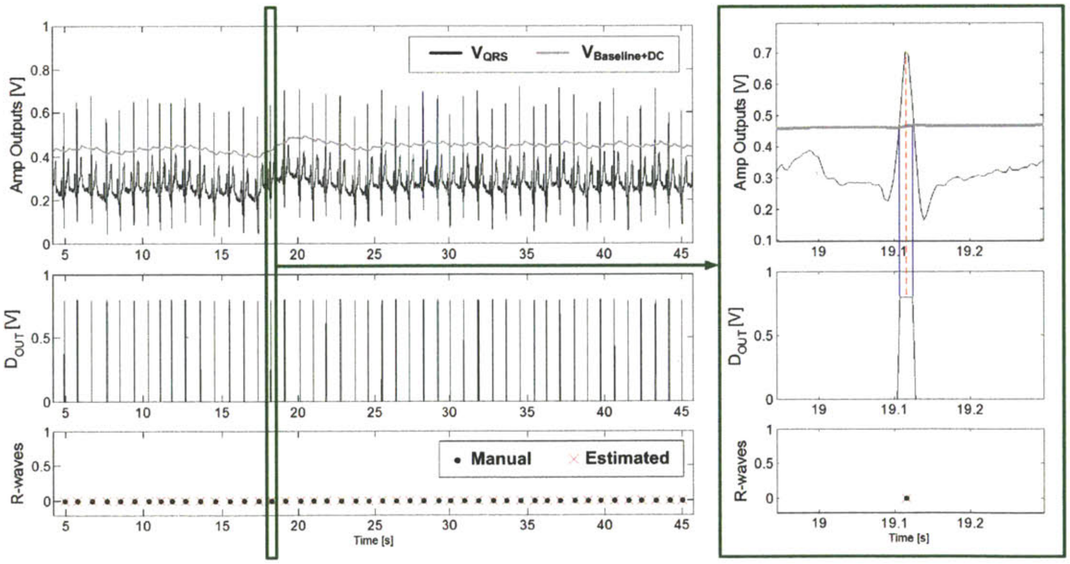

Figure 6-30: Estimation of R-wave timings on a sample ECG segment from PhysioNet database.

Subject	**Number of Beats**	**Mean R-wave Timing Error [ms]**	**Stdev. R-wave Timing Error [ms]**	**Sampling Freq. [Hz]**
1	250	0.91	1.6	250
2	183	0.91	1.6	250
3	63	0.97	2.2	250
4	123	-1.70	1.6	250
5	73	-2.40	1.8	250
6	467	-1.50	0.71	500
7	363	-1.00	0.71	500
8	357	-2.80	0.72	500
9	226	-0.88	0.72	500
10	199	-0.29	0.84	500
Overall	**2,304**	**-0.70**	**1.25**	-

Table 6.9: Comparison between midpoint-estimated R-wave timings and manually annotated R-wave timings from ten subjects.

The mean R-wave timing error arises from the fact that the QR slope may be different from the RS slope, thus resulting in the R-wave not being exactly at the midpoint. Nine out of ten subjects' mean R-wave timing error is within the sampling period ($4ms$ and $2ms$). In six out of ten subjects, the estimation is accurate to within $1ms$ of the actual R-wave timing. The standard deviation of R-wave timing error is mainly due to time quantization caused by sampling. As expected, when the sampling frequency is doubled for subjects 6 to 10, the standard deviation of R-wave timing error approximately halves. In nine out of ten subjects, the standard deviation of R-wave timing error is less than half of the sampling period. In summary, the R-wave midpoint estimation method is an accurate way to recover the ECG peak timing information from D_{OUT}. This enables the use of the ECG ASIC for applications beyond heartbeat detection, such as cuffless blood pressure estimation and HRV analysis, both of which require accurate R-wave timings.

Chapter 7

Conclusion

7.1 Summary of Contributions

In summary, this work presents a wearable heart monitor that uses the head ballistocardiogram (BCG) and the head electrocardiogram (ECG) to extract heart rate, stroke volume, respiratory rate, and pre-ejection period (PEP).

The ear is demonstrated as a viable location for the integrated sensing of physiological signals. Physiologically, the ear location is shown to provide BCG, ECG, and photoplethysmogram (PPG) signals. Mechanically, the ear provides a discreet and natural anchoring point that reduces the need for adhesives.

Periodic head movements are identified as a type of BCG. Two methods of measuring the head BCG are implemented. The accelerometer method allows the portable measurements of the BCG without the use of electrodes. Using ensemble averaging, the morphology of the head BCG is shown to closely represent the traditional BCG waveform. One direct application of the head BCG is electrode-less heart rate monitoring. Another application is the estimation of stroke volume based on the BCG amplitude.

This work also demonstrates the ability to measure the ECG near the ear. Using both BCG and ECG signals, an electromechanical timing duration called the RJ interval can be obtained. From heart timings, the RJ interval is shown to correlate to PEP. Because both head BCG and ECG have low signal quality, cross-correlation is used to statistically extract the RJ interval without the use of peak detection.

A clinical prototype is developed that allows the portable measurements of the BCG and the ECG at the ear while wirelessly transmitting the data to a computer. A clinical test involving hemodynamic maneuvers is performed on 13 subjects. The test results demonstrate a linear relationship between J-wave amplitude and stroke volume across subjects. Also, the RJ intervals extracted from the head BCG and the head ECG are shown to be linearly proportional to PEP across subjects.

A $58nW$ ECG application-specific integrated circuit (ASIC) for long term heart monitoring is implemented. A new topology is presented that takes advantage of the ECG's characteristics to extract heartbeat timings in the presence of motion and muscle artifacts, signal clipping, and ECG signals as low as $30\mu V$. The extracted timings can be used for heart rate, RJ interval, and pulse arrival time (PAT) calculations. With the goal of reducing battery size and consequently overall device size, the circuit's power consumption and area are aggressively reduced due to the elimination of traditional circuit blocks and due to low power circuit design.

7.2 Future Work

As of writing, the PPG component of the system is currently being converted to an integrated solution by Eric Winokur at MIT. This will reduce both overall device size and total power consumption.

Further validation of the relationship between pulse transit time (PTT) and blood pressure is needed. This is best performed in a controlled setting where a gold standard measurement of blood pressure is available, such as in a hospital on patients with arterial lines. Long test durations are necessary to determine the frequency of calibration needed for accurate blood pressure estimates.

Additional validation of the relationship between J-wave amplitude and stroke volume needs to be performed. The problem with the clinical test in this thesis work is that the hemodynamic maneuvers mechanically affect J-wave amplitude. For example, a supine posture dampens the J-wave amplitude due to friction, thus masking any physiological effects due to changed stroke volume. As a result, only the standing posture is analyzed in the current work.

In its present implementation, the system sends continuous real time data wirelessly to the PC for analysis. A future implementation will perform the analysis on the microcontroller and periodically send scalar data such as heart rate and heart intervals to the PC. This will significantly reduce the radio's duty cycle and average power consumption. As of writing, work is currently underway to port the MATLAB algorithms to the MSP430 in an energy efficient manner. This work is being done by Xianzhen Zhu at MIT.

At time of writing, work is also being done to change the radio from a proprietary 2.4GHz protocol to the Bluetooth 4.0 Low Energy (BLE) protocol. Compared to the current radio, BLE allows larger data packets and bandwidth, lower power consumption, and interoperability with mobile devices. This work is being done by Lyne Tchapmi at MIT.

Bibliography

[1] P.A. Heidenreich et al. Forecasting the future of cardiovascular disease in the united states: a policy statement from the american heart association. *Circulation*, 123:933–944, 2011.

[2] J.E.P. Waktare. Atrial fibrillation. *Circulation*, 106(1):14–16, 2002.

[3] V.L. Roger et al. Heart disease and stroke statistics 2012 update. *Circulation*, 125(1):e2–e220, 2012.

[4] A.M. Weissler, W.S. Harris, and C.D. Schoenfeld. Systolic time intervals in heart failure in man. *Circulation*, 37(2):149–159, 1968.

[5] C.L. Garrard Jr., A.M. Weissler, and H.T. Dodge. The relationship of alterations in systolic time intervals to ejection fraction in patients with cardiac disease. *Circulation*, 42:455–462, 1970.

[6] W. Chen and D. Gibson. Mechanisms of prolongation of pre-ejection period in patients with left ventricular disease. *Br. Heart J.*, 42:304–310, 1979.

[7] C. Yancy and W.T. Abraham. Noninvasive hemodynamic monitoring in heart failure: utilization of impedance cardiography. *Congest Heart Fail.*, 9(5):241–250, 2003.

[8] D.M. Lloyd-Jones et al. Heart disease and stroke statistics 2010 update. *Circulation*, 121(7):e46–e215, 2010.

[9] D.M. Lloyd-Jones et al. Novel approach to examining first cardiovascular events after hypertension onset. *Hypertension*, 45(1):39–45, 2005.

[10] P. Verdecchia et al. Circadian blood pressure changes and left ventricular hypertrophy in essential hypertension. *Circulation*, 81(2):528–536, 1990.

[11] T. Ohkubo et al. Prognosis of masked hypertension and white-coat hypertension detected by 24-h ambulatory blood pressure monitoring, 10-year follow-up from the ohasama study. *Journal of the American College of Cardiology*, 46(3):508–515, 2005.

[12] D.G. Guo et al. A long-term wearable vital signs monitoring system using bsn. In *Digital System Design Architectures, Methods and Tools, Conference on*, pages 825–830, 2008.

[13] J.W. Gordon. On certain molar movements of the human body produced by the circulation. *J. Anat. Physiol.*, 11:533–536, 1877.

[14] I. Starr et al. Studies on the estimation of cardiac output in man, and of abnormalities in cardiac function, from the heart's recoil and the blood's impacts; the ballistocardiogram. *The American Journal Of Physiology*, 127(1):1–28, 1939.

[15] S. Kakinada. Surgi-cell. `http://surgi-cell.blogspot.com/2010/03/cant-we-all-just-get-along.html`.

[16] A.M. Weissler. *Noninvasive Cardiology.* Grune and Stratton, Inc., New York, NY, USA, 1974.

[17] H. Mandelbaum and R.A. Mandelbaum. Studies utilizing the portable electromagnetic ballistocardiograph: Iv. the clinical significance of serial ballistocardiograms following acute myocardial infarction. *Circulation*, 7:910–915, 1953.

[18] I. Starr and F.C. Wood. Twenty-year studies with the ballistocardiograph: The relation between the amplitude of the first record of healthy adults and eventual mortality and morbidity from heart disease. *Circulation*, 23:714–732, 1961.

[19] L. Giovangrandi et al. Ballistocardiography; a method worth revisiting. In *IEEE Engineering in Medicine and Biology Conference*, pages 4279–4282, 2011.

[20] O.T. Inan. Recent advances in cardiovascular monitoring using ballistocardiography. In *IEEE Engineering in Medicine and Biology Conference*, pages 5038–5041, 2012.

[21] O.T. Inan et al. Robust ballistocardiogram acquisition for home monitoring. *Physiological Measurement*, 30(2):169, 2009.

[22] J.H. Shin, K.M. Lee, and K.S. Park. Non-constrained monitoring of systolic blood pressure on a weighing scale. *Physiological Measurement*, 30(7):679, 2009.

[23] K.K. Kim et al. A new method for unconstrained pulse arrival time (pat) measurement on a chair. *J. Biomed. Eng. Res.*, 27:83–88, 2006.

[24] T. Koivistoinen et al. A new method for measuring the ballistocardiogram using emfi sensors in a normal chair. In *IEEE Engineering in Medicine and Biology Conference*, pages 2026–2029, 2004.

[25] O. Postolache et al. Vital signs monitoring system based on emfi sensors and wavelet analysis. In *Instrumentation and Measurement Technology Conference Proceedings*, pages 1–4, 2007.

[26] G.S. Chung et al. Wakefulness estimation only using ballistocardiogram: Nonintrusive method for sleep monitoring. In *IEEE Engineering in Medicine and Biology Conference*, pages 2459–2462, 2010.

[27] C. Bruser et al. Adaptive beat-to-beat heart rate estimation in ballistocardiograms. *Information Technology in Biomedicine, IEEE Transactions on*, 15(5):778–786, 2011.

[28] P.-F. Migeotte et al. Three dimensional ballistocardiography: Methodology and results from microgravity and dry immersion. In *IEEE Engineering in Medicine and Biology Conference*, pages 4271–4274, 2011.

[29] O.T. Inan et al. Multi-signal electromechanical cardiovascular monitoring on a modified home bathroom scale. In *IEEE Engineering in Medicine and Biology Conference*, pages 2472–2475, 2011.

[30] G. Bonmassar et al. Motion and ballistocardiogram artifact removal for interleaved recording of eeg and eps during mri. *NeuroImage*, 16(4):1127–1141, 2002.

[31] G. Srivastava et al. Ica-based procedures for removing ballistocardiogram artifacts from eeg data acquired in the mri scanner. *NeuroImage*, 24(1):50–60, 2005.

[32] X. Wan et al. Artifact reduction for eeg/fmri recording: Nonlinear reduction of ballistocardiogram artifacts. *Clinical Neurophysiology*, 117(3):668–680, 2006.

[33] J. Alametsa et al. The potential of emfi sensors in heart activity monitoring. *2nd Open ECG Workshop Integration of the ECG into the HER & Interoperability of ECG Device Systems*, 2004.

[34] M.B. Rappaport, H.B. Sprague, and W.B. Thompson. Ballistocardiography: I. physical considerations. *Circulation*, 7:229–246, 1953.

[35] M. Di Rienzo et al. 24h seismocardiogram monitoring in ambulant subjects. In *IEEE Engineering in Medicine and Biology Conference*, pages 5050–5053, 2012.

[36] A.D. Waller. A demonstration on man of electromotive changes accompanying the heart's beat. *J. Physiol.*, 8:229–234, 1887.

[37] W.B. Fye. A history of the origin, evolution, and impact of electrocardiography. *Am. J. Cardiology*, 73(13):937–949, 1994.

[38] Texas Heart Institute. Anatomy of the heart. `http://www.texasheartinstitute.org/HIC/Anatomy/anatomy2.cfm`.

[39] 6.522. Quantitative physiology. Lecture Notes.

[40] FlightPhysical. Holter monitor: Issues for aviators. `http://flightphysical.com/Exam-Guide/CV/Holter-Monitor.htm`.

[41] Medical Expo. Wireless digital electrocardiograph. `http://www.medicalexpo.com/prod/mindray/wireless-digital-electrocardiographs-computer-based-70856-439812.html`.

[42] Technical Insights. Multiparameter wireless monitoring device caters to all levels of acuity care settings. `http://www.frost.com/prod/servlet/cpo/197553557.htm`.

[43] MedGadget. Posts by ostrovsky. `http://medgadget.com/author/michael/page/137`.

[44] L. Afonso et al. Global and regional left ventricular contractile impairment in patients with wolff-parkinson-white syndrome. *Indian Pacing Electrophysiol. J.*, 9(4):195–206, 2009.

[45] M. Etemadi et al. Non-invasive assessment of cardiac contractility on a weighing scale. In *IEEE Engineering in Medicine and Biology Conference*, pages 6773–6776, 2009.

[46] O.T. Inan et al. Non-invasive measurement of valsalva-induced hemodynamic changes on a bathroom scale ballistocardiograph. In *IEEE Engineering in Medicine and Biology Conference*, pages 674–677, 2008.

[47] R.W. Stafford, W.S. Harris, and A.M. Weissler. Left ventricular systolic time intervals as indices of postural circulatory stress in man. *Circulation*, 41:485–492, 1970.

[48] H.H. Woltjer, H.J. Bogaard, and P.M.J.M. de Vries. The technique of impedance cardiography. *European Heart Journal*, 18:1396–1403, 1997.

[49] S. Hirschfeld et al. Measurement of right and left ventricular systolic time intervals by echocardiography. *Circulation*, 51:304–309, 1975.

[50] Boston Globe. What is a pulse oximeter, and what does it measure? `http://www.boston.com/news/globe/health_science/articles/2007/11/05/what_is_a_pulse_oximeter_and_what_does_it_measure/`.

[51] J. Muehlsteff, X.L. Aubert, and M. Schuett. Cuffless estimation of systolic blood pressure for short effort bicycle tests: The prominent role of the pre-ejection period. In *IEEE Engineering in Medicine and Biology Conference*, pages 5088–5092, 2006.

[52] M. Wong and Y.T. Zhang. The effects of pre-ejection period on the blood pressure estimation using pulse transit time. In *Medical Devices and Biosensors, 5th International Summer School and Symposium on*, pages 254–255, 2008.

[53] C.C.Y. Poon and Y.T. Zhang. Cuff-less and noninvasive measurements of arterial blood pressure by pulse transit time. In *IEEE Engineering in Medicine and Biology Conference*, pages 5877–5880, 2005.

[54] D.B. McCombie, A.T. Reisner, and H.H. Asada. Motion based adaptive calibration of pulse transit time measurements to arterial blood pressure for an autonomous, wearable blood pressure monitor. In *IEEE Engineering in Medicine and Biology Conference*, pages 989–992, 2008.

[55] A.I. Moens. *The Die Pulskurve (The Pulse Curve).* E.J. Brill, 1878.

[56] D.J. Korteweg. Uber die fortpflanzungsgeschwindigkeit des schalles in elastischen rohren. *Annalen der Physik*, 241(12):525–542, 1878.

[57] D.J. Hughes et al. Measurements of young's modulus of elasticity of the canine aorta with ultrasound. *Ultrasonic Imaging*, 1(4):356–367, 1979.

[58] Y. Chen et al. Continuous and noninvasive blood pressure measurement: a novel modeling methodology of the relationship between blood pressure and pulse wave velocity. *Ann Biomed Eng.*, 37(11):2222–2233, 2009.

[59] G. Zhang et al. Pulse arrival time is not an adequate surrogate for pulse transit time as a marker of blood pressure. *J. Appl. Physiol.*, 111(6):1681–1686, 2011.

[60] R.A. Payne et al. Pulse transit time measured from the ecg: an unreliable marker of beat-to-beat blood pressure. *J. Appl. Physiol.*, 100(1):136–141, 2006.

[61] Y. Chen. A new methodology of continuous and noninvasive blood pressure measurement by pulse wave velocity. In *Control Automation Robotics Vision, 11th International Conference on*, pages 1018–1023, 2010.

[62] J.M. Padilla et al. Assessment of relationships between blood pressure, pulse wave velocity and digital volume pulse. In *Computers in Cardiology*, pages 893–896, 2006.

[63] L.W. Bogert and J.J. van Lieshout. Non-invasive pulsatile arterial pressure and stroke volume changes from the human finger. In *Exp. Physiol.*, pages 437–446, 2005.

[64] V.V. Ermishkin et al. Beat-by-beat changes in pre-ejection period during functional tests evaluated by impedance aortography: a step to a left ventricular contractility monitoring. In *13th International Conference on Electrical Bioimpedance and the 8th Conference on Electrical Impedance Tomography*, pages 655–658, 2007.

[65] R.F. Yazicioglu et al. A 30μw analog signal processor asic for biomedical signal monitoring. In *IEEE International Solid-State Circuits Conference Digest of Technical Papers*, pages 124–125, 2010.

[66] H. Kim et al. A configurable and low-power mixed signal soc for portable ecg monitoring applications. In *VLSI Circuits, Symposium on*, pages 142–143, 2011.

[67] S.C. Jocke et al. A 2.6μw sub-threshold mixed-signal ecg soc. In *VLSI Circuits, Symposium on*, pages 60–61, 2009.

[68] F. Censi et al. On the resolution of ecg acquisition systems for the reliable analysis of the p-wave. *Physiological Measurement*, 33:11, 2012.

[69] J.W. Mason, E.W. Hancock, and L.S. Gettes. Recommendations for the standardization and interpretation of the electrocardiogram. part i: The electrocardiogram and its technology. *Circulation*, 115:1306–1324, 2007.

[70] R.R. Harrison and C. Charles. A low-power low-noise cmos amplifier for neural recording applications. *Solid-State Circuits, IEEE Journal of*, 38(6):958–965, 2003.

[71] N. Verma et al. A micro-power eeg acquisition soc with integrated feature extraction processor for a chronic seizure detection system. *Solid-State Circuits, IEEE Journal of*, 45(4):804–816, 2010.

[72] D. Johns and K. Martin. *Analog Integrated Circuit Design.* Wiley, New York, NY, USA, 1996.

[73] D.C. Daly and A.P. Chandrakasan. A 6-bit, 0.2 v to 0.9 v highly digital flash adc with comparator redundancy. *Solid-State Circuits, IEEE Journal of*, 44(11):3030–3038, 2009.

[74] M. Miyahara et al. A low-noise self-calibrating dynamic comparator for high-speed adcs. In *IEEE Asian Solid-State Circuits Conference*, pages 269–272, 2008.

[75] S. Mandal, S. Arfin, and R. Sarpeshkar. Fast startup cmos current references. In *Circuits and Systems, IEEE International Symposium on*, page 4, 2006.

[76] M.S.J. Steyaert and W.M.C. Sansen. A micropower low-noise monolithic instrumentation amplifier for medical purposes. *Solid-State Circuits, IEEE Journal of*, 22(6):1163–1168, 1987.

[77] R.F. Yazicioglu et al. A $60\mu w$ $60nv/rthz$ readout front-end for portable biopotential acquisition systems. In *IEEE International Solid-State Circuits Conference Digest of Technical Papers*, pages 109–118, 2006.